This document is downloaded from DR-NTU (https://dr.ntu.edu.sg)
Nanyang Technological University, Singapore.

Compatibility of wrist exoskeletons with human biomechanical and neural constraints

Mohammad Esmaeili Malekabadi

2014

Mohammad Esmaeili Malekabadi. (2014). Compatibility of wrist exoskeletons with human biomechanical and neural constraints. Doctoral thesis, Nanyang Technological University, Singapore.

https://hdl.handle.net/10356/62010

https://doi.org/10.32657/10356/62010

Downloaded on 13 Mar 2024 14:52:38 SGT

COMPATIBILITY OF WRIST EXOSKELETONS WITH HUMAN BIOMECHANICAL AND NEURAL CONSTRAINTS

MOHAMMAD ESMAEILI MALEKABADI

School of Mechanical and Aerospace Engineering

A thesis submitted to the Nanyang Technological University in partial fulfillment of the requirement for the degree of Doctor of Philosophy

2014

Abstract

Daily motor tasks are often kinematically redundant as they involve more degrees-of-freedom (DoF), for example in the human limbs, than strictly required. Humans are known to adopt motor strategies which consist of a stereotypical selection of specific postures for a given task. Such natural strategies are also known to be perturbed when, for example, operating in contact with machines or robots. To this end, a wrist exoskeleton, specifically designed to minimally perturb motor strategies, was used to study the effects of ergonomic factors and mechanical impedance on human motor strategies during redundant tasks. The novelty of this work is in accounting for the neural constraints imposed by the brain during redundant tasks. Special attention is devoted to wrist robots since the human wrist, together with the hand, is involved in most manipulation tasks, from cooking to micro-surgery, from dart-throwing to calligraphy. To comply with kinematic constraints, ergonomic considerations are introduced at an early stage of structural design of passive exoskeleton, matching the biomechanical constraints imposed by human anatomy. Due to inter-subject anatomical differences, subject-specific kinematic models are determined through a non-invasive protocol. The kinematic models are used to design subject-specific exoskeletons. The effects of kinematic compatibility on motor strategies are assessed through numerical and experimental studies and solutions from literature are adapted to avoid over-constrained configurations. Finally, confirming that perceived inertia is responsible for the perturbation of natural motor strategies during redundant tasks, a low-inertia wrist exoskeleton with one active DoF is devised and tested to be compatible with both biomechanical and neural constraints during pointing tasks.

Acknowledgements

First and foremost, I would like to thank my family for their love, support, inspiration and advice. I cordially confess that I am richly blessed to have my parents who are always there for me. I would like to thank my father for giving me strength and my mother for her unwavering love in my life. I also would like to thank my brothers and sister for their supports and providing me a peaceful mind by taking care of our parents in my away time. Utmost thanks go to the most special person in my life who was my friend first, my best friend then, became my girl friend after and eventually is my wife, now. Since the first day, she showed me the real life via her true love. She started learning about robotics and helping me by listening to my ideas and works enthusiastically and putting some inputs into them. When I was tired of work, she was the only one could cheer me up. Taiebeh, truly speaking, there is no word I can find to thank you.

Next, I would like to express my profound appreciation and sincere thanks to my supervisor, Dr. Domenico Campolo. He was beside me in every step of this project. He is a real knowledgeable person. Like a father for his child, he taught me how to properly conduct scientific research and be a good researcher. Domenico, I am very grateful to your sharp, constructive and goal-oriented guidance on this project especially when I might have been deviated from the main objective.

Thank you for being patient with me in every step. I also would like to thank Dr. Etienne Burdet for his supports and nice feedbacks on my work, especially for the period of my stay in Imperial College London.

My sincere thanks also go to Dr. Nathanaël Jarrassé for his truly friendly advices, encouragement and scientific knowledge sharing. I would also like to thank him for all his supports during my stay in Paris.

I must give my special thanks to my dearest friends Muhammad Azhar, Kumudu Gamage, and Ferdinan Widjaja from Robotic Research Center (RRC) in NTU and also Wayne Dialey, Atsushi Takagi and Asif Hussain from Bioengineering department in Imperial College London and Camille Dianoux from the Institute of Intelligent Systems and Robotics, University Pierre et Marie Curie, Paris who truly helped me during the fabrication, experiments and also scientific discussions. In no particular order, thank you to Mr. Lim Eng Cheng, Ms. Agnes Tan, from RRC and also Mr. Liew Quek Choi (Patrick) from School of Art, Design & Media, NTU who helped me with their technical knowledge and skill to fabricate my experiment setups.

Finally, I would like to thank NTU for the opportunity they gave me to conduct this PhD work.

Contents

Contents **v**

List of Figures **xi**

List of Tables **xxi**

1 Introduction **1**

- 1.1 Motivation 1
- 1.2 Objective 2
- 1.3 Scope and technical challenges 3
- 1.4 Organization of the report 4

2 The Scientific and Technological Background of Upper Limb Exoskeletons **7**

- 2.1 Upper limb exoskeletons 10
  - 2.1.1 Exoskeletons for telemanipulation 10
  - 2.1.2 Exoskeletons for augmenting human power 11
  - 2.1.3 Exoskeletons for virtual environments 11
  - 2.1.4 Exoskeletons for rehabilitation 12

2.2 Physical and cognitive human–robot interaction 13
2.2.1 Kinematic redundancy and motor strategies 16
2.2.2 Soft constraints of neural origin 19

3 Quantifying Neural Constraints: Donders' Law for the Wrist 23
3.1 Wrist kinematics 24
3.1.1 Notations for wrist orientation 24
3.1.2 Joint space (3D) 27
3.1.3 Endpoint space (3D) 28
3.1.4 Forward and inverse kinematics of the wrist 28
3.1.5 Task space (2D) 29
3.2 Center-out experiment 29
3.3 Data analysis 30
3.4 Results 32
3.4.1 Thickness distribution 32
3.4.2 Curvature and shape analysis 34
3.4.3 Prono-supination offset 34
3.5 Conclusion 36

4 Wrist Kinematic Modeling and Assessment: Application to Ergonomic Design of Exoskeletons 39
4.1 Anatomy of the wrist 40
4.2 Subject-specific wrist model calibration 42
4.2.1 Wrist kinematic model 45
4.2.2 Parameter Estimation 50
4.2.3 Numerical assessment of accuracy of kinematic model fitting 52

4.2.4 Experimental assessment of accuracy of fitted kinematic model . . . 56
4.2.5 Results . . . 58
4.3 Ergonomic exoskeleton design from subject-specific kinematic model 63
4.3.1 Protocol . . . 64
4.3.2 Data analysis . . . 64
4.3.3 Design of an ergonomic exoskeleton . . . 65
4.4 Conclusion . . . 67

5 Influence of Kinematic Compatibility on Human-Robot Interaction 69
5.1 Influence of kinematic compatibility in a human-machine interaction on reaction forces: Numerical study . . . 71
5.1.1 Modeling human-exoskeleton interaction in presence of kinematic mismatch . . . 74
5.1.2 Simulation and data analysis . . . 77
5.1.3 Results . . . 80
5.2 Influence of kinematic compatibility in Human-Robot Interaction on motor strategies: Experimental Study . . . 85
5.2.1 Experiments to evaluate kinematic compatibility . . . 86
5.2.2 Analysis of changes in motor synergies in presence of mechanical constraints . . . 89
5.3 Hyperstaticity and kinematic compatibility . . . 94
5.3.1 Experimental setup for hyperstaticity . . . 96
5.3.2 Hyperstaticity in the coupling . . . 97

5.3.3 Experiments to evaluate hyperstaticity 103
5.3.4 Results 106
5.4 Discussion 113
5.4.1 Numerical study 113
5.4.2 Experimental study 115
5.4.3 Hyperstaticity 115

6 Towards Haptic Devices Compatible with Neural Constraints 117

6.1 Transparency in Human-Robot Interaction 118
6.2 PS-actuated wrist robot 122
6.2.1 Actuator characterization 123
6.2.2 Gravity term characterization 123
6.2.3 Inertia and friction characterization 125
6.2.4 Gravity and friction compensation 127
6.3 Influence of the wrist robot on soft constraints 129
6.3.1 Experimental setup 129
6.3.2 Protocol 129
6.3.3 Data analysis 131
6.3.4 Results 131
6.4 Improving the design to reduce the perceived impedance 135
6.4.1 Method 135
6.4.2 Results 136
6.5 Discussion 141

7 Conclusion and Future Work 145

7.1 Conclusion 145

7.2 Future work 148

References **151**

List of Figures

2.1 Exoskeletons: a) MIT-Manus [104], b) IIT-Wrist [58], c) RiceWrist [32], d) CRAMER [90], e) Armeo [21] and f)EXARM [81]. 14

2.2 In a simple pointing, as a redundant task, two possible pointing could be performed by rotating about axes $\mathbf{r}_1$ and $\mathbf{r}_2$, respectively, with rotation angles θ and π. 17

3.1 Commutative diagram of the mappings between spaces. The three-dimensional joint and endpoint spaces fully describe the wrist configuration, and project via $\Pi(R)$ to the (two-dimensional) task space with screen coordinates $[l_x \; l_z]^T$. The orientations in the endpoint space can be represented either in terms of rotation matrices (R, which can be more practically related to the pointing task) or rotation vectors ($\boldsymbol{r}$, which provides an intuitive and more compact representation). 26

3.2 One trial performed by a representative subject with screen coordinates trajectories (a) and as in the rotation vectors space (b). . 30

3.3 Variance accounted for (VAF) vs. thickness for each trial for all subjects. Specific markers are used for the different subjects. . . . 33

3.4 Donders' surfaces of all trials for each subject. 33

3.5 a) Mean curvature (H) vs. Gaussian curvature (K) for all trials and all subjects. The different subjects are indicated with specific markers as indicated in the legend. Dotted lines indicate *loci* of (H, K) pairs with same Shape Index. b) Distribution of shape index eq. (3.13) for all subjects. 35

3.6 Distribution of joint angles. a) presents the distribution of the three joint angles (columns) for all subjects (rows) across all trials, where each line corresponds to one trial. b) shows the distribution of the PS joint of each subject when all trials are grouped together. 37

4.1 Bone structure of wrist. 41

4.2 Three possible wrist movements, from left to right Radial-Ulnar deviation (RUD), Flexion-Extension rotation (FE) and Pronation-Supination (PS). 42

4.3 Axes of rotation in the wrist joint in human wrist (a) and mechanical mock-up counterparts (b). $\boldsymbol{P}_1$ and $\boldsymbol{P}_2$ are the position vectors of the sensor S_1 on the forearm and S_2 on the 3rd metacarpal in the stationary frame, *Base*; $\boldsymbol{A}_1$ and $\boldsymbol{\omega}_{FE}$ are the position vector and orientation of the FE axis relative to the S_1; $\boldsymbol{A}_2$ and $\boldsymbol{\omega}_{RUD}$ are the position vector and orientation of the RUD axis relative to the S_2 pointing to the minimal distance Δ between the two axes. Details on the design and kinematics of the devices are provided in Section 4.3.3. 46

4.4 ComfGrip, the handle designed to be held in a unique and comfortable manner. 47
4.5 Standard form of Denavit-Hartenberg notation. 53
4.6 Simulated wrist joint (a) and different rotation trajectories (b) for parameter estimation. 55
4.7 Three typical movement conditions, a)*Restricted-locked* FE movement, b)*Restricted-locked* RUD movement and c)*Restricted-circum*. 57
4.8 The effect of joint covariation (a) and the number of samples (b) on relative error in estimations of methods M1 (squares) and M2 (circles). The solid line, dashes and dots present 0.15°, 0.30° & 0.45° angular RMS noise. 59
4.9 The effect of different ranges of motion and joint covariation on parameter estimation. Relative error in estimations of methods M1 (squares) and M2 (circles) in the presence of 20% (a) and 30% (b) joint covariation. 59
4.10 Different imposed joint rotations for parameter estimation. 61
4.11 Mean and standard deviation of relative error, respectively as an index for accuracy and repeatability, in estimating Δ, as a representative parameter of the physical mock-up in 'Restricted' and 'Unrestricted' conditions, imposing locked-short, locked-wide, unlocked-wide, unlocked-fluctuation, circumduction-short and circumduction-wide rotations for M1 (red stars) and M2 (blue crosses). 62

4.12 Procedure to design and manufacture a subject specific, ergonomic wrist exoskeleton *ErgoExo* (e). A 3D scan of the subject's hand is imported into Solidworks (a). The position of wrist rotation axes A_1 and A_2 are transferred to the Solidworks environment and used to align the exoskeleton's rotation axes with the corresponding wrist axes (b, c). Finally, the required complementary linkages are designed (d). 66

5.1 Exoskeleton with hand model. a) Configuration of the exoskeleton alongside the wrist. b) SimMechanics model. 73

5.2 Normalized frequency distribution of wrist joint rotation axes offset, based on [53]. 74

5.3 Functional diagram of the wrist and exoskeleton. Through a chain of links and joints human wrist is connected to the exoskeleton. Joint offset is considered for the both wrist (δ) and exoskeleton (δ^{exo}). Misalignment (m) is applied on the exoskeleton joints throughout the simulations. 75

5.4 Prototype of the exoskeleton. Besides, the FE and RUD joints of the exoskeleton which are supposed to mirror the human counterparts, the extra passive joints are considered to align the exoskeleton with different size of end users. 77

5.5 Steady-state sampling represented in time domain. Blue dash-line is the active movement of wrist followed by exoskeleton (red solid line) passively. Circles are the samples chosen when system is in steady-state condition. 79

5.6 Range of motion of exoskeleton (solid line-crosses) is compared with wrist (dots-circles) for a representative $+12mm$ misalignment on ω_{FE}^{exo}. 81

5.7 Normalized reaction force on FE joint of wrist over the range of motion of FE and RUD (a), and normalized deformation energy at attachment points of end-effector (b) for $+12mm$ misalignment on ω_{FE}^{exo}. 82

5.8 Normalized discomfort over the different amount of misalignments (a), and density of total discomfort over the range of wrist axes offset (b). The mean of total potential energy for a set of misalignment is taken into consideration in calculating total discomfort. . 83

5.9 Experimental setup for trials with ErgoExo. a) schematic view of the chair and subjects posture with respect to the screen, b) ErgoExo grasped by the subject. 87

5.10 'Center-out' pointing task. Starting from central target, the peripheral targets was turning on (the color was changed to red) by the software on a random sequence. The subject was instructed to point at the active (red) target. 88

5.11 Synthetic surfaces for the pointing task when PS is locked. 91

5.12 Donders' surfaces of all trials for each experiment. 92

5.13 a) Mean curvature (H) vs. Gaussian curvature (K) for all trials and all experiments. The different experiments are indicated with specific markers as indicated in the legend. Dotted lines indicate *loci* of (H, K) pairs with same Shape Index. The large black star represents the theoretical 'locked PS' condition (H=0, K=$-\frac{1}{4}$). b) Distribution of shape index for all experiments. The vertical line is the theoretical 'locked PS' condition (S=0). 93
5.14 The initial wrist robot to study the reaction forces during prono-supination rotation. 96
5.15 The human forearm attached to the Wrist Robot. Visualization of the force/torque sensor frame at O_s, the three rotation axes of human wrist (PS: Prono/Supination, FE: Flexion/Extension, RUD: Radiar/Ulnar Deviation) intersecting at the wrist joint center O_w, and that of the robot. 98
5.16 Schematic of the PS device and human forearm coupling. 98
5.17 Generating torque around the PS axis through application of forces. 101
5.18 Different views of the Ergonomic exoskeleton (ErgoExo). 102
5.19 Human forearm attached to the Wrist Robot. Visualization of the force/torque sensor frame, the three rotation axes of human wrist, and the robot. Passive DoFs are represented by orange arrows. . . 103
5.20 Improved Wrist Robot to study the reaction forces during prono-supination rotation. 103
5.21 Aligning the prono-supination axis of the subject and the robot. . 105
5.22 The amount of (a) total, (b) controlled, and (c) uncontrolled force and torque over all subjects, all trials using the ErgoExo. 106

5.23 Controlled ($\tau_c = \parallel \tau_x \parallel$) and uncontrolled ($F_{uc} = \sqrt{F_x^2 + F_y^2 + F_z^2}$, $\tau_{uc} = \sqrt{\tau_y^2 + \tau_z^2}$) force/torque for all subjects throughout the PS workspace, using the ErgoExo. 108
5.24 The components of force/torque for all subjects throughout the PS workspace. τ_x is controlled and the rest are uncontrolled force/torque components. 109
5.25 Experimental setup to conduct the Centre-out experiment. 110
5.26 Donders' surfaces of all trials for all subjects. Each row represents the results for one of the subjects. The columns from left to right, respectively, illustrate: free movements, movements using wrist robot while all DoFs are released, and movements with locked extra DoFs. 112

6.1 Mean curvature (H) vs. Gaussian curvature (K) for all trials and all subjects for the experiments reported in [11] done by InMotion3. 120
6.2 The wrist robot used as the platform to study motor synergies. . . 122
6.3 Motor torque constant (k_m) characterization setup (a). Plotting the τ_{motor} vs. applied current (b) resulted in a k_m value of 12.25 mNm/A. The d_z, R_r and R_p in (c) are the distance from load cell to the center of rotation, radius of the ring and radius of the pulley used to calculate τ_{motor} from force transducer reading. 124
6.4 Linear regression between τ_g^{PS} and $\sin(\theta_{PS})$ static values for the estimation of the Prono-Supination gravity term. The fitting curve slope gives the gravitational term as $\tau_g^{PS} = g_{PS} \sin(\theta_{PS}) = 0.42 \sin(\theta_{PS})$. 125

6.5 Multivariable linear regression for PS inertia and friction characterization as reported in (6.1). Considering the values averaged on 10 trials, a viscous friction $b = 0.0121\, Nm.s/rad$ and an inertia $B = 0.0045\, kg.m^2$ were found. 126
6.6 Linear regression between τ_{st}^{PS} and θ_{PS} static values for the estimation of static friction term. The fitting curve gives the torque required to overcome static friction, τ_0^{PS}, as $5.109\, mNm$. 127
6.7 Control scheme. 128
6.8 Experimental setup to conduct the Centre-out experiment. 129
6.9 Donders' surfaces of all trials for each subject (rows) for *free*, *uncompensated*, *gravity compensated* and *gravity-friction compensated* movements (columns). 132
6.10 a-d) Mean curvature (H) vs. Gaussian curvature (K) for all trials and all subjects for *free*, *uncompensated*, *gravity compensated* and *gravity-friction compensated* movements. Dotted lines indicate *loci* of (H, K) pairs with same Shape Index. e-h) Distribution of shape index eq. (3.13) for all subjects. 134
6.11 The modifications applied to our robot (a) resulted in the robot (b), the inertia could be reduced to less than one third of the original amount (from $3.4 \times 10^{-3}\, kg.m^2$ to $1.0 \times 10^{-3}\, kg.m^2$) and the mass by half (from $0.39\, kg$ to $0.20\, kg$). 136
6.12 Variance accounted for (VAF) for each trial for all movements and subjects. 137
6.13 Donders' surfaces of all trials for each subject in different movement conditions. 138

6.14 a-c) Mean curvature (H) vs. Gaussian curvature (K) for all trials and all subjects. Dotted lines indicate *loci* of (H, K) pairs with same Shape Index. d-f) Distribution of shape index eq. (3.13) for all subjects. 139

6.15 Distribution of shape index for each subject in different conditions. 140

7.1 Locating the load cell (`Mini40-E` Transducer from ATI Industrial Automation, Inc.) into the handle. 148

7.2 Differential mechanism to drive flexion-extension and prono-supination. 149

List of Tables

3.1 Range of motion for the wrist joint angles. 27

4.1 Parameters for the screw motion calculation. 49

4.2 Denavit-Hartenberg parameters for wrist model. 54

4.3 Mean and standard deviation of relative error in estimating Δ, as a representative parameter of the physical mock-up. 63

4.4 Estimated parameters for human wrist 65

5.1 Mean and standard deviation of controlled and uncontrolled force and torque for ErgoExo and simplified handle. $\boldsymbol{F}_{uc}$, $\boldsymbol{\tau}_{uc}$ are uncontrolled force and torque, and $\boldsymbol{\tau}_c$ is controlled torque. 109

6.1 The *mean curvature* (H), *Gauss curvature* (K) and *Koenderink's index* (S) for the C coefficients reported in [11] for InMotion3. . . 120

6.2 Components used to fabricate the wrist robot and implement the control. 122

6.3 Comparison between wrist robots studied in this research. 143

Chapter 1

Introduction

1.1 Motivation

In the last two decades, robots moved out of the factory, finding applications in human-related environments, from rehabilitation to surgery, typically assisting during motor tasks.

Application of robots to human environment requires safety considerations in the first place and user-friendly interfaces as a desired feature. Furthermore, robots operating in physical contact with humans require attention for all aspects of Human-Machine Interaction (HMI) ranging from machine design [30; 79], to force control [32; 58] and to motion planning [1]. However, these fields have been often treated separately from each other and a unifying holistic approach is still lacking.

A rather unexplored aspect of HMI is relative to situations where kinematic redundancy (hereafter redundancy) is present, which is often the case in everyday human activities. Redundancy occurs when more degrees-of-freedom (DoF) than strictly necessary are available to perform a given task (for details see 2.2.1). To cope with redundancy, the human central nervous system (CNS) is known to adopt stereotypical solutions considering 'soft' constraints, i.e. with a neural origin, which optimize motor efficiency, in some task-dependent sense [54]. Therefore, machines interacting with humans should minimally alter these motor strategies, not to perturb optimality of the motor task [11]. This is especially important for *ergonomic* robots, which is the focus of this work. Recent research has shown how even state of the art robots designed for neurorehabilitation of the human wrist might perturb natural motor strategies in healthy humans during redundant tasks [11]. It was hypothesized that such perturbation was due to an excessive mechanical inertia on prono-supination joint (better detailed in 2.2.2). Successive studies [94] showed how active control of the perceived inertia might reduce perturbations which, nevertheless, could never be fully overcome due to inherent mechanical characteristics of the robot. A clear message from these studies is that a new generation of robots compliant with human motor strategies should take these aspects into account in the early stage of mechanical design.

1.2 Objective

The main objective of this work is to design wearable wrist exoskeletons, both passive and active, which are compliant with human motor strategies in redundant tasks such as pointing. Methods from literature will be adapted to experimentally assess motor strategies and to quantify their perturbation in terms of geometric factors.

The design of passive exoskeletons, shall primarily take into account ergonomic factors, for which subject-specific kinematic models of the user shall be experimentally determined.

As for the active exoskeletons, I shall specifically focus on reducing the perceived inertia on the prono-supination axis (i.e. the most proximal) as this is recognized to be responsible for disruption of natural motor strategies.

1.3 Scope and technical challenges

In this study, I shall focus on wearable robots and machines for the upper limb, in particular for the human wrist. I will mainly consider mechanisms traditionally used in robots, i.e. consisting of rigid bodies connected via revolute or prismatic joints, and further restrict the attention to anthropomorphic mechanisms, i.e. kinematic structures whose joints closely match the human joints. In this sense, I shall target anthropomorphic exoskeletons meant to operate in concert with the human upper limb/wrist.

I shall aim at lightweight (low-inertia) wearable robots capable of exchanging forces/torques with the human limb. The generation of forces/torques could be either active or passive (e.g. to examine the effect of a purely elastic, viscous or inertial fields on natural motor strategies). Active force/torques generation will require the presence of actuators. As I shall primarily deal with modest levels of forces/torques, I will consider standard actuation (and transmission) technologies currently used in haptics rendering. My attention will be mainly devoted to mechanical transmissions which allow motors not to be carried around (as detailed in 6.2), further reducing the inertial effects of the actuators.

As a widely accepted approximation, at least in applications such as wearable robotics, the human upper limb and wrist will also be modeled as rigid bodies interconnected via revolute joints. However, within this framework, I shall not oversimplify the kinematic model and pay attention to the subject-specific characteristics and the possibility to determine a custom kinematic model based on non-invasive, ambulatory measurements.

The target motor task is pointing with the human wrist. This is a simple, redundant motor task widely used in human motor neuroscience and devised to assess and quantify specific natural motor strategies of rotational joints such as the human wrist. Such a quantitative, objective assessment of motor strategies will be used to determine the amount of perturbation induced by a given mechanical structure, based on the induced change of motor strategies.

1.4 Organization of the report

As for the structure of this report, Chapter 2, presents a literature survey for wearable robots. Kinematic redundancy and motor strategies, are also discussed in this chapter.

Chapter 3, first presents the mathematical notation used to model the wrist. Moreover, in this chapter a quantitative, objective assessment of motor strategies, i.e. Donders' law, for the wrist from my paper is presented [14].

Chapter 4, presents my method, for determining the anatomical parameters of the wrist. The method then is used to fit measurements performed on a human subject. The resulting parameters are applied in the design of a subject-specific, ergonomic exoskeleton meant to comply with the natural coordination mechanisms in the redundant wrist.

Chapter 5, presents the influence of kinematic compatibility, i.e. the alignment between human and robot joints, on reaction forces and human motor strategies through three main sections. In the first section of this chapter, a numerical study highlights the interaction forces and discomfort due to misalignments between the human joints and an anthropomorphic exoskeleton. Then, using the wrist exoskeleton from chapter 4, the effect of misalignment on the natural coordination mechanisms in the redundant wrist is assessed. Finally, I discuss how kinematic incompatibility might be related to human-robot fixation, referred to hyperstaticity. Afterwards, I implement a practical solution, from literature, to avoid hyperstaticity and reduce the level of undesired force/torque in the wrist.

Chapter 6, presents my wrist robot and discusses the characterization procedure I undertook to identify the impedance (i.e. gravity, friction and inertia) for the robot. Then, the transparency of the wrist robot and the effects of the perceived mechanical impedance on natural motor coordination mechanisms during a redundant task is assessed.

Finally, conclusion and future work are presented in Chapter 7.

Chapter 2

The Scientific and Technological Background of Upper Limb Exoskeletons

Robots, from the Czech word ‘robota’ (slave labor), have been traditionally employed for tasks too tedious or dangerous for humans. However, within the last decade, robots have progressively moved out of the factory and started to work with humans, rather than just for humans. Among the robots in close contact with humans I shall consider *Wearable robots*. Wearable robots are people-oriented robots designed to be worn either to substitute a missing limb or to be functional by the side of a limb. These robots are designed based on the function and shape of the human limb and can be either anthropomorphic or non–anthropomorphic, depending on whether its kinematic structure is morphologically similar to the limb or not [28]. Wearable robots can be classified in various ways, Pons [67] proposed the following categories:

Exoskeletons (orthotic robots): installed on human limb like an outside skeleton mapping the anatomy of the limb, these robots are meant to improve the lost strength or functionality of the mapped limb or to assess movements and forces of the patients.

Prosthetic robots: meant to replace a missing limb reproducing its function (at least aesthetically). Beside the general requirements of prosthetic devices (e.g. appearance, size and weight, durability and etc.) the sensing and actuation in these kind of robots represent the major challenge to provide a natural interaction between robot and humans [110].

Extenders: active manipulators worn by humans to enhance their strength. There are two types of extenders: upper and lower extremity. The upper extremity extenders reflect human's upper limb forces that are much smaller than the forces needed to manipulate loads. These extenders are developed for any precise application which requires complex movement of heavy objects [42]. The lower extremity extenders are meant to augment endurance during locomotion beside the strength enhancement [43].

In this study I shall focus on the exoskeletons.

In general, exoskeletons directly transfer mechanical power and exchange information with humans through the physical interface such as electromyography (EMG), electroencephalogram (EEG), forces, and vibrations [75]. Several joints are incorporated in an exoskeleton to interact with human counterparts.

The first concept of 'exoskeleton' was developed by Robert Seymour in a late 1820s by introducing 'Locomotion - Walking by Steam' though it was nothing more than a futuristic illustration. Seventy years later, in 1890, Nicholas Yagn was the first person to develop and file a patent for a passive human–powered exoskeleton [108]. In the early 1960s, scientific work on exoskeletons began with the concept of 'suit of armer' introduced by US Department of Defense. 'Man Amplifiers' is another concept developed by Cornell Aeronautical Laboratories of Buffalo almost at the same time [62]. Typically there is a master component, and a slave component in tele-operated manipulators. In other tele-operated manipulators, they are physically and spatially separate. In man–amplifier, they were together. So, one of the problems encountered was the close proximity of the control harness (master) with the powered exoskeleton. This concept was further developed by Ralph Mosher in General Electric Co. from 1966 to 1971. Hardiman is a name derived, from "Human Augmentation Research and Development Investigation" and Man from MANipulator. The original concept of Hardiman was a single master–slave system, to be split in two, the upper arms, and the lower legs [63]. A complete Hardiman was built with both arms, but earlier tests of just the single, upper manipulator was reported. Later, even when the full machine was built, one side was made static, and the other side was capable moving. However, major kinematic problems forced to fasten the master leg to the slave at the girdle. This changed the operating mode from "operator walk" to "operator ride". Later on, in 1990 Kazerooni [41] developed "extenders" presenting authentic power and information transmission between human and robot. This work will focus on the upper limb and, in the next section, upper limb exoskeletons will be discussed in greater detail.

2.1 Upper limb exoskeletons

Exoskeletons can either be used for lower or upper limbs. In this study I consider the exoskeletons used for upper limb especially for wrist. Exoskeletons have been divided into four major fields of application: telemanipulation, human power enhancement, virtual environment, and rehabilitation [6; 8; 55; 79; 109]. However, assigning only one field of application to most of the exoskeleton robots is not always realistic. For example, Hardiman exoskeleton is used for both telemanipulation and improving human power.

2.1.1 Exoskeletons for telemanipulation

In telemanipulation, a slave robot is controlled by an operator via a master robot, typically anthropomorphic. These exoskeletons are often heavy duty wall-grounded devices. Control is bilateral and force reflection to the human from the robot is one of the major challenges in these exoskeletons. *Hardiman* is the first complete arm exoskeleton developed for telemanipulation. The concept of master–slave manipulator was further developed by Human Sensory Feedback Lab at Wright-Patterson Air Force Base by introducing *Freflex* in 1992, a seven DoF active anthropomorphic exoskeleton meant to control a six DoF robot [105]. The other exoskeletons with bilateral control were *TOPS* and its commercialized version *SARCOS Dextrous Arm* which were hydraulically actuated [29] and developed under contract of the U.S. navy for underwater application in the frame time from 1991 to 1999. The robots were heavy duty wall-grounded and no performance study is reported for them in literature.

2.1.2 Exoskeletons for augmenting human power

In this application of exoskeletons both of the master and slave devices are worn by human to enhance human power. Hardiman and Freflex were also used for human power enhancement. In 1996, Repperger et al. [71] applied a performance study as well as several analysis techniques on Freflex to describe human's strength characteristics. They investigated human–exoskeleton compatibility for the first time in their study though preliminary results were presented. These exoskeletons are supposed to be portable [96], however, due to their actuator demands, size and weight of their structural elements, and mechanical complexity [37] no mobilized, body–grounded, human power enhancing exoskeleton is reported in literature.

2.1.3 Exoskeletons for virtual environments

The introduction of virtual reality in 1990s opened a new field of application for the exoskeletons used for haptic interaction. Haptics refers to sensing and manipulation through touch in a haptic interface. A haptic interface is a force reflecting device which allows a user to touch, feel, manipulate, create and/or alter simulated objects in the virtual environment. One of the first exoskeletons for virtual application was *GLAD-IN-ART*, a five DoF exoskeleton developed by Bergamasco et al. [4]. In order to effectively transmit power to human limb it was equipped with a complex cable transmission system. Caldwell et al. [10] combined tactile feedback glove and arm force sensor with a seven DoF arm exoskeleton to interact with virtual environment. They claimed 90% coverage for human workspace though they didn't present any results or actuator. To the best of my knowledge, feedback sensation and human–exoskeleton interaction is not reported in none of their publications.

2.1.4 Exoskeletons for rehabilitation

These robots have been developed for rehabilitation therapy of patients suffering from neurological injuries. The MIT-MANUS wrist module (InMotion3) is the first developed and commercialized for rehabilitation of the hand/wrist. Successively, RiceWrist, CRAMER and IIT-Wrist (see Figure 2.1) were also specifically developed for wrist rehabilitation and can be considered as the *first generation* of rehabilitation robots. The design of most of the robots for neurorehabilitation hinges upon the widely accepted principle that the patient must have an active role in the execution of the motor task. This basic principle has a profound impact on the technological choices regarding the mechanical structure and the control system of the robot [69]. Indeed, the voluntary movements of the users should be minimally perturbed by the physical interaction with the robot, especially during assessment. During therapy, the robot should assist the patients only when they are not able to complete the task autonomously. Also, the level of assistance should be tuned according to the patients' residual abilities [46]. The kinematics of the robot in terms of both workspace geometry and range of motion of each link should, in the first place, match the constraints imposed by the biomechanics of the human body. Moreover, special attention is devoted to achieving a high degree of back-drivability, i.e., the ability of the robot being moved by the user with a low perceived mechanical impedance [48] in order not to hinder any voluntary motions involved in the specific task. However, recent studies revealed that even highly backdrivable rehabilitation robots can perturb human natural motion due to the mechanical impedance of the robot [92].

The main drawbacks of the first generation of rehabilitation robots is relative to their bulky structure which makes these robots heavy and their 'one-size-fits-all' design which poorly adapts to the anthropometric characteristics of different end-users. Introducing *ergonomics* into robot design, Schiele et al. [82] proposed guidelines to design exoskeleton which can be adapted to different individuals. Based on such considerations Schiele et al. [82] developed *EXARM*, which could be considered as the second generation of the exoskeletons and exploits non-anthropomorphic kinematic structures to enhance human compatibility.

While all the studies have so far considered 'hard' constraints derived from biomechanical considerations, the design of robots physically interacting with humans should also consider another class of "soft" constraints: those with a neural origin, as highlighted in [11]. The novel aspect of the candidate's PhD work is to design and develop a robot which takes into account such 'soft' constraints.

2.2 Physical and cognitive human–robot interaction

Physical and *Cognitive* human–robot interaction are important aspects in the design of robots operating in human environments [7; 77]. Physical Human–Robot Interaction (*pHRI*) provides same workspace for human and robot to exchange forces and operate in action [88]. In Cognitive Human–Robot Interaction (*cHRI*), human maintains the control of the robot based on the information of the task

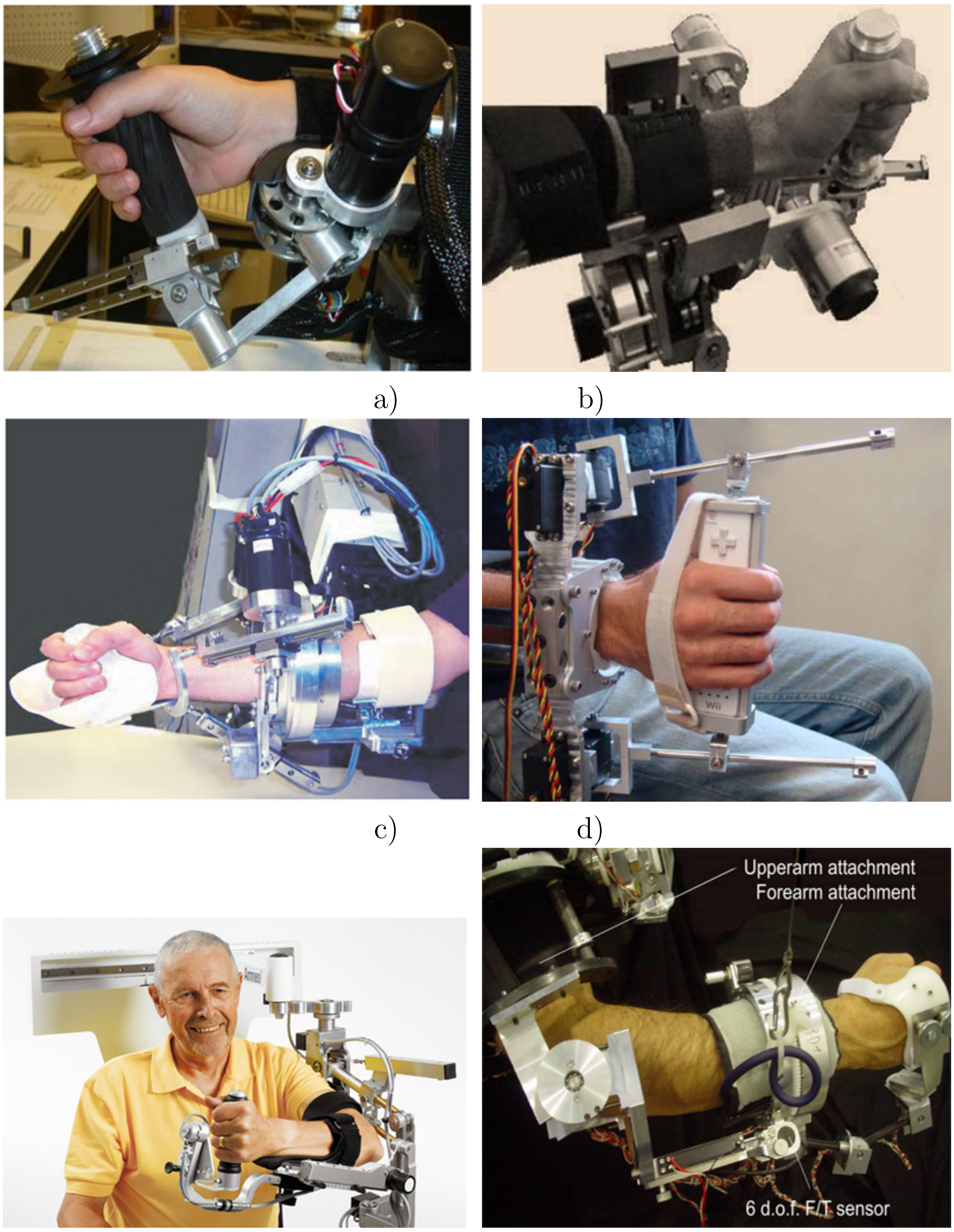
Wii
Armeo
Upperarm attachment
Forearm attachment
6 d.o.f. F/T sensor

a) b)

c) d)

e) f)

Figure 2.1: Exoskeletons: a) MIT-Manus [104], b) IIT-Wrist [58], c) RiceWrist [32], d) CRAMER [90], e) Armeo [21] and f)EXARM [81].

provided by robot [67]. More specifically speaking, *pHRI* mostly deals with force interaction between the human and robot while, *cHRI* makes use of other signals (i.e. visual, EMG and so forth) in human–robot interaction. In other words, information exchange in pHRI prevalently involves mechanical power.

pHRI and cHRI become even more crucial for wearable robots since these robots are meant to be worn by humans. While pHRI is mainly concerned with biomechanical aspects such as supplementary forces, cHRI is also concerned with the neural processes behind human motor control. Cognition refers to the high-level functions carried out by the human brain, including motor planning, action–perception coupling and motor control. However, cognition can also be extended to the robotic counterpart. So, for the wearable robots, cognitive processes appears both in the human and in the robot side and the flow of information between the two results in *cognitive interaction*. It should be emphasized that in developing cHRIs, researchers seek to take advantage of the natural control mechanisms fully optimized in humans.

Human–Robot interface includes both pHRI and cHRI. Physical human–robot interface, involves rigid structure and actuators for transmitting force to human limb. Cognitive human–robot interface, involves sensors to detect biomechanical/electrical variables in the human–robot direction; in the robot–human direction, utilizes bioelectrical variables, biomechanical variables, and natural perception modalities [61].

Physical and cognitive interactions are correlated. A physical interaction with the robot can bring about a cognitive process. For example, an operator can feel force in a telemanipulation through a wearable robot which renders haptic information on the remote object. Moreover, a cognitive interaction can be used to alter the physical interaction between human and robot. For example, in human–robot interaction tremor reduction, the compliancy of the exoskeleton is modified based on the biomechanical data of limb motion [51; 67].

2.2.1 Kinematic redundancy and motor strategies

Interrelation between physical and cognitive aspects during human–robot interaction becomes especially evident during motor tasks characterized by kinematic redundancy. Redundancy arises whenever the degrees of freedom of a manipulator (be it human or robotic) are more than the necessary ones to perform a task *kinematically redundant* [52; 84]. One experimental paradigm considered throughout this work is the pointing task, represented in Figure 2.2. The wrist joint is functionally redundant since it has three DoFs while the task has two DoFs. For example, to point at the target ‘B’, starting from configuration pointing at target ‘A’, one might rotate the wrist about a vertical axis $\mathbf{r}_1$ by an angle θ or, make a 180 degrees rotation about the horizontal axis $\mathbf{r}_2$. These are only two of the infinitely many possible strategies, for more details see [14].

Pointing with the human wrist, like gazing with the eye, is a kinematically redundant task, as infinite postures can be used to point in a given direction. How does the central nervous system (CNS) deal with this indeterminacy? Since the nineteenth century, studies on eye movements have shown the existence of simplifying strategies adopted by the brain when dealing with kinematically redundant problems. In particular, Donders (1847) showed that for any steady gazing direction, the human eye assumes the same combination of elevation, azimuth, and torsion angles. Donders’ law states that in the three-dimensional space of

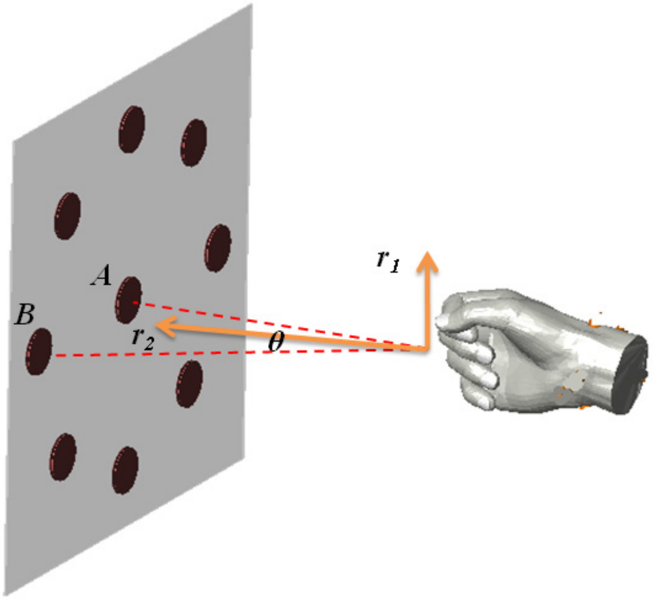

Figure 2.2: In a simple pointing, as a redundant task, two possible pointing could be performed by rotating about axes $\mathbf{r}_1$ and $\mathbf{r}_2$, respectively, with rotation angles θ and π.

possible eye configurations, the physiological eye configurations are constrained to a two–dimensional surface now called Donders' surface. When representing eye orientation by a rotation vector relative to the subject–dependent primary position (approximately corresponding to gazing straight ahead), Donders' surface appears as a plane normal to the primary position: The eye assumes only those postures that can be reached from the primary position by a single rotation about an axis in this Listings plane. In the last two decades, advanced technologies have allowed verifying this Listing's law during fixation as well as during saccade movements, smooth pursuit, and vergence [14].

The existence of a constrained behavior such as Donders' law in a mechanically unconstrained system indicates a *motor strategy.* For eye movements, where torsion is not under voluntary control, it was long debated whether Listing's law is due to a biomechanical or to a neural mechanism. It is now known that no such law holds during sleep, suggesting that Listing's law is actively implemented by a neural mechanism.

Like the eye, the wrist has three degrees-of-freedom, i.e., prono-supination, flexion-extension, and radial-ulnar deviation, which have approximately perpendicular but non-intersecting axes [53]. While the human wrist has obvious anatomical differences to the oculomotor system, a similar control mechanism may be used by the CNS for these two systems with similar kinematics.

Campolo et al. [13] investigated wrist movements using a dedicated apparatus. Experimental data of 3D wrist orientations during a pointing task with the wrist (and expressed in the standard coordinates based on rotation vectors as described in 3.1.1) were fitted with a quadratic surface. The fit was evaluated in terms of the surface thickness, defined as the standard deviation of its residuals. The data showed good fit with thickness between 1 and 2 degrees, exhibiting Donders' surfaces for the wrist with subject–specific curvature, possibly due to individual biomechanical factors.

Recently, I investigated wrist control by developing a simple phenomenological model to explain Donders' law for wrist postures [14]. This model considers both extrinsic (task-related) factors, as have been used to model the eye kinematics, and intrinsic (joint-related) factors, as have been used for the arm. The cost associated with extrinsic factors is assumed to be the same for all subjects while the cost associated to intrinsic factors, depending on the wrist kinematics and the range of each DoF, is parameterized to account for subject-specific biomechanical factors.

Although I used simple, U–shaped discomfort functions to account for intrinsic factors, my results show how subject–specific biomechanical factors might explain different behaviors in different subjects. In general, discomfort is due to interaction forces with a mechanism. Such forces might be due to kinematic, e.g., due to a mismatch between human and robotic joints, or dynamic, e.g., due to inertial, viscous or elastic properties of the wearable mechanism. In this thesis I report my studies on the ergonomics of exoskeletons. In particular, I consider discomfort due to reaction forces arising from kinematic misalignment between the human limb and a wearable mechanisms. In the next section I will detail more on the effects of inertial forces.

2.2.2 Soft constraints of neural origin

Ideally, robots closely interacting with humans, should minimally perturb the voluntary movements of a subject. To this end, the kinematics of the robot in terms of both the workspace geometry and the range of motions of each link should, in the first place, match the constraints imposed by the biomechanics of the human body. Such ergonomic considerations are discussed in Chapter 5. Aside from ergonomic considerations, special attention should be also devoted to achieving a sufficient degree of back-drivability, i.e., the ability of the robot being moved by the user with a low perceived mechanical impedance in order not to hinder any voluntary motions involved in the specific task which is addressed in Chapter 6. Campolo et al. [11] showed that besides “hard” (biomechanical) constraints, the design of robots physically interacting with humans should also consider another class of “soft” constraints: those with a neural origin, such as Donders’ law. In their studies, Campolo et al. [11], asked healthy subjects to perform pointing tasks, while the wrist orientation was assessed by means of a lightweight hand-held device to avoid perturbations of any sort. Data showed how such intrinsic constraints are well fitted to (2-D) surfaces embedded in the 3-D space of wrist orientations. Such surfaces do not vary much from trial to trial for the same subject but high variability is shown from subject to subject, especially in terms of curvature and twisting of the surface. In particular, this could denote different motor strategies for each subject, i.e., a personal “style” in solving redundancy. A different group of healthy subjects was then asked to complete a similar task while interacting with a state-of-the-art robot for wrist rehabilitation that is designed to fully comply with biomechanical constraints of the human wrist and provide a high degree of back-drivability. Whereas, in the case of a hand-held device, there were statistically significant differences between subjects, in the case of the wrist robot, there was no statistical difference both within subject and between subjects.

Campolo et al. [11] hypothesized that this effect on motor strategies was due to excessive inertia of the mechanism perceived at the prono-supination joint (the most proximal joint). The excessive inertia on the most proximal joint is due to a specific characteristic of the robot, see Figure 2.1 a) and b): actuators relative to the most distal part are mounted on the moving joints and therefore their inertia is carried around and heavily perceived at the proximal joints. Although such an inertia can be easily overcome by the (healthy) subject where necessary, during redundant tasks different kinematic solutions exist and subjects resort to deploying the most comfortable one, i.e. all subjects avoided the use of the prono-supination joint. This hypothesis was then confirmed in a successive study by Tagliamonte et al. [94] in which healthy subjects were requested to perform a similar pointing task in three different conditions: with lightweight handle, with a robot as in [11] and with the same robot while implementing a force control feedback. For the latter condition, the robot handle was equipped with a torque sensor and basic force control feedback was used to lower the perceived inertia of the prono-supination joint of the robot, see [93]. The experiments performed in the first two conditions confirmed previous results, i.e. a robot perceived too heavy would flatten any subject-specific feature in a redundant motor task, while when the robot inertia was actively decreased (up to four times) subject-specific properties and variability started to reappear in the motor output. The conclusions of this work are twofold, on the one hand the mechanical impedance of a robot (inertia, in the specific case of [94]) might not be compliant with 'soft' constraints of neural origin. On the other hand, the perceived inertia of a robot (or machine, in general) can be decreased via active control only up to a certain extent. This latter consideration calls for a different mechanical design which should avoid carrying around motors.

The main objective of this thesis was to devise wrist mechanisms which are compliant with both kinematic and dynamic constraints. As for kinematic constraints, ergonomic considerations will guide the structural design of the exoskeleton. As for the dynamic constraints, this research focused on procedures which minimize the perceived mechanical impedance at the endpoint. In all cases, the quantitative assessment of the neural constraints, and in particular their change, in redundant tasks such as pointing represented the efficacy of a proposed design.

Chapter 3

Quantifying Neural Constraints: Donders' Law for the Wrist

The central nervous system uses stereotypical combinations of the three wrist joint angles to point in a given (2D) direction in space. In this chapter, I first present the mathematical notation used to model the wrist then the *Center-out* experiment that would be used throughout this thesis to assess human motor coordination mechanisms during the redundant task is presented, then confirm and analyze this Donders' law for the wrist as well as the distributions of the joint angles. Afterwards, it is shown that the quadratic surfaces fitting the experimental wrist configurations during pointing tasks are characterized by a subject-specific Koenderink shape index, and by a bias due to the prono-supination angle distribution.

The concepts of this chapter as well as other findings of this study are published in the following paper. Not to deviate from the main stream of this thesis, the relevant parts of the published paper are reflected in this chapter.

- D. Campolo, F. Widjaja, M. Esmaeili, and E. Burdet, *Pointing with the wrist: a postural model for Donders' law*, Exp brain Res, 212(3):417-427, June 2011.

3.1 Wrist kinematics

Wrist motions are analyzed in three different spaces: joint, endpoint and task spaces which will be defined below.

3.1.1 Notations for wrist orientation

The 3D orientation of a rigid body such as the human wrist can be described by means of a 3×3 rotation matrix R (satisfying ortho-normality $R^T R = I$ and 'right-handedness' $\det R = +1$). A rotation is physically determined once the rotation axis $\boldsymbol{n}$ ($|\boldsymbol{n}| = 1$) and the rotation angle θ are known, thus can be described by a rotation vector $\boldsymbol{r} = \theta \boldsymbol{n}$.

The rotation matrix R corresponding to a rotation vector $\boldsymbol{r}$ can be computed via the Rodrigues' formula [64]:

$$R = \exp(\widehat{\boldsymbol{r}}) = I + \sin|\boldsymbol{r}| \frac{\widehat{\boldsymbol{r}}}{|\boldsymbol{r}|} + (1 - \cos|\boldsymbol{r}|) \frac{\widehat{\boldsymbol{r}}^2}{|\boldsymbol{r}|^2}, \tag{3.1}$$

where the skew-symmetric matrix $\widehat{\boldsymbol{r}}$ is defined through:

$$\widehat{\cdot} : \boldsymbol{r} = \begin{bmatrix} r_x \\ r_y \\ r_z \end{bmatrix} \longrightarrow \begin{bmatrix} 0 & -r_z & r_y \\ r_z & 0 & -r_x \\ -r_y & r_x & 0 \end{bmatrix} = \widehat{\boldsymbol{r}} .$$

Conversely, for a given rotation matrix R, the corresponding rotation vector can be computed as:

$$\boldsymbol{r} = \log_{\vee}(R) = \frac{\theta}{2\sin\theta} \begin{bmatrix} R_{3,2} - R_{2,3} \\ R_{1,3} - R_{3,1} \\ R_{2,1} - R_{1,2} \end{bmatrix} \tag{3.2}$$

where $\theta = \arccos((\operatorname{trace}(R) - 1)/2)$, valid for $\theta < \pi$.

Forward kinematics

Following the axes conventions of [107], the wrist orientation R can be computed as the ordered product of three rotations:

$$R(\boldsymbol{\theta}) = \exp(-\widehat{\boldsymbol{e}}_{\boldsymbol{x}}\, \theta^{PS}) \exp(\widehat{\boldsymbol{e}}_{\boldsymbol{z}}\, \theta^{FE}) \exp(\widehat{\boldsymbol{e}}_{\boldsymbol{y}}\, \theta^{RUD}) \tag{3.3}$$

and the corresponding rotation vector is:

$$FK(\boldsymbol{\theta}) := \log_{\vee}\left(R(\boldsymbol{\theta})\right) . \tag{3.4}$$

The transformations between these spaces are also detailed in Figure 3.1.

$$\begin{tikzcd}
(3D)\left\{\vphantom{\begin{matrix}R\\R\end{matrix}}\right. & & R \arrow[dl, "\Pi(R)"'] \arrow[r, bend left, "\log_{\vee}(R)"] & \boldsymbol{r} \arrow[l, bend left, "\exp(\widehat{\boldsymbol{r}})"] \arrow[r, bend left, "IK(\boldsymbol{r})"] & \boldsymbol{\theta} \arrow[l, bend left, "FK(\boldsymbol{\theta})"] \\
(2D)\left\{\vphantom{\begin{matrix}R\\R\end{matrix}}\right. & \begin{bmatrix} l_x \\ l_z \end{bmatrix} & & & \\
& \underbrace{\qquad}_{\textit{task space}} & \underbrace{\qquad\qquad\qquad}_{\textit{endpoint space}} & & \underbrace{\qquad}_{\textit{joint space}}
\end{tikzcd}$$

Figure 3.1: Commutative diagram of the mappings between spaces. The three-dimensional joint and endpoint spaces fully describe the wrist configuration, and project via $\Pi(R)$ to the (two-dimensional) task space with screen coordinates $[l_x\ l_z]^T$. The orientations in the endpoint space can be represented either in terms of rotation matrices (R, which can be more practically related to the pointing task) or rotation vectors ($\boldsymbol{r}$, which provides an intuitive and more compact representation).

Table 3.1: Range of motion for the wrist joint angles.

angle	min	max	unit
θ^{RUD}	-50	35	deg
θ^{FE}	-65	70	deg
θ^{PS}	-90	90	deg

Inverse kinematics

If the wrist orientation is given by the rotation matrix R, the joint angles $\boldsymbol{\theta} = [\theta^{RUD}\ \theta^{FE}\ \theta^{PS}]^T$ can be computed as the Euler angles [87]. Although, in general there are several solutions, the biomechanical range of motion of the wrist (see Table 3.1) yields a unique joint angles configuration for any reachable orientation:

$$IK(R) = \boldsymbol{\theta} = \begin{bmatrix} \operatorname{atan2}(R_{1,3}, R_{1,1}) \\ \arcsin(-R_{1,2}) \\ \operatorname{atan2}(-R_{3,2}, R_{2,2}) \end{bmatrix}. \tag{3.5}$$

3.1.2 Joint space (3D)

The human wrist can be modeled as a 3-DoF system comprising the following rotational joints[1] (from proximal to distal): prono-supination (PS), flexion-extension (FE), and radial-ulnar deviation (RUD). While FE and RUD are anatomically confined within the wrist, the latter being the most distal [2], the forearm PS is due to the articulated complex between elbow and wrist. I assume that these joints are characterized by the angles θ^{RUD}, θ^{FE} and θ^{PS} confined to a biomechanical range. These angles are grouped in a 3D vector $\boldsymbol{\theta} := [\theta^{RUD}\ \theta^{FE}\ \theta^{PS}]^T$ which are the coordinates of the *joint space*.

---

[1] Anatomically speaking, only flexion-extension and radial-ulnar deviation are part of the wrist, while pronation-supination is part of the forearm but functionally they all contribute to the final 3D orientation of the hand.

3.1.3 Endpoint space (3D)

The *endpoint space* is constituted by the spatial orientations of the wrist with respect to the anatomical *neutral configuration* [107]. Given an orthonormal fixed frame $\{\boldsymbol{e}_x; \boldsymbol{e}_y; \boldsymbol{e}_z\}$ (pointing respectively forward, left and up), a moving orthonormal frame $\{\boldsymbol{e}_1; \boldsymbol{e}_2; \boldsymbol{e}_3\}$, attached to the hand, is uniquely defined as to coincide with the fixed frame in the neutral configuration. At any time, the components of the moving frame in fixed frame coordinates are given by

$$\boldsymbol{e}_1 = R \begin{bmatrix} 1 \\ 0 \\ 0 \end{bmatrix}, \quad \boldsymbol{e}_2 = R \begin{bmatrix} 0 \\ 1 \\ 0 \end{bmatrix}, \quad \boldsymbol{e}_3 = R \begin{bmatrix} 0 \\ 0 \\ 1 \end{bmatrix} \tag{3.6}$$

where R is a 3×3 rotation matrix R (the identity matrix corresponds to the neutral configuration).

While the matrix representation is practical to combine different orientations, a geometrically more intuitive representation of orientation is provided using a *rotation vector*: a rotation can be represented by the vector $\boldsymbol{r}$ pointing in the direction of the rotation axis with magnitude $|\boldsymbol{r}|$ corresponding to the rotation angle. Vector and matrix representations are related as described in Section 3.1.1, by the Lie groups exponential (3.1) and logarithmic (3.2) maps.

3.1.4 Forward and inverse kinematics of the wrist

The joint and endpoint spaces are related through forward and inverse kinematic transformations. To any given set of values for the joint angles (within the joint limits) there corresponds a unique wrist configuration, yielding the *forward kine-*

matic transformation $\boldsymbol{r} = FK(\boldsymbol{\theta})$, defined in (3.4). Similarly, any physiological configuration of the wrist is realized by a unique combination of joint angles, yielding the *inverse kinematic transformation* $\boldsymbol{\theta} = IK(\boldsymbol{r})$ defined in (3.5)[1].

3.1.5 Task space (2D)

A hand-held laser aligned with $\boldsymbol{e}_1$, pointed in a direction $\boldsymbol{n} = R\boldsymbol{e}_x$ ($|\boldsymbol{n}| = 1$) towards a vertical screen in the yz-plane, would hit the screen at coordinates:

$$\begin{bmatrix} l_y \\ l_z \end{bmatrix} = \Pi(R) := \begin{bmatrix} 0 & -1 & 0 \\ 0 & 0 & 1 \end{bmatrix} R \begin{bmatrix} 1 \\ 0 \\ 0 \end{bmatrix}, \tag{3.7}$$

assuming the origin of the screen at unit distance from the wrist along $\boldsymbol{e}_x$ and the y-axis of the screen directed as $-\boldsymbol{e}_y$.

3.2 Center-out experiment

Experiments similar to [13] were conducted to provide data for testing the model. Eight healthy subjects with no known history of neuromuscular impairment, who declared to be right-handed and gave their informed consent, performed a pointing task from a central target towards one of eight targets 15° away from the center and oriented at $\{0^o, 45^o, 90^o, 135^o, 180^o, 225^o, 270^o, 315^o\}$([13], Figure 3.2a). Each *trial* consisted of eight back and forth movements to the targets in random sequence. Each subject performed ten consecutive trials.

---

[1] In general, wrist joint of mechanical systems involve singularities, however the restriction to physiological range of motion of the human wrist joints (Table 3.1) allows using singularity-free transformations.

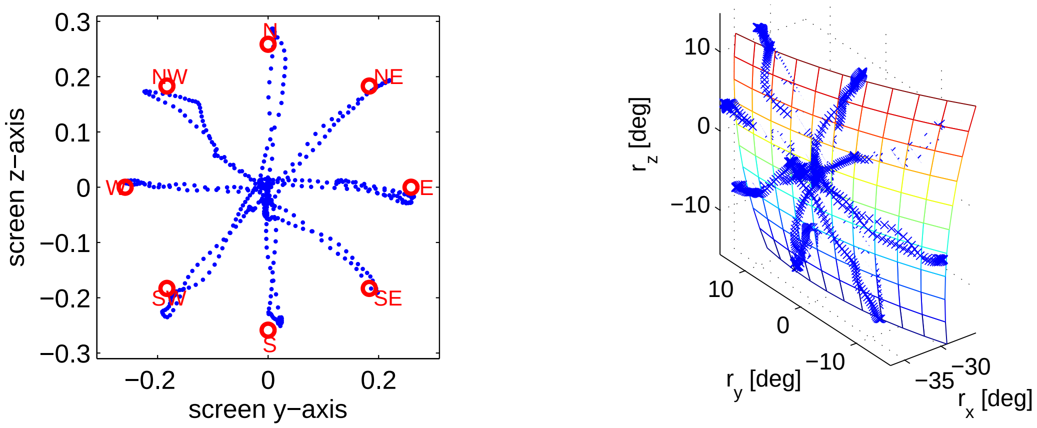

a) b)

Figure 3.2: One trial performed by a representative subject with screen coordinates trajectories (a) and as in the rotation vectors space (b).

Throughout the experiment, each subject was strapped to a chair to restrain all torso and upper-limb motions except the ones of interest (FE, RUD and PS for the wrist). To acquire data, each subject would grasp a lightweight handle, sensorized with an orientation tracking sensor (MTx-28A-33-G25 device from XSens Inc. with $< 1^o$ static orientation accuracy and $40Hz$ bandwidth. Before starting each trial a zeroing-procedure was carried out, defining the anatomically neutral position for the wrist as the initial one (by default, such a zero-position would point towards the central target), see [13] for details. Data at $120Hz$ were downloaded onto a local PC for offline data analysis. Real-time visual feedback of the current pointing position was provided during movement.

3.3 Data analysis

Data acquired from each trial consisted of a sequence R_i of 3×3 rotation matrices where i being sample number with 100 samples per second. For each trial, I computed the sequence of corresponding rotation vectors

$$\boldsymbol{r}_i = [r_{xi}\ r_{yi}\ r_{zi}]^T := \log_{\vee}(R_i) \tag{3.8}$$

Then I fitted the sequence of the first components r_{xi} to a quadratic function [13]:

$$r^*_{xi} = C_1 + C_2 r_{yi} + C_3 r_{zi} + C_4 r^2_{yi} + 2C_5 r_{yi} r_{zi} + C_6 r^2_{zi} \tag{3.9}$$

which defines the *Donders' surface*, as well as the *thickness* defined as the standard deviation of the residuals $r^*_{xi} - r_{xi}$. C_1, C_2, and C_3 are indicative of linear features such as tilt and offset of the surface in 3D space, while C_4, C_5, and C_6 are related to the surface's curvature. A more standard goodness of fit index is provided by the *variance accounted for*

$$\mathrm{VAF} := \left(1 - \frac{\mathrm{var}(r^*_i - r_i)}{\mathrm{var}(r_i)}\right) 100\%\,, \tag{3.10}$$

which was also computed relatively to the fitting of each trial for all subjects. Figure 3.2b shows an example of fitting of experimental data for a representative subject.

The *mean curvature*, i.e., the mean of largest and smallest section curvatures, expressed in the C_i coefficients as [20], [13]

$$H = \frac{(2 + 2C_3^2)C_4 - 4C_3C_2C_5 + (2 + 2C_2^2)C_6}{2\,(1 + C_2^2 + C_3^2)^{3/2}}\,, \tag{3.11}$$

and the *Gauss curvature*, corresponding to their product and expressed in the C_i

coefficients as [20], [13]

$$K = \frac{4C_4C_6 - 4C_5^2}{(1 + C_2^2 + C_3^2)^2}\,, \tag{3.12}$$

are used to analyze the *geometric invariant features* of Donders' surfaces near the origin. Koenderink's Shape Index [45]

$$S = -\frac{2}{\pi}\arctan\frac{H_0}{\sqrt{H_0^2 - K_0}} \tag{3.13}$$

is employed to analyze the 'shape' of Donders' surfaces. Koenderink's index captures the intuitive notion of shape independently of the curvature's amount, e.g. two spheres of different radii have same shape index but different amounts of curvature. By definition $-1 \leq S \leq 1$.

3.4 Results

3.4.1 Thickness distribution

Data from each single trial were fitted with the generic quadratic surface of eq. (3.9). As in [13], for most of the trials and in most of the subjects the thickness was around 1°: 0.9^o median and 1.0^o mean value. Figure 3.3 displays the relationship between the thickness and the variance accounted for (VAF) index relatively to the fitting of each trial for all subjects.

Figure 3.4 shows the Donders' surfaces relative to all trials, for each subject. From a visual inspection, two major features appear. The first is that inter-subject differences can be appreciated in terms of curvature of Donders' surfaces, confirming [13].

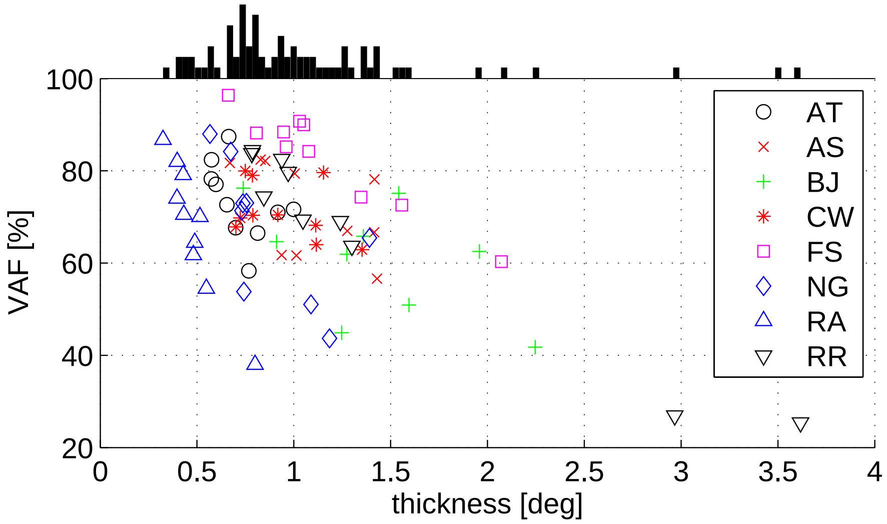

Figure 3.3: Variance accounted for (VAF) vs. thickness for each trial for all subjects. Specific markers are used for the different subjects.

The second feature is that besides shape, the surfaces seem to be characterized by an 'offset' in the r_x component, corresponding to an offset in prono-supination (note: when pointing at the central target, $r_y = r_z = 0$, then $r_x = -\theta^{PS}$).

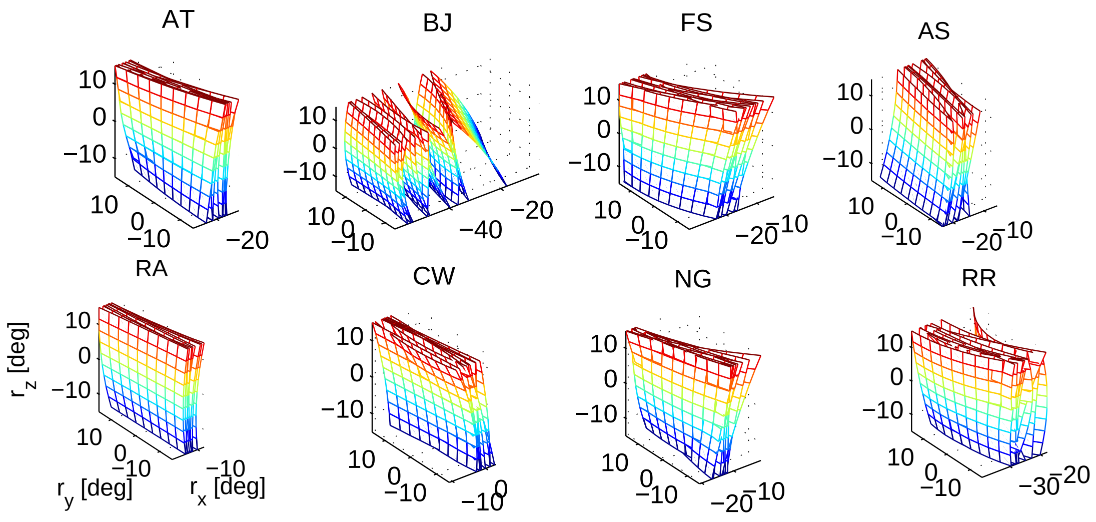

Figure 3.4: Donders' surfaces of all trials for each subject.

3.4.2 Curvature and shape analysis

Figure 3.5a shows Gauss curvature K as a function of mean curvature H, for all trials of all subjects. Note that, as H is the mean of the minimal and maximal one-dimensional curvature and K its product, (H, K) pairs can only assume values in the region $K \leq H^2$. This plot reveals between subjects differences in terms of curvature. The dotted lines in Figure 3.5a show the *loci* of equivalent Shape Index, suggesting subject specific clustering in terms of shape. Indeed, Figure 3.5b illustrates subject specific distributions of shape index. In most of the trials and subjects, the Donders' surfaces have a negative shape index ($p < 10^{-6}$, t-test).

To further investigate inter-subjective differences in terms of shape, a non-parametric analysis of variance (Kruskal-Wallis test) is performed for all trials, using the shape index as dependent variable and the subjects as grouping factor. This highlighted statistical differences ($p < 10^{-7}$) for the median of the groups. Based on Kruskal-Wallis statistics (using the Matlab7.1 `multcompare` function), pairwise comparisons were also performed which showed between-groups differences (at 95% confidence level). Except for subjects 'NG' and 'BJ', all other subjects have Shape Index distributions which are significantly different (95% confidence level) from some other subject.

3.4.3 Prono-supination offset

To analyze the PS joint offset, I used the inverse kinematics of the wrist model (3.5) to estimate joint angles from the experimental wrist orientations. Figure 3.6a shows the distribution (estimated for each joint angle via the `ksdensity`

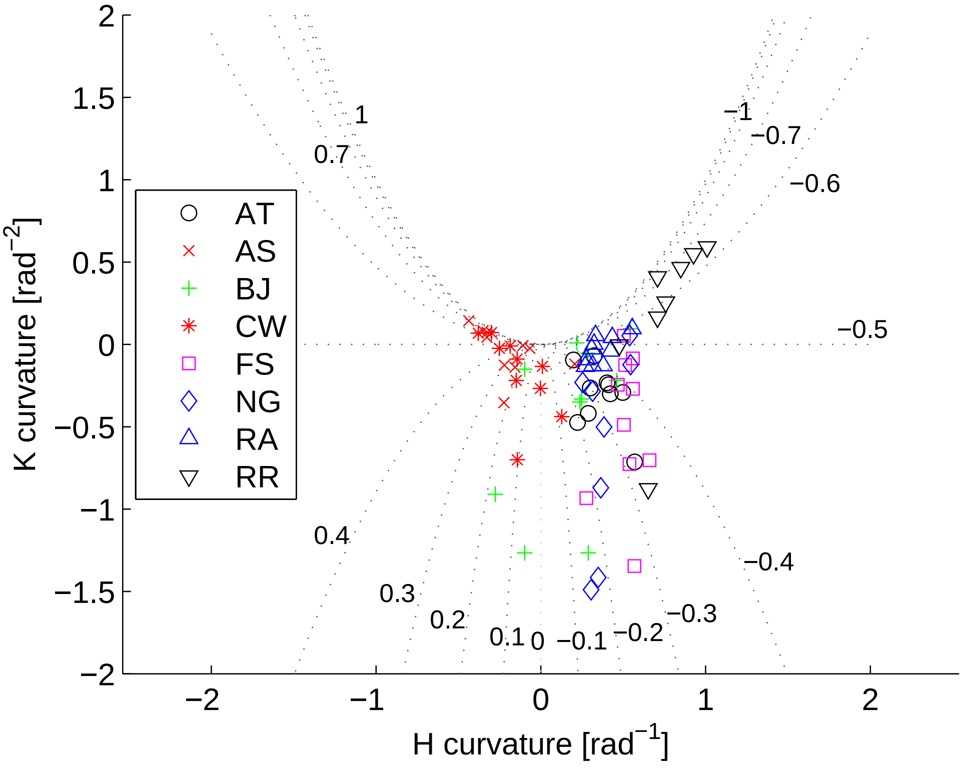

a)

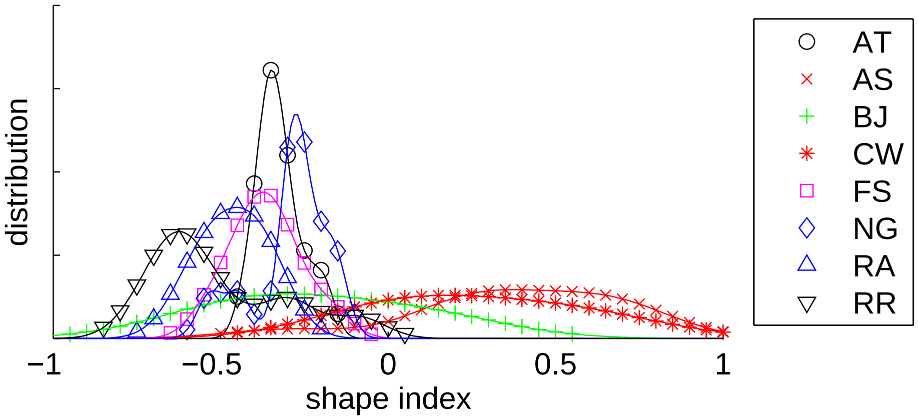

b)

Figure 3.5: a) Mean curvature (H) vs. Gaussian curvature (K) for all trials and all subjects. The different subjects are indicated with specific markers as indicated in the legend. Dotted lines indicate *loci* of (H, K) pairs with same Shape Index. b) Distribution of shape index eq. (3.13) for all subjects.

function in Matlab 7.1) of the three joint angles (columns) for each subject (rows), superimposing for each subject all the trials (each solid line represents the distribution for a single trial). It is clear that RUD and FE have a similar and roughly symmetric distribution both within- and between-subjects (no statistical difference was detected for either mean and standard deviation of the distributions for RUD and FE by a Kruskal-Wallis test, using subjects as grouping factor).

The task redundancy becomes evident when analyzing the PS joint (third column of Figure 3.6a). A large variability is observed in terms of both mean and standard deviation of the PS joint angle. In particular a Kruskal-Wallis test detected statistical differences for the PS joint distribution both in terms of mean ($p \leq 10^{-13}$) and standard deviation ($p \leq 10^{-9}$) when using subjects as grouping factor. To better appreciate these differences, Figure 3.6b shows the mean vs. standard deviation of the PS joint angle distribution for all subjects.

3.5 Conclusion

In this study, I first recorded human subjects performing wrist movements from a central position on a screen to eight peripheral targets. In line with previous work [13], the results first confirmed the existence of a reproducible relation between the forearm pronation/supination, wrist flexion/extension and wrist radial-ulnar deviation solely dependent on the pointing direction, i.e. a Donders' law. For each subject, the 3-dimensional rotation vectors describing the wrist configuration could be well fitted by a second order (Donders') surface. Furthermore, subject-specific features of the Donders surface such as distinct biases in the forearm prono-supination and distinct curvatures and shapes were found.

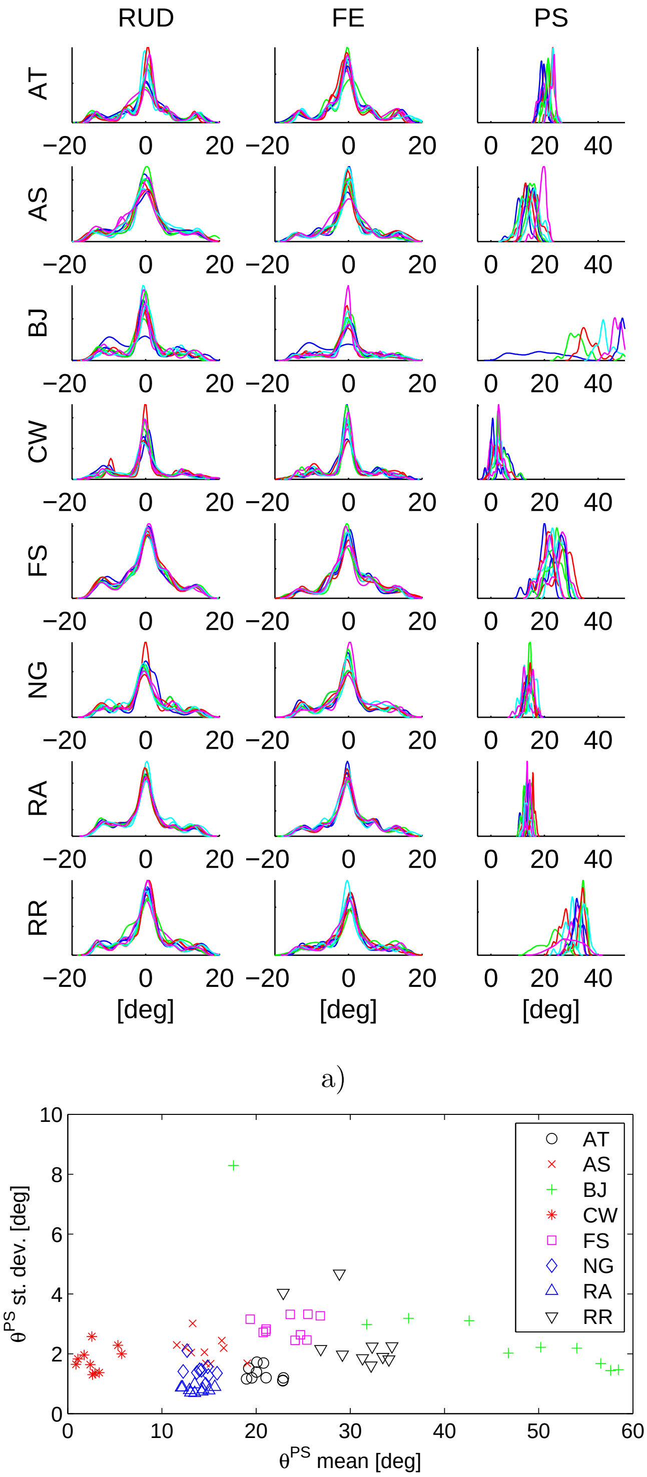

a)

b)

Figure 3.6: Distribution of joint angles. a) presents the distribution of the three joint angles (columns) for all subjects (rows) across all trials, where each line corresponds to one trial. b) shows the distribution of the PS joint of each subject when all trials are grouped together.

Chapter 4

Wrist Kinematic Modeling and Assessment: Application to Ergonomic Design of Exoskeletons

The goal of this chapter is to analyse the accuracy of non-invasive methods to determine subject-specific kinematics of wrist axes based on unrestricted measurements. Adapting methods from the literature, joint parameters are fitted from measurements derived through an in-vivo, non-invasive procedure. This chapter analyzes the accuracy of these fitting methods by using a mechanical mock-up, with known geometry and kinematic structure similar to the human wrist, which provides a ground truth for assessment of accuracy. The method was used to fit measurements performed on a human subject. The resulting parameters were applied in the design of a subject-specific, ergonomic exoskeleton meant to comply with the natural coordination mechanisms in the redundant wrist.

The findings of this chapter is published as

- M. Esmaeili, S. Moussouni, F. Widjaja, K. Gamage, and D. Campolo, *Accuracy and repeatability of parameter estimation methods from ambulatory data for the wrist joint*, 33rd Annual International Conference of the IEEE Engineering in Medicine and Biology Society (EMBC), International Conference on, Aug 30th Sept 3rd 2011.
- M. Esmaeili, S. Guy, W. D. Dailey, E. Burdet, and D. Campolo, *Subject-Specic Wrist Model Calibration and Application to Ergonomic Design of Exoskeletons*, IEEE Sensors journal, 13(9):3293-3301, September 2013.

4.1 Anatomy of the wrist

In this section the bone structure and degrees-of-freedom of the wrist are describe. The rotation of radius about the ulna bone, produces the pronation-supination (PS) motion (see Figure 4.2) which functionally contributes to the final 3D orientation of the hand and thus it is considered as one of the DoFs of wrist. The other two DoFs of wrist, i.e., flexion-extension (FE) rotation and radial-ulnar deviation (RUD), are provided through articulation at the radiocarpal joint[1], the midcarpal joint[2], the carpo-metacarpal joint[3], and between individual carpal bones [3]. Carpal bones are connected to radius bone of forearm proximally and to the five metacarpal bones of the hand distally [44] (Figure 4.1). Thus, when

---

[1] The joint between the radius and the proximal carpal row is called radiocarpal

[2] Midcarpal joint is between the proximal and distal rows of carpal bones

[3] Carpo-metacarpal is between the distal row of carpal bones and the metacarpal bones

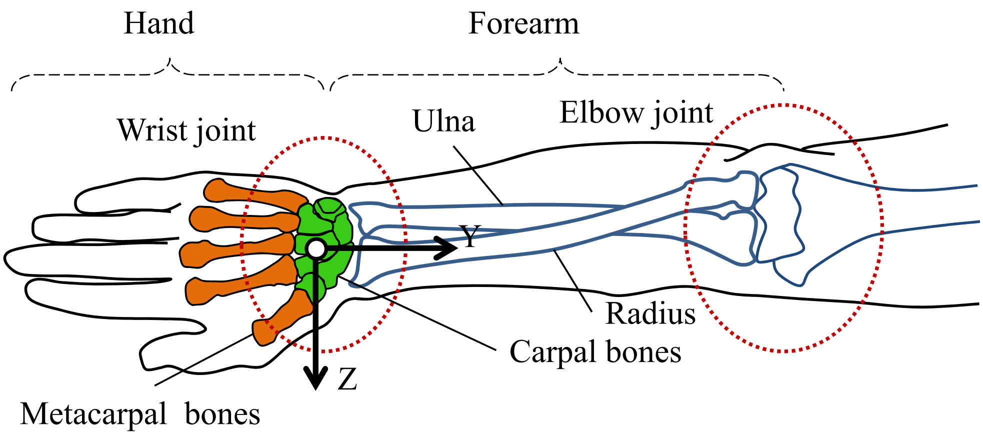

Figure 4.1: Bone structure of wrist.

the hand rotates toward the palm (volarly), flexion occurs and when the hand rotates in opposite direction (dorsally), extension occurs. Radial deviation occurs when the hand moves toward the thumb and ulnar deviation occurs when hand moves away from the thumb (Figure 4.2). There is a large inter-subject variation for the Range of Motion (RoM) of the wrist. But, as an average I consider the RoM as in Table 3.1.

A standard reference frame can be defined based on ISB[1] recommendation [107], considering forearm in the standard anatomical position[2] the positive $X-$axis is directed volarly, the direction of positive $Y-$axis proximal and the positive $Z-$axis is pointing to the right (Figure 4.1).

---

[1] International Society of Biomechanics

[2] For standard position of right forearm, palm is anterior and the thumb lateral.

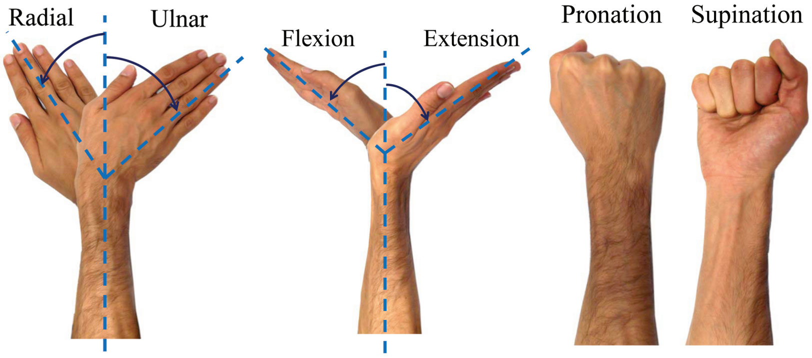

Figure 4.2: Three possible wrist movements, from left to right Radial-Ulnar deviation (RUD), Flexion-Extension rotation (FE) and Pronation-Supination (PS).

4.2 Subject-specific wrist model calibration

It is widely understood that in presence of redundant tasks, i.e., when more degrees of freedom of mobility are available than strictly necessary, neural constraints might be imposed by the brain to solve the redundancy. This has been shown to occur for specific tasks such as gazing with the eyes [97] or with the head [15] as well as during pointing tasks performed with the arm [54] or with the wrist [13]. For historical reasons, such constraints are also known as Donders' Law [22]. Being of neural origin, constraints are strongly influenced by the environment. Specifically, the amount of interaction forces exchanged with a robot [11; 95] has been shown to influence Donders' Law. Interaction forces between robots or mechanisms and humans can be of dynamic and/or kinematic origin. For the latter, ergonomic factors such as misalignments between human and exoskeleton joints result in the generation of reaction forces [24] which have the potential to affect natural motor strategies. To design ergonomic exoskeletons which minimizes the misalignment between the human and mechanical joints, it is important to derive an accurate human kinematic model.

Computer tomography (CT) and magnetic resonance imaging (MRI) are the most common technologies used for in-vivo wrist motion studies [17; 31; 106]. These technologies provide precise results but are bulky and expensive, and thus difficult to use in rehabilitation clinics or research laboratories. Recent developments in motion tracking technology [102] have made low cost kinematic assessment techniques suitable for clinic environments more widely available [18].

Based on both in-vivo and in-vitro studies, it is considered an acceptable simplification to model the human wrist as a universal joint with two axes: the flexion-extension axis (FE) which is proximal and fixed in the forearm, and the radial and ulnar deviation (RUD) axis which is distal and fixed in the hand. In healthy adults, these two axes are skew-oblique and approximately orthogonal, with a typical offset of a few millimeters [2; 53].

Several in-vivo, non-invasive calibration methods have been proposed for joints of the human upper limb[1] which are suitable for unrestricted movement measurement [5; 18; 66; 68; 72]. Many similarities exist among these approaches, e.g., they all assume a serial kinematic chain with unknown parameters to model the human upper limb (or a subset of its joints) and optimal estimates for the unknown parameters are derived from measurements.

In this chapter it is investigated how joint covariation and range of motion may influence the outcome of the calibration method introduced in [26]. The human wrist is actuated by at least five muscles, all of which contribute to both FE and RUD rotations. Therefore, voluntary wrist movement involving only one degree of freedom is unlikely. In other words, when a subject is asked to perform a pure flexion/extension of the wrist, the actual movement typically involves ulnar deviations to some extent. This is important when addressing complex joints such as the human wrist, as several calibration methods [5; 68] rely on single-joint movements and joint covariation which might induce errors in the estimation. On the other hand, methods devised to assess multiple joints at a time might perform poorly due to a lack of significant joint covariation.

---

[1] In these studies, the shoulder is regarded as ball-in-socket joint, while the remaining joints at elbow and wrist are regarded as rotational hinges.

In my initial study [26], I selected two representative methods from those available in the literature focusing on the two skew-oblique axes of the wrist: the first method, *M1*, proposed by Biryukova et al. [5], was devised to estimate parameters for one joint at a time; the second method, *M2*, adapted from Prokopenko et al. [68], was used to estimate all parameters simultaneously [26]. The second method was adapted because in the original work [68], the authors minimize the 'Direct Kinematic Error', which is a weighted sum of position errors and orientation errors (between estimated and measured data). This step requires a somewhat arbitrary choice of weights. Prokopenko et al. [68] justify this choice based on a specific set of data but it is clearly movement-dependent.

Non-invasive calibration methods proposed in the literature are typically tested over multiple trials. Due to a variety of sources of errors (e.g. noisy measurements and skin motion) different estimates are obtained from different trials. The standard deviation of the parameters across trials or the norm of residuals in the fitting process [68] are often taken as an index of accuracy. In fact, standard deviation or goodness-of-fit are indices of repeatability but not accuracy, as the ground-truth, i.e., the actual geometry of the problem, is not known (only invasive methods can be used to measure the real anatomical features).

In [26], the adapted method M2 was tested on a set of synthetic data in addition to real data acquired via a mechanical mock-up. In both cases, the ground-truth was known and I could therefore determine accuracy. In this study, a new mock-up (shown in Figure 4.3.b) with a more robust structure is developed and used to avoid several structural irregularities (e.g., screw effect in joint rotations). This enabled me to compare the accuracy and repeatability of the adapted method M2 using the two calibration methods [5; 26]. I also investigated the effect of different movement conditions/covariations on estimated parameters. For example, stroke patients have stiffer muscles and would have a limited range of motion relative to the natural range, or tremor might be observed during the movements of subjects with Parkinson disease.

4.2.1 Wrist kinematic model

The wrist model considered here is a universal joint with two skew-oblique axes as shown in Figure 4.3 [5; 68]. The unit vector $\boldsymbol{\omega}_{FE}$ represents the FE axis and is fixed proximally on the forearm. The unit vector $\boldsymbol{\omega}_{RUD}$ represents the RUD axis and is fixed on the hand [14]. The two axes do not intersect as they are separated by a few millimeters (distance Δ) [53] and approximately perpendicular, with subject-specific variations. The Range of Motion (RoM) of the joint angles is considered as Table 3.1.

As shown in Figure 4.3.a, two principal frames are defined based on the position of two electromagnetic sensors S1 and S2 (Liberty System from Polhemus Technologies Inc). Sensor S1 is fixed with respect to the forearm while S2 is fixed with respect to the hand. Since the method should be non-invasive, only approximate sensor attachment is possible due to skin motion. Sensor S1 is rigidly

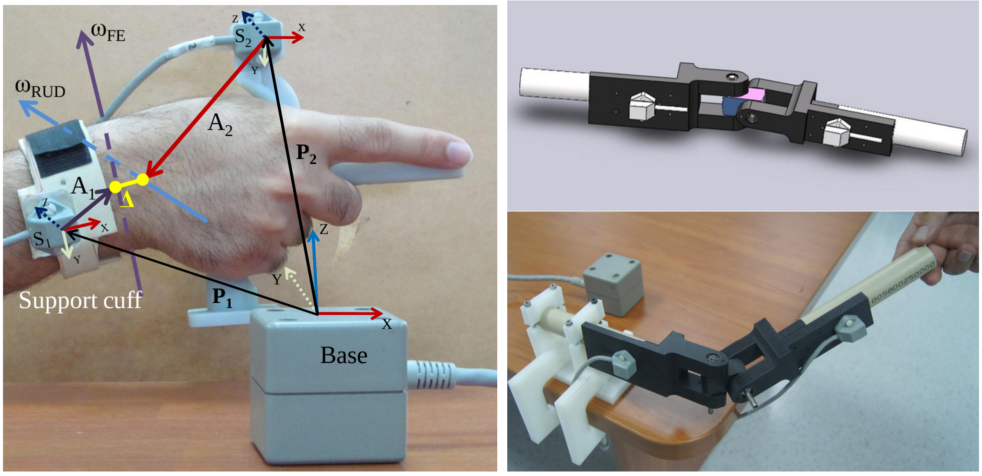

a) b)

Figure 4.3: Axes of rotation in the wrist joint in human wrist (a) and mechanical mock-up counterparts (b). $\boldsymbol{P}_1$ and $\boldsymbol{P}_2$ are the position vectors of the sensor S_1 on the forearm and S_2 on the 3rd metacarpal in the stationary frame, *Base*; $\boldsymbol{A}_1$ and $\boldsymbol{\omega}_{FE}$ are the position vector and orientation of the FE axis relative to the S_1; $\boldsymbol{A}_2$ and $\boldsymbol{\omega}_{RUD}$ are the position vector and orientation of the RUD axis relative to the S_2 pointing to the minimal distance Δ between the two axes. Details on the design and kinematics of the devices are provided in Section 4.3.3.

mounted on a support cuff wrapped around the forearm, just before the styloid process, while S2 is rigidly mounted on the handle. The support cuff was developed with regard to repeatability, ease of placement, and comfort for the subject; I thus considered the bony landmarks of the forearm, i.e., the styloid process of the radius and ulna bones, as reliable fixation points to ensure repeatability when wearing the sensor in each experiment. $3.2mm$ Luxafoam, a thin soft padding, was applied to the inner side of the support cuff for increased comfort. Thermoplastic material was used for the exterior of the cuff to assure a stable seat for the sensor. To avoid cumulative trauma disorders of the wrist, I developed a comfortable handle, the '*ComfGrip*, inspired by the fencing-grip design which evolved over centuries to provide a stable grasp.

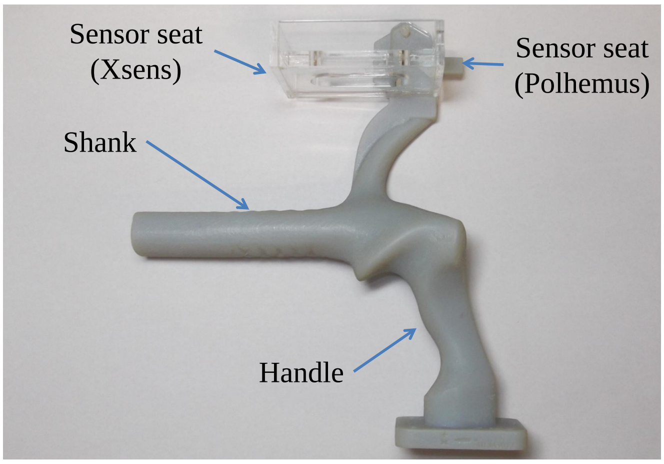

Figure 4.4: ComfGrip, the handle designed to be held in a unique and comfortable manner.

To hold ComfGrip, the little, ring and middle fingers rest on the handle and index finger rests along the shank, providing a comfortable and unique way of grasping. A sensor seat was also included on ComfGrip for mounting Sensor S2 (Figure 4.4). Each sensor provides readings of its own orientation and position (6 Degrees-of-Freedom) with respect to a reference frame (Base, in Figure 4.3) at a rate of 240 samples per second.

The FE axis $\boldsymbol{\omega}_{FE}$ is fixed with respect to the forearm and so its position $\boldsymbol{A}_1$ with respect to sensor S1 is constant. Similarly, $\boldsymbol{\omega}_{RUD}$ is fixed with respect to the hand and so that its position $\boldsymbol{A}_2$ from S2 is constant. According to the anatomical structure of the wrist, I defined an additional frame (f_{FE}). Its x-axis is aligned with $\boldsymbol{\omega}_{FE}$, its z-axis is aligned with $\boldsymbol{\omega}_{FE} \times \boldsymbol{\omega}_{RUD}$ (where $\times$ is the standard vector product), i.e., perpendicular with both FE and RUD axes, and its y-axis is defined via the right-hand rule. A bold symbol $\boldsymbol{X}$ indicates a space vector and $\boldsymbol{X}^{(F)}$ indicates its coordinates with respect to a frame F.

Following standard robotics approaches [64], the transformations between the above defined reference frames could be defined, with the convention that a symbol ${}^{A}T_{B}$ indicates a 4 × 4 homogeneous transformation matrix from a frame B into a frame A, a bold symbol $\boldsymbol{X}$ indicates a space vector and $\boldsymbol{X}^{(F)}$ indicates its coordinates with respect to a frame F.

In ambulatory conditions, sensors S1 and S2 will provide time-varying readings ${}^{B}T_{S1}$ and ${}^{B}T_{S2}$, respectively:

$$
{}^{B}T_{Si} = \begin{bmatrix} R_i & \boldsymbol{P}_i^{(B)} \\ 0\ 0\ 0 & 1 \end{bmatrix} \tag{4.1}
$$

where $i = 1, 2$, R_i is the rotation matrix and $\boldsymbol{P}_i^{(B)}$ the position of sensor S_i with respect to the base (B).

Nevertheless, such readings will not be independent because of the kinematic relationship between the two sensors:

$$
{}^{B}T_{S2} = {}^{B}T_{S1}\ {}^{S1}T_{f_{FE}}\ {}^{f_{FE}}T_{S2} \tag{4.2}
$$

Following [64] ${}^{S1}T_{f_{FE}}$, ${}^{f_{FE}}T_{S2}$ in (4.2) are defined as :

$$
\begin{aligned}
{}^{f_{FE}}T_{S2}(\theta_{RUD}) &= \exp\left(\widehat{\xi}_{RUD}\theta_{RUD}\right) {}^{f_{FE}}T_{S2}(0) && (4.3)\\
{}^{S1}T_{f_{FE}}(\theta_{FE}) &= \exp\left(\widehat{\xi}_{FE}\theta_{FE}\right) {}^{S1}T_{f_{FE}}(0) && (4.4)
\end{aligned}
$$

where the exponential $\exp \widehat{\xi}\theta$ in (4.3)-(4.4) defines a *screw motion* generated by a *twist* $\widehat{\xi}$ as represented in Section 3.1.1. $\widehat{\xi}$, operatively defined as

$$
\widehat{\xi} = \begin{bmatrix} \widehat{\omega} & \boldsymbol{v} \\ 0 & 0 \end{bmatrix} = \begin{bmatrix} \widehat{\omega} & -\boldsymbol{\omega} \times \boldsymbol{q} + h\boldsymbol{\omega} \\ 0 & 0 \end{bmatrix} \tag{4.5}
$$

where $\boldsymbol{\omega}$ is the unit vector of a rotation axis, q is any point on the axis, h is the pitch[1], and $\boldsymbol{v} = -\boldsymbol{\omega} \times q + h\boldsymbol{\omega}$.

For rotational axes ($\boldsymbol{\omega} \neq \mathbf{0}$) the exponential is computed as

$$e^{\widehat{\xi}\theta} = \begin{bmatrix} e^{\widehat{\omega}\theta} & (I - e^{\widehat{\omega}\theta})(\boldsymbol{\omega} \times \boldsymbol{v}) + \boldsymbol{\omega}\boldsymbol{\omega}^T \boldsymbol{v}\theta \\ 0 & 1 \end{bmatrix} \tag{4.6}$$

Table 4.1 provides the parameters used for the numerical calculations.

Table 4.1: Parameters for the screw motion calculation.

	$\boldsymbol{\omega}$	q	${}^{A}T_{B}(0)$
${}^{S1}T_{f_{FE}}$	$\begin{bmatrix} 0 \\ -1 \\ 0 \end{bmatrix}$	$\begin{bmatrix} A_{1x} \\ A_{1y} \\ A_{1z} \end{bmatrix}$	$\left[\begin{array}{ccc\|c} 0 & 0 & 1 & A_{1x} \\ -1 & 0 & 0 & A_{1y} \\ 0 & -1 & 0 & A_{1z} \\ \hline \multicolumn{3}{c\|}{0} & 1 \end{array}\right]$
${}^{f_{FE}}T_{S2}$	$\begin{bmatrix} 0 \\ -1 \\ 0 \end{bmatrix}$	$\begin{bmatrix} \Delta_x \\ \Delta_y \\ \Delta_z \end{bmatrix}$	$\left[\begin{array}{ccc\|c} 0 & 1 & 0 & \Delta_x - A_{2y} \\ 0 & 0 & 1 & \Delta_y - A_{2z} \\ 1 & 0 & 0 & \Delta_z - A_{2x} \\ \hline \multicolumn{3}{c\|}{0} & 1 \end{array}\right]$

Considering that the position vectors $\boldsymbol{A}_1$ and $\boldsymbol{A}_2$ are constant when expressed with respect to S1 and S2, respectively, I can define constant components:

$$\boldsymbol{A}_1^{(S1)} := \begin{bmatrix} A_{1x} \\ A_{1y} \\ A_{1z} \end{bmatrix}; \; \boldsymbol{A}_2^{(S2)} := \begin{bmatrix} A_{2x} \\ A_{2y} \\ A_{2z} \end{bmatrix}; \tag{4.7}$$

with respect to frames (S1) and (S2), the distance between the FE and RUD axes is defined as:

$$\boldsymbol{\Delta} = \Delta \frac{\boldsymbol{\omega}_{FE} \times \boldsymbol{\omega}_{RUD}}{|\boldsymbol{\omega}_{FE} \times \boldsymbol{\omega}_{RUD}|} \tag{4.8}$$

---

[1] For purely rotational joints, like my mechanical mock-up, h = 0.

with

$$\boldsymbol{\Delta}^{(f_{FE})} = \begin{bmatrix} \Delta_x \\ \Delta_y \\ \Delta_z \end{bmatrix} \tag{4.9}$$

The goal of the calibration will be to accurately estimate $\boldsymbol{A}_1^{(S1)}$, $\boldsymbol{A}_2^{(S2)}$, $\boldsymbol{\omega}_{FE}^{(S1)}$, $\boldsymbol{\omega}_{RUD}^{(S2)}$ and Δ.

4.2.2 Parameter Estimation

Referring to Figure 4.3, the following invariant (i.e. frame independent) geometric relation holds:

$$\boldsymbol{P}_2 - \boldsymbol{P}_1 = \boldsymbol{A}_1 + \boldsymbol{\Delta} - \boldsymbol{A}_2 \tag{4.10}$$

Vectors $\boldsymbol{P}_1$ and $\boldsymbol{P}_2$ are conveniently expressed in base frame (B) coordinates, as the sensors directly measure $\boldsymbol{P}_1^{(B)}$ and $\boldsymbol{P}_2^{(B)}$. Vector $\boldsymbol{A}_1$ and $\boldsymbol{\omega}_{FE}$ are unknown but, being fixed onto the forearm, their coordinates $\boldsymbol{A}_1^{(S1)}$ and $\boldsymbol{\omega}_{FE}^{(S1)}$ with respect to the frame S1 are constant. Similarly, $\boldsymbol{A}_2^{(S2)}$ and $\boldsymbol{\omega}_{RUD}^{(S2)}$ are unknown but constant vectors.

For numerical calculations, I prefer to express (4.10) with respect to the base frame (B). Orientation matrices R_1 and R_2 from, respectively, sensors S1 and S2 can be used to transform coordinates from (S1) or (S2) to (B), e.g. for a general vector:

$$\boldsymbol{X}^{(B)} = R_1 \boldsymbol{X}^{(S1)} = R_2 \boldsymbol{X}^{(S2)} \tag{4.11}$$

Furthermore, due to inherent measurement noise, equation (4.10) will not hold exactly. Thus

$$\epsilon = \left| \boldsymbol{P}_2^{(B)} - \boldsymbol{P}_1^{(B)} - \boldsymbol{A}_1^{(B)} - \boldsymbol{\Delta}^{(B)} + \boldsymbol{A}_2^{(B)} \right|$$

and after a change of coordinates as in (4.11):

$$0 < \epsilon(t) = \left| \boldsymbol{P}_2^{(B)} - \boldsymbol{P}_1^{(B)} - R_1 \boldsymbol{A}_1^{(S1)} - \Delta \frac{R_1 \boldsymbol{\omega}_{FE}^{(S1)} \times R_2 \boldsymbol{\omega}_{RUD}^{(S2)}}{\left| R_1 \boldsymbol{\omega}_{FE}^{(S1)} \times R_2 \boldsymbol{\omega}_{RUD}^{(S2)} \right|} + R_2 \boldsymbol{A}_2^{(S2)} \right| \tag{4.12}$$

where ϵ is a small scalar accounting for possible measurement errors at a given time t. It should be noted that all terms in equation (4.12) are either directly measured from the sensors ($\boldsymbol{P}_1^{(B)}$, $\boldsymbol{P}_2^{(B)}$, R_1, and R_2) or as unknown constants: one scalar Δ, two position vectors $\boldsymbol{A}_1^{(S1)}$, $\boldsymbol{A}_2^{(S2)}$, and two axes $\boldsymbol{\omega}_{FE}^{(S1)}$, $\boldsymbol{\omega}_{RUD}^{(S2)}$). Each position vector results in 3 unknown scalar parameters.

Guided by the clinical nature of this application, sensors S1 and S2 were mounted on the dorsal part of the forearm and hand, respectively, with the wires directed proximally (see Figure 4.3). For the specific case of Polhemus sensors, the sensor x-axis (aligned with the wire) is roughly aligned with the main axes of the forearm for S1 and the hand for S2. The z-axis of each sensor points volarly (Figure 4.3). With this convention, I can define vectors of unit length (using only two parameters) as follows:

$$\boldsymbol{\omega}_{FE}^{(S1)} := \frac{1}{\sqrt{1+\alpha_1^2+\beta_1^2}} [\alpha_1 \;\; 1 \;\; \beta_1]^{-1} \tag{4.13}$$

$$\boldsymbol{\omega}_{RUD}^{(S2)} := \frac{1}{\sqrt{1+\alpha_2^2+\beta_2^2}} [\alpha_2 \;\; \beta_2 \;\; 1]^{-1} \tag{4.14}$$

Similarly to [5], for a given set of measurements acquired during a time $t \in [0\ T]$, I can determine the 11 parameters by solving a least-squares problem[1]

$$p^* := \underset{p \in \mathbb{R}^{11}}{\operatorname{argmin}} \frac{1}{T} \int_0^T \epsilon^2 \, dt \tag{4.15}$$

where $p := [A_{1x}\ A_{1y}\ A_{1z}\ A_{2x}\ A_{2y}\ A_{2z}\ \alpha_1\ \beta_1\ \alpha_2\ \beta_2\ \Delta]^T$ and ϵ is from (4.12). To assess the accuracy and repeatability of each method in estimating a generic parameter A, I use the relative error e_A, defined as

$$e_A = \frac{||\hat{\boldsymbol{A}} - \boldsymbol{A}||}{||\boldsymbol{A}||} \tag{4.16}$$

where $\hat{\boldsymbol{A}}$ is the estimated value of parameter A obtained from direct measurement at the mock-up and $||\boldsymbol{A}||$ is the Euclidian norm of parameter A.

4.2.3 Numerical assessment of accuracy of kinematic model fitting

For a given circle, only three distinct points on the circle are needed to geometrically identify its centre. However, in the presence of noisy measurements it is necessary to use a large number of points distributed along a circular arc. The larger the angle subtended by the circular arc, the better is the accuracy of the estimation. For a 1-DoF rotational joint, the largest possible arc is limited by the range of motion which for human joints is bounded by physiological limits. These limits might have important consequences on the accuracy of an algorithm meant for clinical applications.

---

[1] Numerically solved via the function `lsqnonlin` in MATLAB.

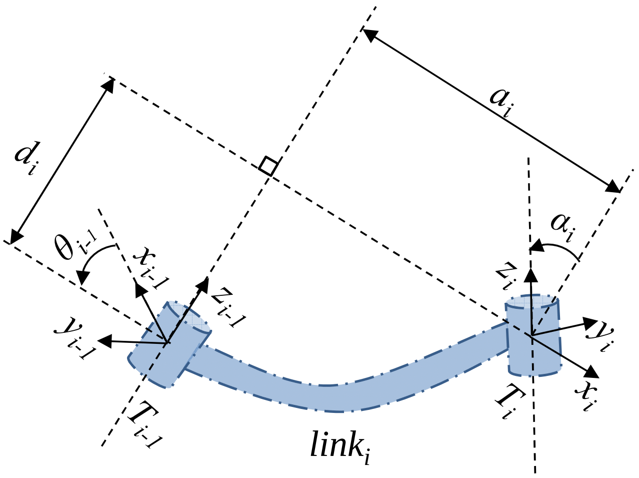

Figure 4.5: Standard form of Denavit-Hartenberg notation.

For 2-axis joints such as the human wrist, both the range of motion of each joint and any covariation between joints may have an influence. When a patient's wrist is manually moved by a therapist, It cannot be assume that only one joint moves at a time. To study the effects of the range of motion, noisy data, and joint covariation on the estimation of the geometry of a 2-joint wrist, a sequence of wrist motion data was numerically generated via the wrist kinematic model, through a sequence of joint angles $\theta_{FE}^{(n)}$ and $\theta_{RUD}^{(n)}$, where n is the discrete time index.

Using the Denavit-Hartenberg (DH) standard notation [19], I described the wrist model as presented in Table 4.2.

As it is illustrated in Figure 4.5, considering the $link_i$ connects the revolute joint $i-1$ to the revolute joint i, the notation used in Table 4.2 would be described as follows:

link length (α_i) the distance between the z_{i-1} and z_i axes along the x_i axis;

link twist (a_i) the angle from the z_{i-1} axis to the z_i axis about the x_i axis;

Table 4.2: Denavit-Hartenberg parameters for wrist model.

Joint	α_i[rad]	$a_i[mm]$	θ_i[rad]	$d_i[mm]$	type
1	$-\pi/2$	0	0	0	dummy
2	π	143	0	0	PS
3	$\pi/2$	0	0	0	dummy
4	$\pi/2$	0	0	22.3	FE
5	0	11.25	0	0	dummy
6	π	0	0	0	dummy
7	0	0	0	21.75	RUD
8	0	68	0	0	3^{rd}metacarpal

link angle (θ_i) the angle between the x_{i-1} and x_i axes about the z_{i-1} axis;

joint offset (d_i) the distance from the origin of frame $i-1$ to the x_i axis along the z_{i-1} axis.

Figure 4.5, illustrates the standard form of DH notation. The DH parameters via the function `robot` from robotics toolbox [16] is used to generate the wrist model as illustrated in Figure 4.6.a. The *dummy* links in Table 4.2 are used to make the DH links compatible with the robotics toolbox in order to generate a model with the correct configuration. Using the function `fkine`, I then calculated a sequence of homogeneous transformation matrices, through the sequence of joint angles $\theta_{FE}^{(n)}$ and $\theta_{RUD}^{(n)}$, from which I extracted matrices R_1 and R_2 to be used in equations (4.12) and (4.15).

Figure 4.6.a depicts the simulated wrist model and its workspace, assuming the right hand pointing straight ahead with palm looking left and thumb pointing up. Figure 4.6.b. shows the pure (blue lines), covariated-noisy (black lines) and circumduction (red line) movements used in parameter estimations which are generated by this wrist model.

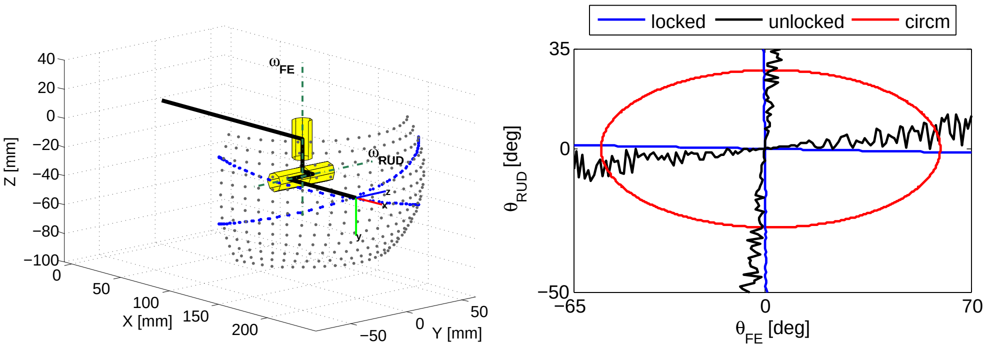

a) b)

Figure 4.6: Simulated wrist joint (a) and different rotation trajectories (b) for parameter estimation.

A pure FE movement is generated by keeping $\theta_{RUD}^{(n)} = 0$ while varying the FE joint angle $\theta_{FE}^{(n)}$. In particular, for a given number of samples N_s, $\theta_{FE}^{(n)}$ assumes N_s equally spaced values within its range of motion and $n = 1, \ldots, N_s$. Similarly, for pure RUD movements, the FE joint angle is kept fixed while the RUD joint angle is varied between N_s equally spaced values within the RUD range of motion.

I simulated the effect of joint covariations by admitting motion for the joint supposedly held fixed. For example, for pure FE movements, I allowed $\theta_{RUD}^{(n)} = c\,\mu^{(n)}\,\theta_{FE}^{(n)}$, where c is a coefficient of covariation ($c = 0$ denotes a pure FE movement) and $\mu^{(n)}$ is a sequence of random numbers equally distributed between zero and one. A similar procedure was adopted for the RUD movements.

To simulate the effect of noisy measurements, I added noise ($\delta R^{(n)}$) to the orientation readings from the sensors, $R^{(n)}$, by $R_{noise}^{(n)} := \delta R^{(n)} R^{(n)}$. Three levels of angular RMS noise: 0.15°, 0.30° and 0.45° are considered. The 0.15° level corresponds to the static accuracy orientation for the Polhemus Liberty System.

Finally, I simulated the effect of the natural range of motion (RoM) and also 80%, 60%, 40% and 20% of RoM on parameter estimation. The simulated movement was in such a way that starting from the maximum point of wrist flexion, I simulated a rotation of hand about the FE axis toward the point of maximum wrist extension and then move the hand back to its original position of maximum flexion for ten times, the same rotations were simulated about the RUD axis starting from maximum radial to maximum ulnar range of motion. For these simulations, $c = 20\%$ is used. Contamination from noise in the angular signal with an RMS value of $0.15°$ is also considered.

Then both methods M1 and M2 are used to estimate the model parameters (A_1, A_2 and Δ) from sequences of FE and RUD movements affected by different levels of joint covariations, noise, range of movements as well as by different number of samples N_s.

4.2.4 Experimental assessment of accuracy of fitted kinematic model

In order to estimate accuracy of the fitted method, the ground-truth must be known. For this reason, I used the mock-up shown in Figure 4.3.b which structurally resembles a human wrist (i.e. two perpendicular and non intersecting axes) with known dimensions. It should be noted that experiments with a mechanical mock-up are not influenced by skin motion, leading to fitting outcomes which solely depend on the quality of the sensors (e.g. noise levels and accuracy), the experimental protocol (e.g. range of motion), and the fitting method itself.

I conducted two batches of experiments in two different conditions. For each experiment, one subject was asked to manually move the mock-up (as if it were a patient's wrist, according to specific instructions described below) while the

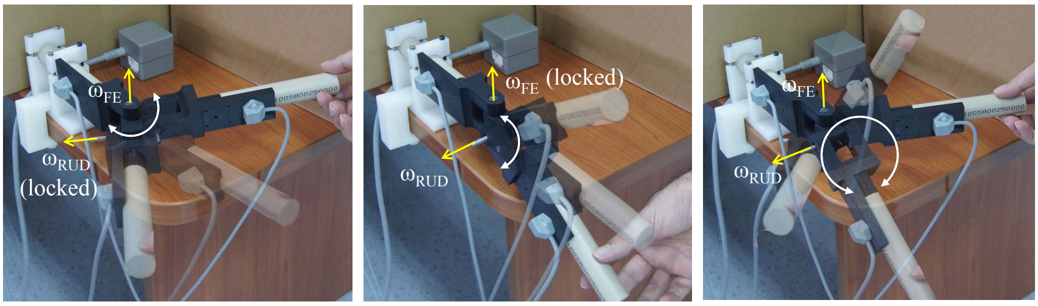

a) b) c)

Figure 4.7: Three typical movement conditions, a)*Restricted-locked* FE movement, b)*Restricted-locked* RUD movement and c)*Restricted-circum*.

corresponding sequences of sensor readings were sampled at 240 Hz.

Experiment 1 (restricted)

The mock-up was mounted on a table, simulating the restricted condition. In this case sensor S1 is stationary, providing constant readings. Three types of movements were performed:

Restricted-locked: one axis at a time was mechanically locked (with ad-hoc screws) while the subject was asked to perform 10 rotations with the other DoF throughout the complete range of motion (see 4.7.a, b).

Restricted-unlocked: the subject was asked to perform a set of movements similar to those of *Restricted-locked* on one axis at a time while the other DoF was mechanically unlocked. Despite the specific instruction to perform single axis movements, the subject would unavoidably elicit movements in both axes at the same time.

Restricted-circum: the subject was asked to induce circumduction movements of the wrist (both mock-up axes were unlocked, see see 4.7.c).

Experiment 2 (unrestricted)

The subject was instructed to perform movements as in *Restricted-unlocked* and *Restricted-circum* while holding the whole mock-up in his own hands. In particular, the mock-up forearm was no longer strapped onto the table, corresponding to an unrestricted condition (readings from sensor S1 were no longer constant).

Each batch of experiments in both limited ranges of motion and in the natural RoM are conducted. For each motion, the sequence of sensor readings was recorded and the method of Section 4.2.2 was used to estimate the desired parameters of the mock-up (i.e. $\boldsymbol{A}_1$, $\boldsymbol{A}_2$, $\boldsymbol{\omega}_{FE}$, $\boldsymbol{\omega}_{RUD}$, Δ).

4.2.5 Results

Synthetic data

Using the described synthetic data, the influence of joint covariation, noise and number of samples and range of motion are evaluated on the accuracy of parameter estimation by methods M1 and M2. Figure 4.8.a shows the effect of joint covariation on parameter estimation on both methods, for different levels of noise when a large number of samples was acquired (Ns=2500). Because of the large number of samples, both methods are rather insensitive to noise levels but Method M1 is highly sensitive to the covariation index. In particular, Method M1 displays a parabolic increase of accuracy error for small covariations (0-20%) and linear afterwards, while method M2 is accurate (almost zero accuracy error) throughout the whole range of covariations (0-40%).

On the other hand, as shown in Figure 4.8.b, both methods M1 and M2 are sensitive to the noise for smaller numbers of samples (Ns $\leq$ 2000), only for larger

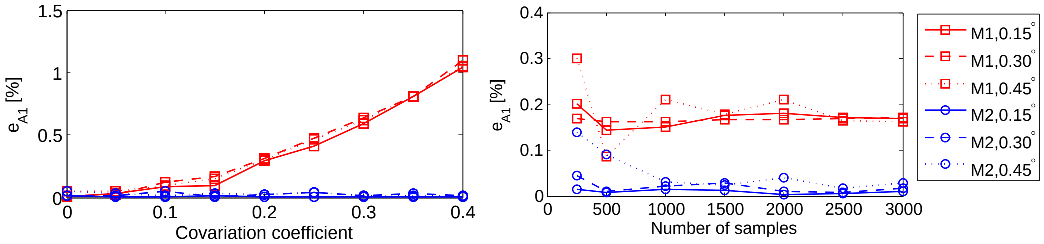

a) b)

Figure 4.8: The effect of joint covariation (a) and the number of samples (b) on relative error in estimations of methods M1 (squares) and M2 (circles). The solid line, dashes and dots present 0.15°, 0.30° & 0.45° angular RMS noise.

samples (Ns $\geq$ 2500) the effect of noise on measurements is averaged out.

Figure 4.9 shows the relative error for Δ. For 40% of RoM up to the whole RoM, the error is less than 0.5% for M2. Comparing the estimation error of the method M2 with M1 shows that M2 has at least 60% less error in parameter estimation than the previous method.

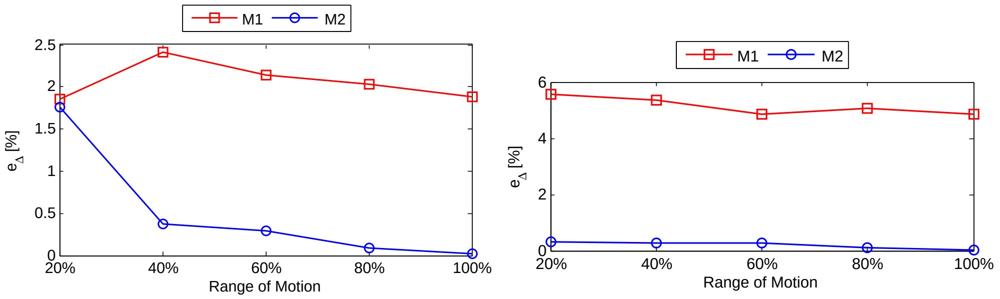

a) b)

Figure 4.9: The effect of different ranges of motion and joint covariation on parameter estimation. Relative error in estimations of methods M1 (squares) and M2 (circles) in the presence of 20% (a) and 30% (b) joint covariation.

These preliminary numerical results demonstrate the robustness of the method M2 with respect to method M1. Method M2 requires joint covariation and provides more accurate estimations (i.e., lower relative error) as the range of motion increases. Method M1 is strongly limited by the joint covariation. As it is illustrated in Figure 4.9, in the specific case of 20% joint covariation, the relative error will not decrease by increasing the range of motion. For the case of 30% joint covariation, the relative error for estimations of method M1 is twice larger than its estimations for 20% covariation. Furthermore, the relative error for estimations of method M2 is smaller than the previous case.

Experimental data

Experimental data were obtained with a mock-up to examine the joint covariation induced by manually moving a joint which is kinematically similar to the human wrist. Figure 4.10 shows the joint-space representation of induced wrist movements. I chose these movements as they are the physiological movements available at the wrist, i.e., the wrist can perform F/E, UD/RD, or combined movements available at the wrist joint. Assessment of normal joint range and exercises to regain physiological movements is incorporated into treatment regimes following musculoskeletal or neurological injury. For a strapped forearm, I considered the pure rotations about either of the axes in a limited and wide RoM, i.e. 'locked-short' range and 'locked-wide' range, respectively, in Figure 4.10. To study the effect of weakness and poor motor control[1] seen following neurological injury I imposed fluctuated movements ('unlocked-fluct') as shown in Figure 4.10 for both strapped forearm and unrestricted conditions.

Moreover, in the absence of locking mechanisms (screws for my mock-up, or possibly ad-hoc splinting for the human wrist) a joint covariation less than 20%

---

[1] Following stroke, the most frequent problems are weakness and lack of co-contraction around the joint. Over time, spasticity can develop or soft tissue can change which would cause stiffness in the muscle [9].

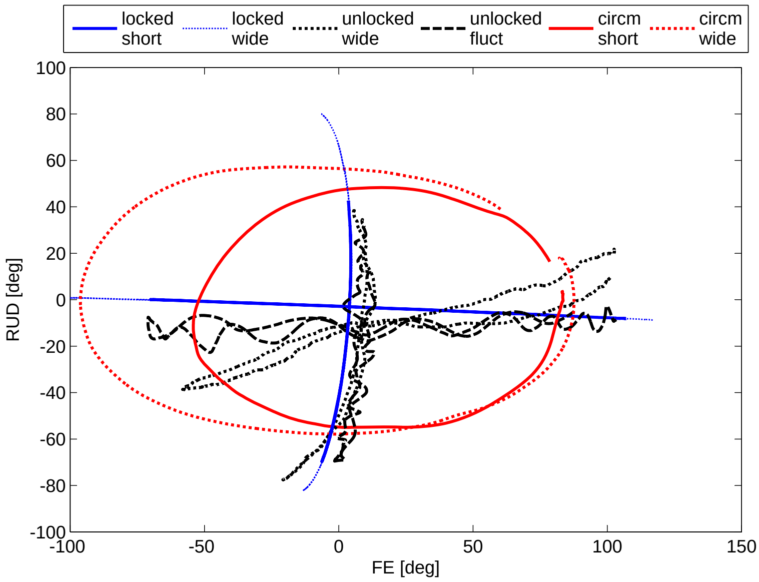

Figure 4.10: Different imposed joint rotations for parameter estimation.

was induced by manual motion of the wrist[1]. For the sake of clarity, Figure 4.10 shows the trajectory of one representative movement out of the 10 in six different conditions. In the locked condition (solid and dotted blue lines) the movements are perfectly superimposed. However, some deviation in the single axis movements could be seen. This deviation resulted from the loose mechanical lockage which could not completely lock the other joint. Figure 4.6.b, shows the same phenomenon for the numerical simulation. The lockage mechanism will be improved to avoid future errors. For the single-joint but unlocked condition (dotted and dashed black lines) a 5% joint covariation is observed. A similar variability is present in the circumduction movements (dashed lines). Different RoMs for each condition are obvious.

Another feature is demonstrated in the centre of the crosses relative to the un-

---

[1] From experimental data, a covariance as large as 20% is noticed that could appear also in movement intended to be mono-axial.

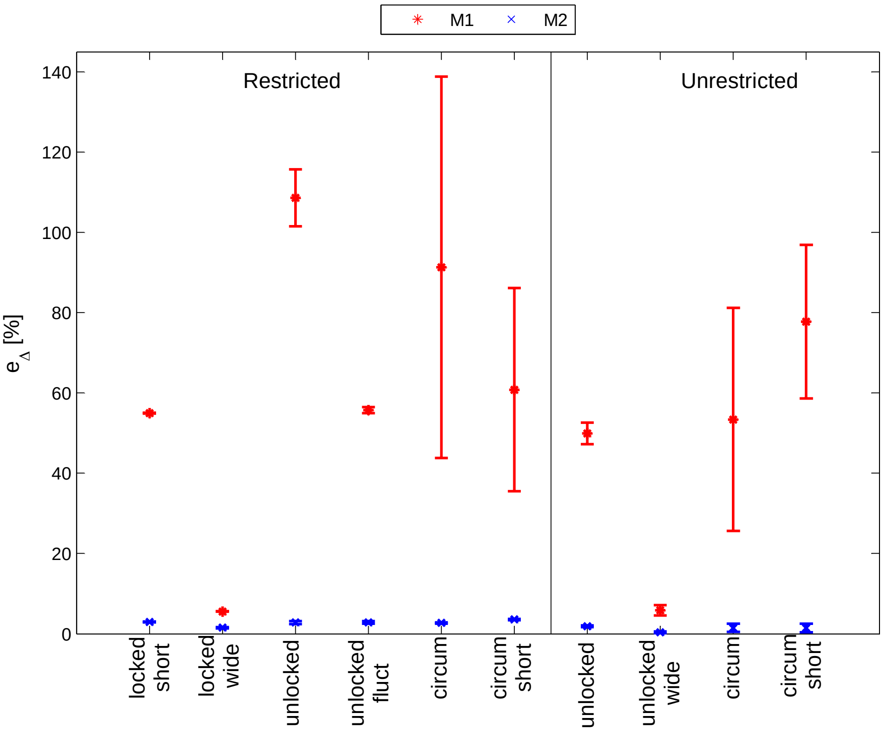

Figure 4.11: Mean and standard deviation of relative error, respectively as an index for accuracy and repeatability, in estimating Δ, as a representative parameter of the physical mock-up in 'Restricted' and 'Unrestricted' conditions, imposing locked-short, locked-wide, unlocked-wide, unlocked-fluctuation, circumduction-short and circumduction-wide rotations for M1 (red stars) and M2 (blue crosses).

locked movements. This also displays a 5% variability, indicating that manual movement will also result in a repeatability error when returning to the 'zero-position.'

The mean and standard deviation of the relative error for each trial are calculated to evaluate the accuracy (mean) and repeatability (standard deviation) of the both methods in the parameter estimation. The maximum relative error on estimation is less than 3.6% for M2, showing a promising accuracy for this method, while the least relative error for M1 is 6% for locked wide RoM, see Figure 4.11. For M2, the relative error in the parameter estimation for the limited RoM seems more than the wide RoM while the lowest amount of error is presented for unrestricted condition with a wide RoM (Figure 4.11). Comparing the error for the restricted condition with covariation and fluctuated movements shows almost the same error for both of the covariation and fluctuated movements for M2 estimations (Figure 4.11). Method M1 exhibits the highest error for fluctuated and circumduction movements. Table 4.3, explicitly represents the percentage of relative error for the representative parameter Δ, for more precise comparison.

Table 4.3: Mean and standard deviation of relative error in estimating Δ, as a representative parameter of the physical mock-up.

Movement condition		mean±SD of relative error (%)	
		M1	M2
Restricted	locked-short	54.94±0.11	2.98±0.09
	locked-wide	5.58±0.08	1.51±0.15
	unlocked	108.61±7.06	2.82±0.37
	unlocked-fluctuated	55.69±0.75	2.85±0.32
	circumduction	91.31±47.52	2.72±0.17
	circumduction-short	60.83±25.30	3.56±0.15
Unrestricted	unlocked	49.92±2.70	1.84±0.20
	unlocked-wide	5.88±1.31	0.34±0.23
	circumduction	53.41±27.79	1.47±1.02
	circumduction-short	77.78±19.15	1.48±1.09

4.3 Ergonomic exoskeleton design from subject-specific kinematic model

In this section I describe how the wrist kinematic model generated through the procedure explained in this chapter, could be used to develop an ergonomic exoskeleton, named *ErgoExo*.

4.3.1 Protocol

As demonstrated in the results of the previous section, the recordings taken from movements in an unrestricted condition lead to the most accurate parameter estimation (see Figure 4.11). This feature is used as the basis for achieving accurate parameter estimation. Specifically, the subject was asked to wear sensors as depicted in Figure 4.3 and perform the following movements:

- *One joint at a time (unrestricted movement):* similar to *Restricted-unlocked* in 4.2.4, starting from the maximum point of wrist flexion, the subject was asked to rotate his or her hand about the FE axis toward the point of maximum wrist extension and then move the wrist back to its original position of maximum flexion. After performing this rotation ten times, the same rotations were performed about the RUD axis starting from maximum radial to maximum ulnar range of motion.

- *Circumduction:* using both the FE and RUD joints, the subject was instructed to rotate his hand about the PS axis as if tracing an imaginary circle for ten times.

Note: During experiments, the subject was asked to be seated, holding his upper arm beside his trunk (in the coronal plane) and his forearm horizontal (in the transverse plane).

4.3.2 Data analysis

For each experiment, the sequence of sensor readings was recorded and method M2 discussed in Section 4.2.2 was used to estimate the desired parameters of the wrist. The estimated parameters are presented in Table 4.4.

Table 4.4: Estimated parameters for human wrist

Parameter	mean ± standard deviation (mm)
A_1	$[48.5 \pm 1.19 \;\; -5.3 \pm 1.41 \;\; 43.8 \pm 0.51\;]^T$
A_2	$[-60.4 \pm 1.00 \;\; 60.2 \pm 1.41 \;\; 18.3 \pm 0.67\;]^T$
Δ	4.3±0.81

4.3.3 Design of an ergonomic exoskeleton

A 3D scan of the hand holding the ComfGrip was acquired using an Artec^{TM}Eva camera. The complete 3D scan of the hand was imported into SolidWorks (Dassault Systèmes SolidWorks Corp) to make a precise solid model of the hand wearing the sensors see Figure 4.12.a. The estimated parameters for the wrist, presented in Table 4.4, were transferred to the solid model to determine the exact positions of the wrist rotation axes, i.e. FE_{wrist} and RUD_{wrist}, Figure 4.12.b. This procedure resulted in positioning the exoskeleton's rotation axes aligned with corresponding wrist axes. Confirming the exoskeleton's rotation axes, Figure 4.12.c, the other required linkages were designed to connect FE_{exo} and RUD_{exo} axes to ComfGrip, Figure 4.12.d. This exoskeleton is considered ergonomic because its rotation axes are perfectly aligned with the corresponding wrist axes and its handle is comfortable to grasp for long periods of time. Figure 4.12.e demonstrates the prototype of the exoskeleton manufactured by means of rapid-prototyping technology. Obviously, this procedure is subject-specific.

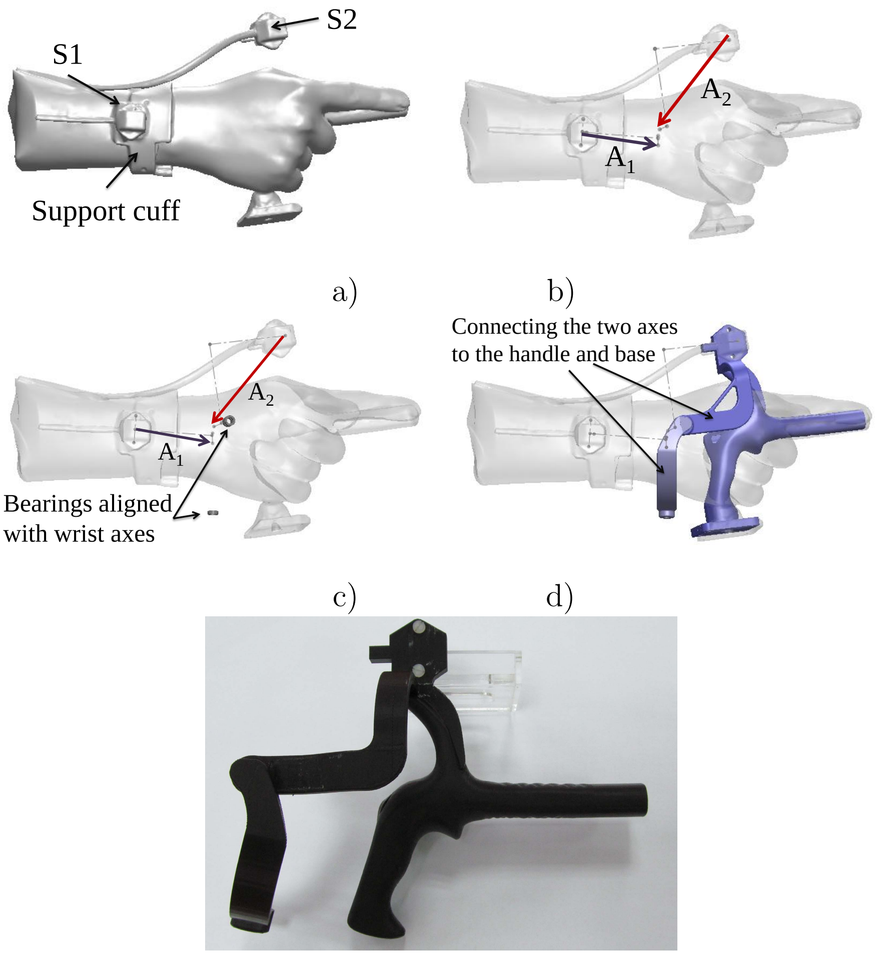
S2
S1
Support cuff
A_2
A_1
A_2
A_1
Bearings aligned with wrist axes
Connecting the two axes to the handle and base

a) b)

c) d)

e)

Figure 4.12: Procedure to design and manufacture a subject specific, ergonomic wrist exoskeleton *ErgoExo* (e). A 3D scan of the subject's hand is imported into Solidworks (a). The position of wrist rotation axes A_1 and A_2 are transferred to the Solidworks environment and used to align the exoskeleton's rotation axes with the corresponding wrist axes (b, c). Finally, the required complementary linkages are designed (d).

4.4 Conclusion

This chapter proposed a method to determine subject-specific kinematics of the wrist. To evaluate the accuracy of the proposed method, I considered two different movement conditions, i.e. *restricted* and *unrestricted* movements, joint covariation, number of samples, noise as well as different ranges of motion on the estimations of the adapted method. A physical mock-up with known dimensions, enabling comparison between the estimated and actual values, was used to assess the accuracy and repeatability of the parameter estimation method. The mean (accuracy) and standard deviation (repeatability) of relative errors for the parameter estimation for both movement conditions were computed.

For method M1, which assumes pure single-joint motions, the accuracy error increases with joint covariation while method M2 is insensitive to joint covariation, see Figure 4.8.a. However, for lower number of samples (less than 2500 per movement) both methods are sensitive to noise in measurements, as shown in Figure 4.8.b.

The experimental results exhibited much better accuracy for wide range unrestricted movements with covariations for the new method M2 (Figure 4.11). I also observed that the accuracy in estimating parameters through M2 for limited RoM with small fluctuations in *restricted* condition is 10% has greater accuracy for the same condition when one joint is moved at a time (see the relative error for restricted 'unlocked-fluct' and 'locked-short' in Figure 4.11). I performed uncontrolled (fluctuated) movements to replicate conditions seen following neurological injury.

The promising results of these experiments suggest that this method may be a useful tool to assess wrist movement following musculoskeletal and neurological injury. Overall, comparing the mean relative error for all restricted conditions with unrestricted conditions for M2 shows a 45% higher accuracy for the latter. This makes the new method especially suitable for unconstrained conditions in which higher variability in the joint space (e.g. joint covariation or fluctuations) induces better accuracy in parameter estimation.

Chapter 5

Influence of Kinematic Compatibility on Human-Robot Interaction

The influence of kinematic compatibility, i. e. the alignment between human and robot joints, on reaction forces and human motor strategies has been addressed in this chapter in three main sections.

In the first section, I present a numerical study on the interaction forces and discomfort due to misalignments with the human joints in an anthropomorphic exoskeleton. In particular, I evaluate the response of the exoskeleton in terms of kinematic mismatch and reaction forces in wrist joint by simulating imposed movements at the human joints. I discuss the kinematic discrepancy as well and suggest a one-size-fits-all exoskeleton based on the aggregate loss minimization concept.

Afterwards, in the second section, using the exoskeleton presented in chapter 4, in an experimental study I discuss the effect of the kinematic compatibility on the natural coordination mechanisms in the redundant wrist. Human sensorimotor control is known to impose intrinsic kinematic constraints to solve redundant motor tasks. To this end, the effect of an exoskeleton on natural motor strategies was assessed during pointing tasks performed with the wrist. The exoskeleton was designed based on the kinematic model of one specific subject (more details in Section 4.3). Then wrist orientation was observed during pointing tasks with the exoskeleton in the following conditions: i) optimal alignment between human and exoskeleton joints; ii) varying degrees of misalignment between human and exoskeleton joints; iii) optimal alignment while the PS axis was locked, i.e., no redundancy.

Finally, in the last section of this chapter, I show how kinematic discrepancy would lead to hyperstaticity, i.e., over-constrained mechanism, in a backdrivable robot. Then, I implement a practical solution to avoid hyperstaticity and reduce the level of reaction force/torque in the wrist. This technique is shown to reduce 75% of the force and 68% of the torque. I also shown how an over-constrained mechanism could alter human motor strategies. The presented solution as well as the other results of this chapter has been taken into account in the early phase of design of my robot, presented in detail in Chapter 6.

This study has been reflected in the following publications:

- M. Esmaeili, K. Gamage, E. Tan, and D. Campolo, *Ergonomic Considerations for Anthropomorphic Wrist Exoskeletons: A Simulation Study on the Effects of Joint Misalignment*, Intelligent Robots and Systems, IROS. IEEE/RSJ International Conference on, pages 4905–4910, September 2011.

- M. Esmaeili, W. Dailey, E. Burdet, and D. Campolo, *Ergonomic Design of a Wrist Exoskeleton and its Effects on Natural Motor Strategies During Redundant Tasks*, Robotics and Automation, ICRA 2013. IEEE International Conference on, May 2013.
- M. Esmaeili, S. Guy, W. D. Dailey, E. Burdet, and D. Campolo, *Subject-Specic Wrist Model Calibration and Application to Ergonomic Design of Exoskeletons*, IEEE Sensors journal, 13(9):3293-3301, 2013.
- M. Esmaeili, N. Jarrassé, W. Dailey, E. Burdet, and D. Campolo, *Hyperstaticity for Ergonomic Design of a Wrist Exoskeleton*, Rehabilitation Robotics, ICORR 2013. IEEE International Conference on, June 2013.
- M. Esmaeili, N. Jarrassé, W. Dailey, E. Burdet, and D. Campolo, *Ergonomic Design of a Wrist Robot: the Influence of Hyperstaticity on Reaction Forces and Motor Strategies*, International Journal of Intelligent Computing and Cybernetics, Special Issue on "Robotic Rehabilitation and Assistive Technologies", (submitted), 2014.

5.1 Influence of kinematic compatibility in a human-machine interaction on reaction forces: Numerical study

Exoskeletons can be divided into two main categories: anthropomorphic and non-anthropomorphic [86]. In this work I present ergonomic considerations, based on kinematic simulations, for anthropomorphic exoskeletons meant to act in concert with the human wrist.

Discomfort in wearing an exoskeleton is due to interaction forces between human and exoskeleton arising at those locations where the exoskeleton is attached to the human limb. Such forces result from ‘kinematic discrepancies’ [40], due for example to oversimplified models of human kinematics and/or misalignments between human and exoskeleton joints [83].

Most of the modern approaches propose the use of extra degrees of freedom (DoF) for compensating joint misalignments. Such extra DoFs are passive, while only the joints which correspond to the human ones are meant to be actuated. While introducing extra DoF clearly helps reducing or eliminating kinematic discrepancy (for example, a 6DoF structure can surely adapt to a human wrist, at least within a certain range), it should be noticed that, when the extra DoF are present but locked during normal operations, a *kinematic mismatch* might still arise, i.e. joint angles at corresponding exoskeleton and human joints no longer coincide. Although some recent studies focused on reaching-movements for robot-assisted rehabilitation for the wrist domain [11; 13; 14; 85; 95], the effect of kinematic mismatch on robot control strategies, especially in relation to neurorehabilitation, received relatively less attention. Most control strategies, in fact, assume that driving (imposing motion or torque) a robotic joint is equivalent to driving the corresponding human joint.

In this chapter, I do consider extra DoF only for the purpose of wearing the exoskeleton, e.g. different subjects might require different positioning of the handle, but I will consider that all the extra dof as locked during normal operation. Therefore, from a kinematic perspective, the wrist exoskeleton will comprise only 2–DoF mobility at joints which are, in principle, aligned with human ones.

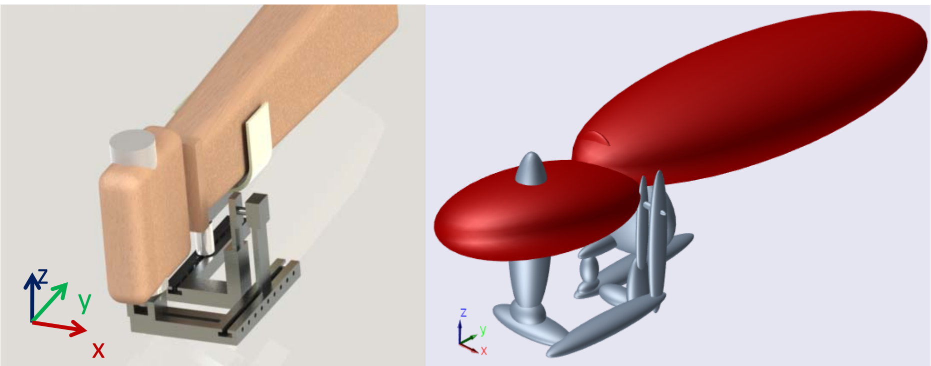

a) b)

Figure 5.1: Exoskeleton with hand model. a) Configuration of the exoskeleton alongside the wrist. b) SimMechanics model.

I shall consider a physiologically accurate 2–DoF model of the human wrist, which comprises an offset between the two human joints. Such an offset is known to vary from subject to subject, with a distribution experimentally derived by [53]. In this study, I assume that the misalignment between human and exoskeleton occurs at the both proximal and distal joints along the offset between them.

The human hand and the exoskeleton handle represent the endpoints[1] of two–DoF structures, for any non-zero misalignment, the position and orientation of the hand would be obviously incompatible with the position/orientation of the handle. In reality, the hand is not a perfectly rigid body, due, for example, to the skin compliance and to the possible adjustment in the grasping. For this reason I hypothesize that contact between hand and handle is non-rigid and occurs through some springs. In this study I assume linear springs and this is clearly a simplification, nevertheless interesting features such as asymmetry in the reaction forces can be captured, as discussed next.

---

[1] The other endpoint is where the exoskeleton is attached to the forearm, I assume this attachment much more rigid than the hand-handle one, see for example [67].

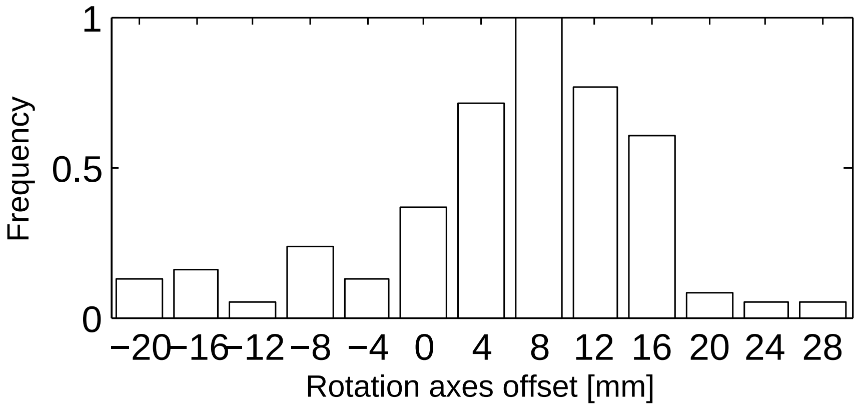

Figure 5.2: Normalized frequency distribution of wrist joint rotation axes offset, based on [53].

5.1.1 Modeling human-exoskeleton interaction in presence of kinematic mismatch

Modeling the human wrist

The human wrist is a complex joint with two degrees of freedom (DoF) responsible for radial-ulnar deviation (RUD, distal) and flexion-extension (FE, proximal). Despite small changes in the instantaneous center of rotation for each joint during rotations, a widely accepted approximation is to assume ideal revolute joints for both degrees of freedom. The simplest models assume a universal joint [104]. In reality, the FE and RUD axes are almost orthogonal and non-intersecting [2] and the joint offset of between the RUD and FE axes is known to vary among subjects. Leonard et al. [53] investigated, with noninvasive measurements, the distribution of the offset for a population of 108 subjects and reported a 6.8mm mean inter-axes offset with a distribution as shown[1] in Figure 5.2. Based on

---

[1] Note: the values were digitized from the original work [53].

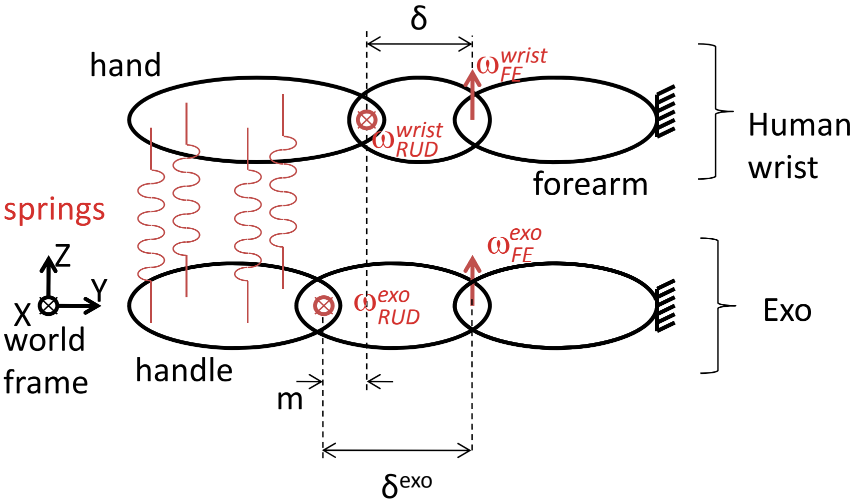

Figure 5.3: Functional diagram of the wrist and exoskeleton. Through a chain of links and joints human wrist is connected to the exoskeleton. Joint offset is considered for the both wrist (δ) and exoskeleton (δ^{exo}). Misalignment (m) is applied on the exoskeleton joints throughout the simulations.

the above considerations, I developed a kinematic model of the human wrist in the SimMechanics (MathWorks Inc.) environment. As shown schematically in Figure 5.3, the model consists of a series of three rigid bodies[1], the most proximal being the forearm (fixed) and the most distal being the hand, connected to one another via revolute joints. I considered two orthogonal joints $\boldsymbol{\omega}_{FE}^{wrist}$ (proximal) and $\boldsymbol{\omega}_{RUD}^{wrist}$ (distal) and with an offset between the two axes ('joint offset') along the longitudinal axis of the forearm (Y-axis).

Each joint has an associated joint angle: θ_{FE} and θ_{RUD} for the FE and RUD axes, respectively. For the joint angles, I assumed an average range of motion presented in Table 3.1.

---

[1] The middle body is simply used to introduce an offset between the two joints.

Modeling of the exoskeleton

For the exoskeleton, I considered an anthropomorphic structure, i.e. a 2–DoF mechanism with revolute joint axes $\boldsymbol{\omega}_{RUD}^{exo}$ and $\boldsymbol{\omega}_{FE}^{exo}$ with a similar proximal-distal order and aligned with the anatomical counterparts. As for the alignment, as I shall see next, a variable misalignment will be purposely introduced to analyze its effects.

The proximal end of the exoskeleton is meant to be attached to the forearm, and therefore fixed. The distal end of the exoskeleton is attached to the hand through the handle. While for the forearm I can resort to optimal attachments methods which minimize skin motion effects, e.g. see the splinting proposed in [73], the hand-handle attachment is more prone to relative motions and, to the authors' knowledge, much less analyzed in literature. For this reason, I assumed a perfect attachment between the human forearm and the proximal side of the exoskeleton while I assumed a non-rigid attachment between human hand and handle. This non-rigid attachment is implemented via a set of four non-collinear ideal springs which are meant to allow some degrees of relative motion between human hand and handle during grasping. This is a preliminary numerical study and requires further experimental validation. Nevertheless, I refer to similar approaches performed by Schiele et al. on [81] although not specifically for the hand-handle attachment. The stiffness constant to the four springs are heuristically set equal to 2000 N/m, that is also similar to the stiffness values used in haptic channel experiments [78]. The use of four non-collinear springs results in a translational and rotational stiffness throughout the movements which are considered in potential energy (see 5.1.3).

Besides the FE and RUD joints which are supposed to mirror the human

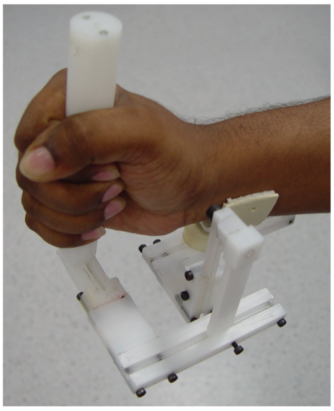

Figure 5.4: Prototype of the exoskeleton. Besides, the FE and RUD joints of the exoskeleton which are supposed to mirror the human counterparts, the extra passive joints are considered to align the exoskeleton with different size of end users.

counterparts, the exoskeleton is also endowed with a number of ‘passive’ joints. Such passive joints are required to adapt the exoskeleton itself to the different size of end users.

Remark: the passive joints are meant to be locked while the exoskeleton is in use. The model used in my simulations, described next, takes into account the full structure of the exoskeleton. This is important for future studies, when the inertial properties of the exoskeleton will also be considered.

5.1.2 Simulation and data analysis

Although in this study I am interested in the ergonomics of the exoskeleton from a kinematic perspective, in my simulations I implemented the full structure of the exoskeleton as shown in Figure 5.4, comprising the inertial properties of each element. Given the elastic and the inertial properties present in the model, transient behaviors would inevitably arise after each step of the inputs. For this reason, I also added linear dampers in series to each spring, to dampen out any mechanical resonance due to the elastic properties of the springs and the inertial properties of the exoskeleton. Heuristically, I set the linear damping coefficients to 1.0 $N/(m\,s^{-1})$ as this generated overdamped behaviors, quickly leading to steady-state conditions.

In order to analyze the steady-state conditions for different human wrist postures, FE and RUD joints in the human wrist model are actuated according to a sequence of discrete values corresponding to a 11 × 9 matrix of values covering a range of movement of $[-50^o\ \ 50^o]$ by 10 degrees step for FE and $[-20^o\ \ 20^o]$ by 5 degrees steps for RUD.

SimMechanics is a continuous time simulator, so discontinuous, step-like transitions between two discrete values of a joint angle would elicit long-lasting transient behaviors, while I am only interested in steady-state conditions. In order to generate smooth transitions between discrete values of each joint angle, I used the `jtraj` function, distributed with the MATLAB *Robotics Toolbox* [16]. This function receives the two consecutive joint angles (e.g. q_{start} and q_{end}) and implements a 5th order polynomial interpolation to generate the required joint velocity and acceleration for producing the smooth transition for the provided joint trajectory.

As seen from Figure 5.5, the combined effect of smooth transitions between discrete values of the human joint angle and the over-damped response of the system ensures short transient behaviors. The steady-state conditions of the angles for both human and exoskeleton joints can be reliably sampled at fixed time intervals (circles in Figure 5.5).

By sampling at these very fixed time intervals, I was able to extract the steady-state values for the following variables (for both the human wrist and the exoskeleton):

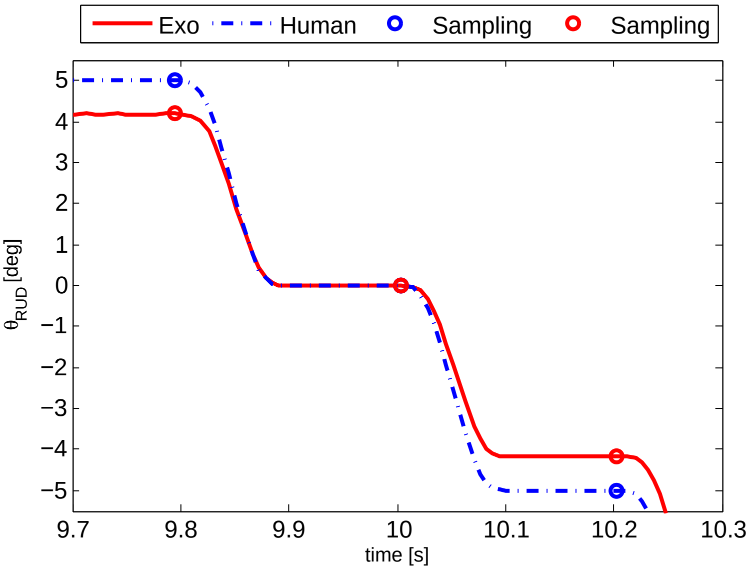

Figure 5.5: Steady-state sampling represented in time domain. Blue dash-line is the active movement of wrist followed by exoskeleton (red solid line) passively. Circles are the samples chosen when system is in steady-state condition.

- *kinematics*: the angular position, angular velocity and angular accelerations for FE and RUD joints;
- *reaction forces* ($\boldsymbol{F}_r$): amplitude[1] of generated forces due to misalignments for FE and RUD joints, computed as

$$F_r = \sqrt{F_x^2 + F_y^2 + F_z^2}$$

- *discomfort function*: for each misalignment, I compute the mean value over the workspace of the elastic energy of the springs between hand and handle[2] (see Figure 5.3);

---

[1] Single force components could be analyzed as well, but no qualitative difference was found.

[2] Although rather arbitrary, I noticed no qualitative difference when choosing the mean value of reaction forces or kinematic mismatch between human and exoskeleton joint angles.

Therefore, for each posture of the human wrist, (i.e. a 9×11 matrix of values covering Table 3.1, I extracted the corresponding values for the physical variables described above.

I repeated the simulation for different possible misalignments between the RUD/FE joint of the exoskeleton and the RUD/FE joint of the human wrist. In particular, based on the work of Leonard et al. [53] in Figure 5.2, a misalignment distribution[1] was considered. The choice of range of misalignments was dictated by the aggregate loss calculations explained later. Note that just for programming convenience, the human joint offset was held constant while the misalignment was generated by varying the exoskeleton joint offset.

5.1.3 Results

Kinematic mismatch

A so-called active mode operation, i.e., desired angles were imposed for the human joints while the exoskeleton passively followed, is simulated. As expected, except for the case of perfect alignment, there was a kinematic mismatch between the exoskeleton FE/RUD angles and human counterpart (since the joint misalignment was for the FE (proximal) joint, the angular mismatch was obviously found between the human and exoskeleton FE and RUD angles too). Figure 5.6 shows a representative case, for a $+12mm$ joint misalignment. The mismatch grew approximately linearly with the angle. For the representative case of $+12mm$ misalignment, there is a 20% relative error, as shown in Figure 5.6.

---

[1] These misalignments are along the longitudinal axis of the forearm, i.e. in the Y-axis as in Figure 5.3.

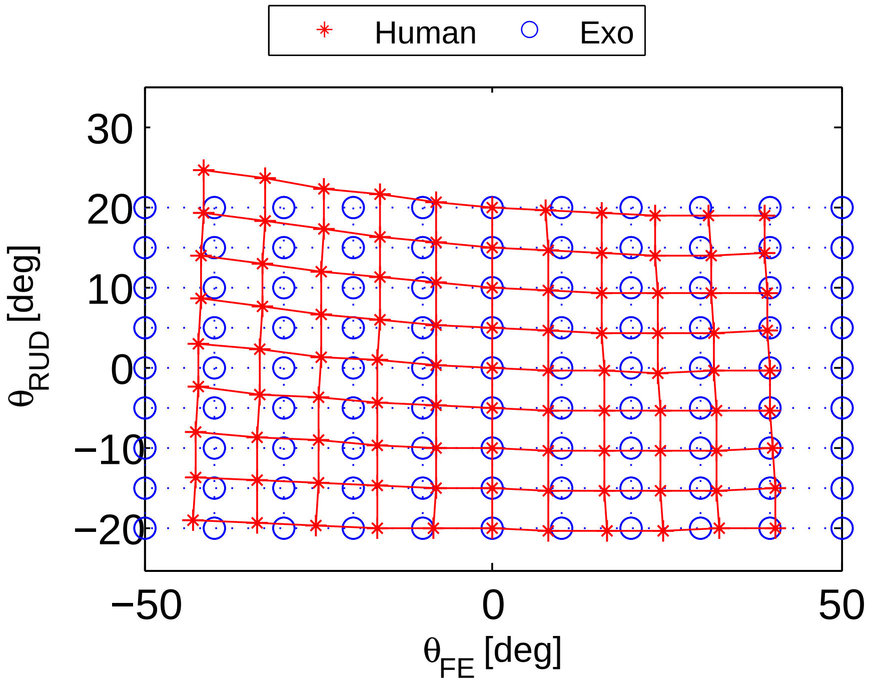

Figure 5.6: Range of motion of exoskeleton (solid line-crosses) is compared with wrist (dots-circles) for a representative $+12mm$ misalignment on ω^{exo}_{FE}.

Reaction forces at human wrist

Figure 5.7.a shows the reaction forces at the FE joint of the human wrist (Fr^{wrist}_{FE}) against the range of motion of FE and RUD joints. These forces are monitored in the presence of $+12mm$ misalignment between the ω_{FE} of wrist and exoskeleton. In covering the whole RoM_{FE}, the maximum amounts of reaction forces occur in the maximum range of the wrist flexor for the whole RUD joint angles. No reaction force is seen throughout the RoM_{RUD} when $\theta_{FE} = 0$. For each FE joint angle the amount of Fr_{FE} is almost constant across RoM_{RUD}.

Note: Since stiffness of the springs in the attachment points as well as damping ratio are heuristically selected, I took into account the normalized values for all forces.

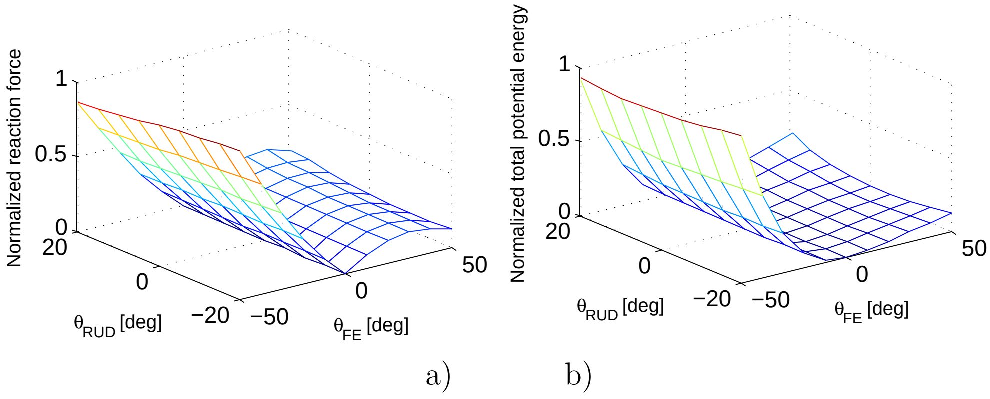

Figure 5.7: Normalized reaction force on FE joint of wrist over the range of motion of FE and RUD (a), and normalized deformation energy at attachment points of end-effector (b) for $+12mm$ misalignment on ω_{FE}^{exo}.

Non-rigid attachment

The resulting deformation energy of the four non-collinear springs, explained in 5.1.1, during movement of the wrist could be calculated through

$$\boldsymbol{U}_t = \sum_{i=1}^{4} \frac{1}{2} k_i \, \boldsymbol{l}_i^2 \tag{5.1}$$

Where, k is the stiffness and $\boldsymbol{l}$ is the length of each spring shown in Figure 5.3. Figure 5.7.b, illustrates the resulting deformation energy over wrist RUD and FE angles. It can be seen that, deformation energy significantly changes across flexion-extension rotations while it seems less sensitive to radial-ulnar deviations.

Moreover, I calculated the mean values of the deformation energy for each amount of misalignment and considered the normalized amount of this deformation energy during movement of wrist as the *Normalized discomfort* which is shown in Figure 5.8.a.

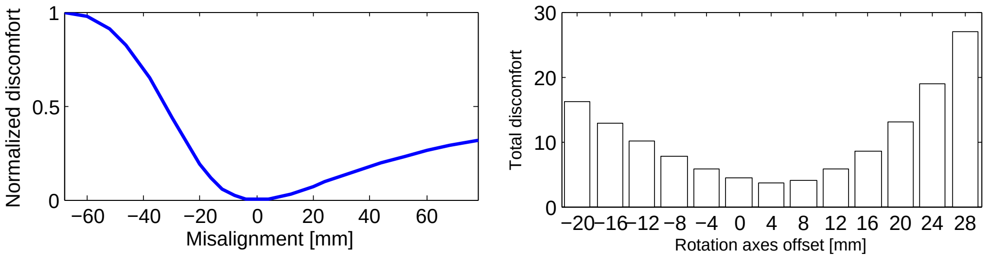

a) b)

Figure 5.8: Normalized discomfort over the different amount of misalignments (a), and density of total discomfort over the range of wrist axes offset (b). The mean of total potential energy for a set of misalignment is taken into consideration in calculating total discomfort.

One-size-fits-all

Since the RUD–FE offset for the exoskeleton cannot be, in principle, aligned by simple visual procedures, in this section I try to estimate which optimal offset, for the exoskeleton, would best fit an entire population, not just a single subject. For this I shall use the distribution of the joint offsets derived by Leonard et al. [53] and correlate it with the discomfort caused by different misalignments, as in Figure 5.8.a.

To this end I shall make use of the concept of ‘aggregate loss’ [36] which is widely used in the fields of Human Factors and Ergonomics as well as in Economics. Simply put: if one has to design a one-size T-shirt meant to fit an entire population, knowing the anthropomorphic data of a population and knowing that each individual will claim a refund proportional to the amount of discomfort (a positive function of size mismatch), what is the optimal size that will minimize the total refund (aggregate loss)?

One might be tempted to design a T-shirt that fits the average size (from the population distribution) any asymmetry in the population distribution or in the discomfort function (e.g. better a T-shirt too large rather than too small) might induce better choices.

In the case of my study, the probability density function (PDF) of joint offsets (δ), i.e. $PDF(\delta)$, for the population sampled by Leonard et al. [53], reported in Figure 5.2, does not present remarkable asymmetries, with the average offset being $\bar{\delta} = 6.8mm$. On the other hand, the discomfort $\bar{U}(m)$, function of misalignment (m), is highly asymmetric due to mounting the exoskeleton in the interior side of the wrist, as shown in Figure 5.8.a. An exoskeleton with offset δ^{exo} worn by a person whose anatomical offset is δ, would cause a discomfort $\bar{U}(\delta^{exo} - \delta)$. Therefore, the aggregate loss $\mathcal{L}(\delta^{exo})$, for a specific choice of exoskeleton offset, is

$$\mathcal{L}(\delta^{exo}) := \int PDF(\delta)\bar{U}(\delta^{exo} - \delta)\, d\delta$$

Figure 5.8.b shows the aggregate loss numerically estimated from the data available from Leonard et al. [53] and the simulated discomfort function.

The optimal offset for the exoskeleton is numerically found to be

$$\delta^{exo}_{opt} := \arg\min \mathcal{L}(\delta^{exo}) = 4\ mm$$

The other important issue might arise due to misalignment, is its possible effect on human motor coordination mechanisms during a redundant task which is addressed in the next section.

5.2 Influence of kinematic compatibility in Human-Robot Interaction on motor strategies: Experimental Study

Human-robot interaction, a central topic in the field of robotic exoskeletons, necessitates consideration of ergonomy, and ergonomic constraints have recently become prevalent in the early stages of exoskeleton design methodologies [81], [24]. This section presents an ergonomic anthropomorphic exoskeleton based on kinematic simulations discussed in Section 5.1. The exoskeleton is intended for interaction with the human wrist while achieving maximum comfort. Discomfort associated with exoskeleton use arises from interaction forces at the points of contact between the exoskeleton and the human limb. These "kinematic discrepancies" [38] can result from oversimplified models of human kinetics and/or misalignments between the human and exoskeleton joints.

As a consequence of reaction forces arising at the human joints due to misalignment with the exoskeleton axes, natural motor strategies are likely to be affected. It was shown that excessive perceived mechanical impedance would alter motor strategies adopted by the brain during redundant tasks performed with a robot [11], despite the backdriveability of the robot itself.

It is proposed that "soft" constraints, i.e. those of a neural origin, should be considered alongside the more traditional "hard" (biomechanical) constraints. Building on the works [11; 93], this chapter presents a preliminary study on motor strategy adaptation. These adaptations arise during kinematically redundant motor tasks while the subject wears exoskeletons of varying ergonomic levels.

To this end, an ergonomic exoskeleton is first designed and developed to match the anthropometric features of one specific subject based on in-vivo ambulatory assessment methods [26; 68].

Kinematic redundancy in the human motor system is common as in many tasks there are more Degrees of Freedom (DoF) than necessary to complete the task. If the mechanics does not constrain the movement, the sensorimotor system addresses this redundancy by imposing soft constraints and applying strategies for improved motor efficiency. These neural constraints are commonly referred to as intrinsic constraints [54]. The earliest observations of intrinsic constraints came from the oculomotor system. In 1847, Donders observed that physiological eye configurations can be described by a 2-dimensional surface embedded in the 3-dimension space of eye configurations for a given steady gaze direction. Though it was initially unclear if Donders law resulted from biomechanical or neural mechanisms, it is now understood that neural mechanisms are responsible for the law as it applies to head and limb movements [27]. Recent studies have demonstrated that Donders law can be applied to two–DoF pointing tasks of the wrist. In such tasks, the 3 DoFs of the wrist become redundant [12; 13; 14].

5.2.1 Experiments to evaluate kinematic compatibility

Setup

To obtain the data required for my analysis, experiments similar to Section 3.2 are conducted, using the setup shown in Figure 5.9.a. To ensure pure movement of the wrist and minimum movement of the elbow, the shoulder and torso during the experiment, the subject was asked to be seated on a chair with his forearm

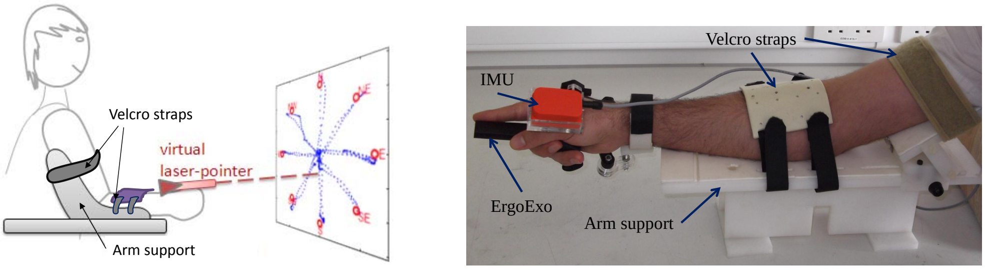

a) b)

Figure 5.9: Experimental setup for trials with ErgoExo. a) schematic view of the chair and subjects posture with respect to the screen, b) ErgoExo grasped by the subject.

was strapped to the arm-support, as shown in Figure 5.9.b. The orientation of the wrist, R, was captured by means of a motion tracking sensor (MTx-28A-33-G25 device from XSens Inc.). The static orientation accuracy and bandwidth of the sensor are $< 1^o$ and $40Hz$, respectively. At $120Hz$, the sequence of orientation matrices, R_i (representing the i-th sample) was downloaded onto a PC for offline data analysis. During the movements, real-time visual feedback was provided for the subject. A zeroing procedure was performed before the start of each trial to define the wrist's anatomical neutral position. For details see [13].

Protocol

The subject, who declared to be right-handed, was asked to perform the 'center-out' pointing task depicted in Figure 5.10. Similar to the task presented in Section 3.2, the subject was asked to point from the central target toward one of eight peripheral targets. The subject was asked to perform 20 trials in each experiment of which five were training trials designed to familiarize the subject with the task. These training trials were excluded from the analysis, the 15 remaining trials were taken into account for further analyses.

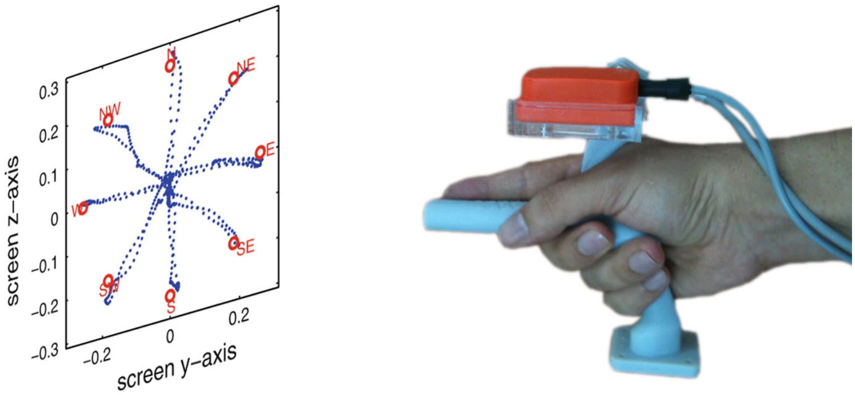

Figure 5.10: ‘Center-out’ pointing task. Starting from central target, the peripheral targets was turning on (the color was changed to red) by the software on a random sequence. The subject was instructed to point at the active (red) target.

The subject was instructed to perform the *center-out* experiment in three different conditions: *i*) grasping ComfGrip as shown in Figure 4.4, *ii*) wearing ErgoExo illustrated in Figure 4.12.b and *iii*) wearing non-ergonomic exoskeleton. To make the exoskeleton non-ergonomic, three pads of thicknesses 4, 8 and 12 *mm* were prototyped and mounted on the ErgoExo. These pads cause an increase of distance between the palm and the back side of the handle resulting in misalignment on the RUD. This misalignment would make the exoskeleton uncomfortable [24].

Conditions *ii* and *iii* were conducted underneath two scenarios:

- Prono-Supination joint of exoskeleton (PSexo) was attached to subject’s forearm through the support cuff.
- PSexo was grounded.

5.2.2 Analysis of changes in motor synergies in presence of mechanical constraints

A sequence of rotation matrices, R_i, constitutes each trial of the center-out experiment (noting that 'i' is sample number with 120 samples per second). According to the sequence R_i relative to each trial, the sequence of rotation vectors, r_i, were calculated as eq. (3.8). Similar to Section 3.3, a generic quadratic surface, $\boldsymbol{r^*}_i = [r^*_{xi}\ r_{yi}\ r_{zi}]^T$, was fitted to the sequence of the first components r_{xi}, as depicted in eq. (3.9). This surface is called *Donders' surface*. I used nonlinear least squares fitting methods[1] to determine coefficients $C_1 ... C_6$. The first three coefficients, $C_1 ... C_3$, and the remaining three coefficients, $C_4 ... C_6$, respectively, define the linear feature and the curvature of the the surface. Similar to previous studies, I calculated the *thickness* of Donders' surface as the standard deviation of the residuals $r_{xi} - r^*_{xi}$. To analyze the 'shape' of Donders' surfaces, calculating the *mean*[2] and *Gauss* curvatures [20] through eq. (3.11) and eq. (3.12), respectively, I computed Koenderink's Shape Index as in eq. (3.13). By definition $-1 \leq S \leq 1$. Independently of curvature's amount, this index reflects the intuitive notion of shape [14].

2D gimbal case

To solve a 2D task such as pointing, only two degrees of freedom are strictly required and, in that case, there would no longer be kinematic redundancy. For the human wrist, the PS axis is the most proximal, while the RUD is most distal, leading to the forward kinematics presented in the equation (3.3). In the event of locked PS (e.g. $\theta^{PS} = 0$), the wrist acts like a 2D gimbal and, by definition, can only assume configurations which lie in a 2D surface:

---

[1] via `nlinfit` function in the Matlab environment from MathWorks, Inc.

[2] the mean of largest and smallest section curvatures

$$R_{locked} = \begin{bmatrix} c_{FE} \cdot c_{RUD} & -s_{FE} & c_{FE} \cdot s_{RUD} \\ s_{FE} \cdot c_{RUD} & c_{FE} & s_{RUD} \cdot s_{FE} \\ -s_{RUD} & 0 & c_{RUD} \end{bmatrix}$$

where $c_{FE} = \cos\theta^{FE}$, $c_{RUD} = \cos\theta^{RUD}$, $s_{FE} = \sin\theta^{FE}$, $s_{RUD} = \sin\theta^{RUD}$. Straightforward calculations can show that, for the relative rotation vector $[r_x\, r_y\, r_z]^T = \log_\vee(R_{locked})$, the second order Taylor expansion at the origin ($\theta^{FE} = \theta^{RUD} = 0$) of the first component (r_x) with respect to the remaining ones (r_y and r_z) is simply

$$r_x = -\frac{1}{2} r_y \cdot r_z$$

corresponding to the quadratic function $C_1 = 0$, $C_2 = 0$, $C_3 = 0$, $C_4 = 0$, $C_5 = -\frac{1}{4}$, and $C_6 = 0$. For such a quadratic function, the corresponding curvatures and shape index are:

$$H_{locked} = 0\, rad^{-1}; \quad K_{locked} = -\frac{1}{4} rad^{-2}; \quad S_{locked} = 0. \tag{5.2}$$

In a numerical study, I set $\theta^{PS} = 0$ and generated a grid of angles for θ^{RUD} and θ^{FE} within the biomechanical range of wrist movement (representing the wrist sweeping across its workspace). The forward kinematic equation demonstrated in eq. (3.3) was used to generate the corresponding rotation vector for each point. eq. (3.9) was used to fit each surface and generate the synthetic Donders' surface depicted in Figure 5.11. The resulting coefficients $C_1 ... C_6$ were similar to above.

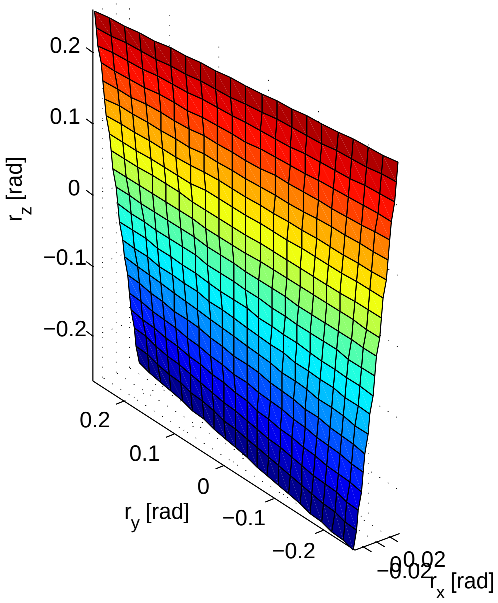

Figure 5.11: Synthetic surfaces for the pointing task when PS is locked.

Additionally, I calculated the values of H, K and S using eq. (3.11)-(3.13) and received the same values as the analytical values reported in 5.2.

The generic quadratic surface described by eq. (3.9) was fit to the data of each individual trial. The Gauss curvature K as a function of the mean curvature H for all trials is presented in Figure 5.13.a. Inspection of the plot demonstrates variation in the curvature between experiments. Based on the work presented in [14], the loci in Figure 5.13.a suggest shape clustering. The large black star represents theoretical 'locked PS' condition (H=0, K=$-\frac{1}{4}$). In the case of this chapter, the observed clustering is specific to each experiment. Figure 5.13.a demonstrates that the circular shape of the curvatures for a representative misalignment of 8 *mm* is significantly different from pointing by either ComfGrip or ErgoExo. These cases which are denoted by crosses and pluses, respectively, in Figure 5.13.a. Moreover, Figure 5.13.a shows the cluster of 'locked PS' exper-

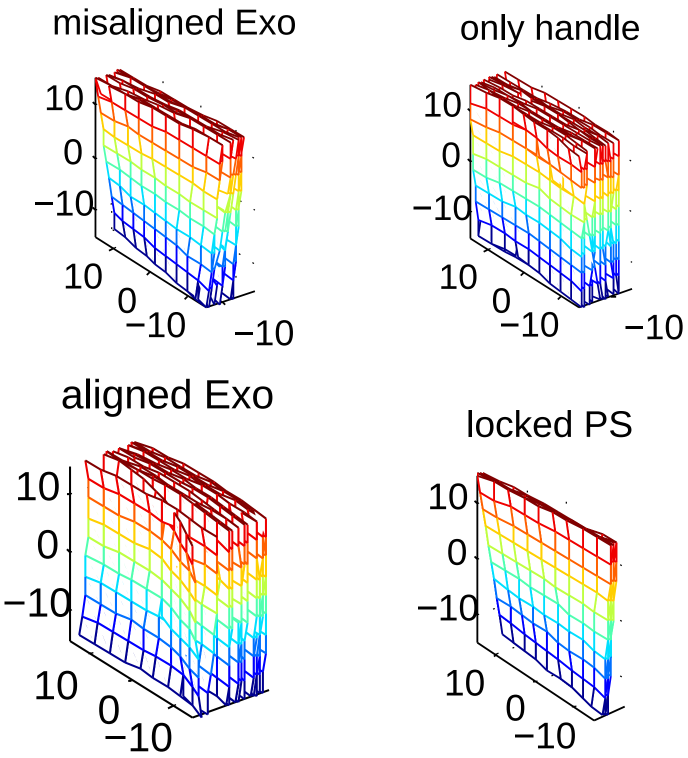

Figure 5.12: Donders' surfaces of all trials for each experiment.

iments, represented by black stars, are located in proximity to the large black star which is consistent with 2D gimbal discussed in Section 5.2.2. More specifically, Fig 5.13.b illustrates distributions of shape index for each experiment. The vertical line in this figure represents the theoretical case of locked PS (S=0).

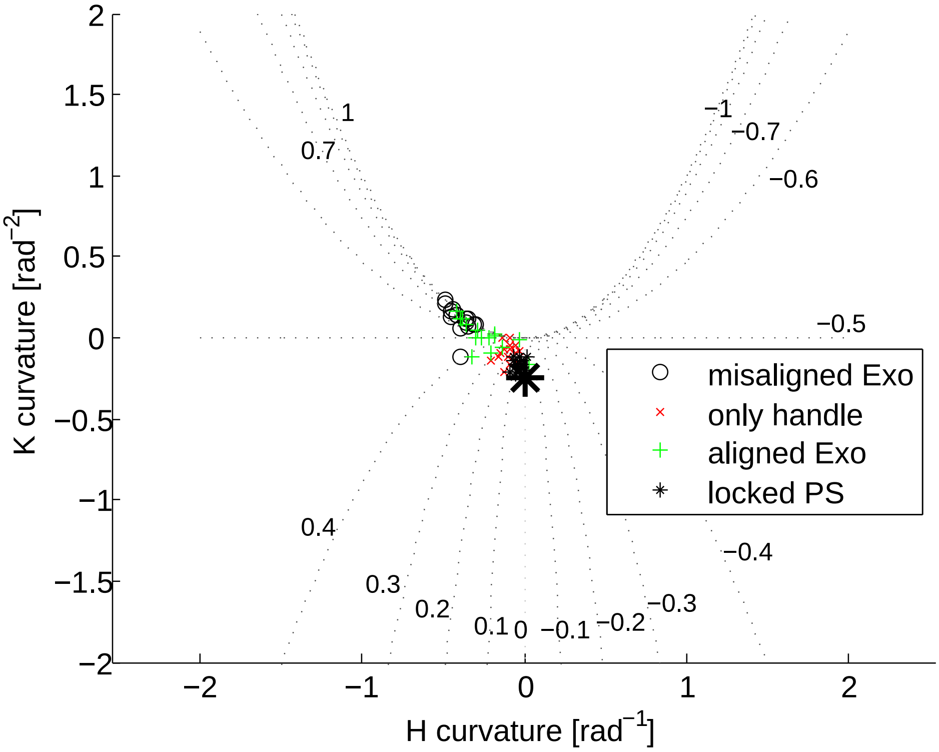

a)

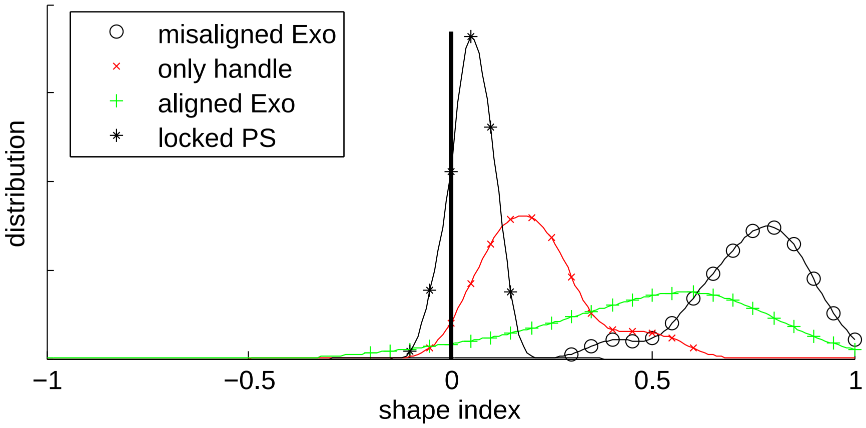

b)

Figure 5.13: a) Mean curvature (H) vs. Gaussian curvature (K) for all trials and all experiments. The different experiments are indicated with specific markers as indicated in the legend. Dotted lines indicate *loci* of (H, K) pairs with same Shape Index. The large black star represents the theoretical 'locked PS' condition (H=0, K=$-\frac{1}{4}$). b) Distribution of shape index for all experiments. The vertical line is the theoretical 'locked PS' condition (S=0).

5.3 Hyperstaticity and kinematic compatibility

Rehabilitation robotics experienced a strong and sustained growth of applications during the past four decades. These systems have evolved from the four degrees of freedom powered orthosis developed by CASE Institute of Technology in the early 1960's, which is generally recognised as the first rehabilitative manipulator [34], to recent state-of-the-art robots such as Bi-Manu Track [98]. In recent studies focusing on *neurorehabilitation*, most researchers targeted special therapy to recover the sensorimotor function and improve movement coordination in patients with lesions of the central or peripheral nervous system, e.g. after stroke [47; 60; 70; 74]. In order to provide efficient training enabling patients to reacquire motor capabilities, it is crucial that rehabilitation robots should neither alter natural movements of the patients nor suppress any motor capability [35]. Therefore, special attention should be paid to robot workspace, fixation points, and control strategies to avoid any extra (unnatural) force or movement during therapy. On the other hand, haptic interfaces used to investigate the sensorimotor function in humans should avoid any resistance or reduction of the degrees-of-freedom that can bias the results [14].

Recently, haptic interfaces, exoskeletons and robots have been developed to promote self-rehabilitation [89], arm and wrist rehabilitation [56; 65]. The pronosupination (PS) joint of the forearm has received considerable attention in these devices. This joint is complex and cannot be effectively modeled as a simple pivot joint[1]. This issue was not taken into account during the design of most of these devices and it was assumed that alignment between a robot pivot joint and the virtual PS axis results in a kinematic match between the joints. Even when the device and forearm joint are perfectly aligned in the rest position, the unique configuration of the PS joint causes a misalignment as soon as movement is initiated. Thus, closing the (human+robot) mechanical loop with a "different" and simplified robotic joint leads to over-constrained configuration, i.e. hyperstaticity. As a consequence, uncontrolled interaction forces would arise as soon as misalignment occurs.

---

[1] The movement of this joint is produced through the rotation of radius bone about the ulna while the ulna is nearly steady. Therefore, the PS rotation axis changes during the movement.

In this section, I present the importance of accounting for over-constrained attachments when designing a robot for human motor studies, haptics applications or rehabilitation. I examine how the fixation of the human to the device necessitates attention when analyzing kinematic compatibility as presented in [39] and my previous work [25]. I first applied the method from [39] and performed simple experiments to evaluate the amount of uncontrolled and undesired force that can be applied on the human wrist by a over-constrained robot. I assessed the level of overall force and torque due to hyperstaticity. I then present a practical solution to reduce the uncontrolled force/torque. This simple approach may be applied to commercial robots for reducing the level of undesired force/torque and during operation and in the design of highly backdrivable devices.

Moreover, I investigated the effect of hyperstaticity on human motor strategies. Through the "centre-out" experiment I evaluated soft constraints for free movements holding a handle and compared the results with the experiments with my wrist robot in the presence and absence of the proposed solution. I show how hyperstaticity might alter the user's motor strategies. Throughout this section, I refer to joint and reaction forces and torques as controlled and uncontrolled forces and torques, respectively.

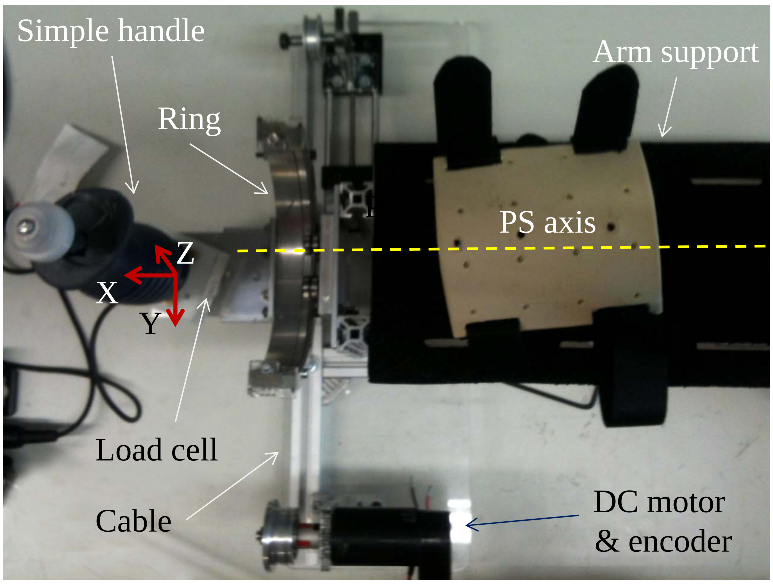

Figure 5.14: The initial wrist robot to study the reaction forces during prono-supination rotation.

5.3.1 Experimental setup for hyperstaticity

The Wrist Robot shown in Figure 5.14 is a one active DoF device used to collect the data required to validate the design of wrist interfaces. Its kinematics is composed of one pivot whose axis is intended to be coincident with that of prono-supination.

Control (for gravity compensation) and data recording are implemented in `MATLAB R2011b` (The MathWorks, Inc.), in a timed-loop structure with a high priority control loop at 1 kHz. This control frequency is sufficient because the bandwidth of human movements is limited to 2-3 Hz and only slow movements are performed with the device. Data (force and position) from the 6-DOF force sensor (Mini40-E Transducer from ATI Industrial Automation, Inc.) and encoder (HEDL 5540 optical encoder, 3 channels, 500 lines per revolution, from Avago Technologies.) is sampled at the same frequency and is transferred to the main program, through a data acquisition card (PCI-6221, National Instruments), and used for gravity compensation. A DC motor (3242G012CR, stall torque: 181 *mNm*, from Faulhaber GmbH & Co.) was coupled to the ring via cables (reduction ratio: 3.9) to transmit the required driving torque. I used LSC 30/2 motor controller (from Maxon motor AG) to drive the DC motor. More information about the robot is presented in Chapter 6, in detail.

5.3.2 Hyperstaticity in the coupling

Exoskeletons are usually designed to replicate the kinematics of human limbs. However, it is impossible to precisely follow human kinematics with a robot. Human joint kinematics are very complex and do not correspond to conventional robot joints. Moreover, morphology drastically varies between subjects. Discrepancy, and thus kinematic incompatibility between the two structures seem unavoidable. If the connected bodies were rigid, the resulting hyperstaticity would lead to uncontrollable internal forces and immobilization.

In practice, rigidity is not infinite and mobility can be achieved thanks to the compliance of human tissues. A common principle to reduce hyperstaticity is to add passive DoFs at the fixation points between the robot and human. I used the constructive technique, introduced in [39], to analyze the human-robot coupling, select the appropriate DoF to alleviate fixation, and design a mechanism guaranteeing global isostaticity and, consequently, a reduction in uncontrolled forces.

Application

The schematic view of the wrist robot is depicted in the Figure 5.15. Similar to

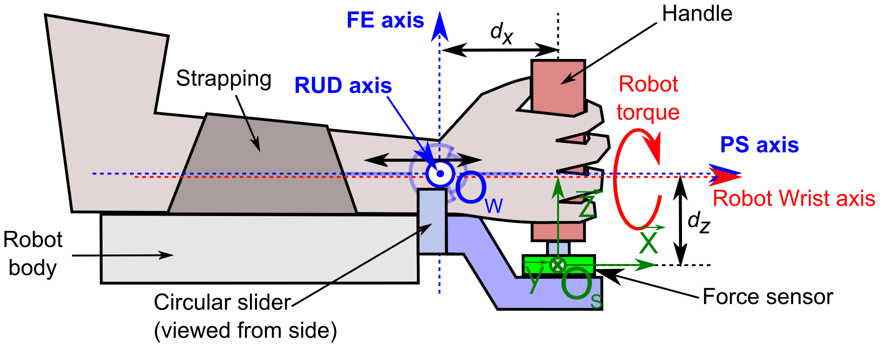
FE axis
d_x
Handle
Strapping
RUD axis
Robot torque
PS axis
Robot Wrist axis
O_W
Z
X
Y
O_S
d_z
Robot body
Circular slider (viewed from side)
Force sensor

Figure 5.15: The human forearm attached to the Wrist Robot. Visualization of the force/torque sensor frame at O_s, the three rotation axes of human wrist (PS: Prono/Supination, FE: Flexion/Extension, RUD: Radiar/Ulnar Deviation) intersecting at the wrist joint center O_w, and that of the robot.

my initial study [25], I applied the method from [39] to this device and its two fixations (the human forearm is attached to the main body of the robot whereas the human hand is “attached” to the handle mounted on robot’s end-effector), leading to the representation shown in Figure 5.16. Considering that the robot segments and the human limbs are connected together through n fixations and that each fixation is a mechanism consisting of a passive kinematic chain, the total

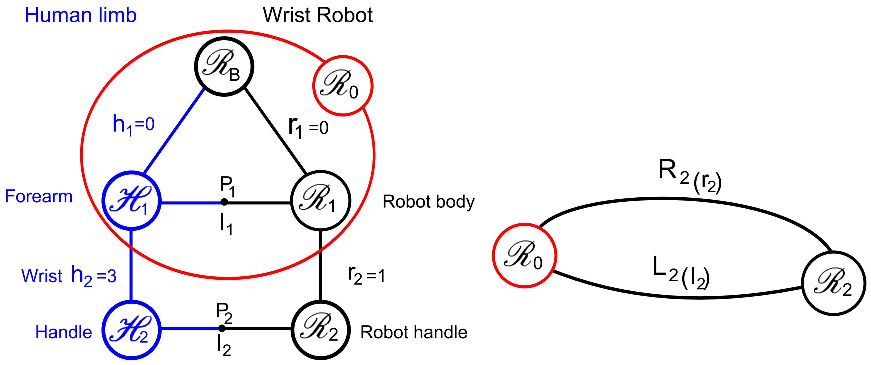
Human limb
Wrist Robot
$\mathscr{R}_B$
$\mathscr{R}_0$
h_1=0
r_1 =0
Forearm
$\mathscr{H}_1$
P_1
l_1
$\mathscr{R}_1$
Robot body
Wrist h_2 =3
r_2 =1
Handle
$\mathscr{H}_2$
P_2
l_2
$\mathscr{R}_2$
Robot handle
$R_2(r_2)$
$\mathscr{R}_0$
$L_2(l_2)$
$\mathscr{R}_2$

Figure 5.16: Schematic of the PS device and human forearm coupling.

number of passive DoF to be added is given by the following set of equations:

$$\forall i \in 1 \cdots n, \sum_{j=1}^{i} (l_j + r_j) \geq 6i \tag{5.3a}$$

$$\forall i \in 1 \cdots n, \ \sum_{j=1}^{i-1} (l_j + r_j) + r_i \leq 6i \tag{5.3b}$$

$$\sum_{j=1}^{n} (l_j + r_j) = 6n \tag{5.3c}$$

where l_i is the connectivity of the fixation mechanism i (fixation can be an embedment - $l_i = 0$ - or can release several DoFs, such that: $\forall i \in \{1, .., n\}, \ \ 0 \leq l_i \leq 5$), and r_i is the connectivity of each active robot joint. Considering that the human forearm is rigidly attached ($h_1 = 0$) to the robot body itself, which is fixed to the ground ($r_1 = 0$), the different bodies $\mathcal{R}_B$,$\mathcal{R}_1$ and $\mathcal{H}_1$ could be simply considered as a single rigid body $\mathcal{R}_0$. Thus, the goal is to define the number of DoF required to relieve the handle fixation level (i.e. l_2) and guarantee isostaticity (i.e. force controllability) even when the kinematics of the two chains (human and robot) differ.

Since only one fixation point is considered, only equation (5.3c) must be applied on the Wrist Robot structure demonstrated in Figure 5.16:

$$\sum_{j=2}^{n=2} l_j = 6 - r_1 = 1 \quad \Rightarrow l_2 = 5 \tag{5.4}$$

Selecting a solution

According to screw theory, the wrench describing the action of the robot r applied to the human limb h, at the wrist center O_w, expressed in the reference frame R_0 attached to the fixed body of the robotic interface, is:

$$\{\mathcal{W}_{O_w,\mathrm{r}\to\mathrm{h}}\} = F_{\mathrm{r}\to\mathrm{h}}\tau_{O_w,\mathrm{r}\to\mathrm{h}_{R_0}},\ \ F_{\mathrm{r}\to\mathrm{h}}, \tau_{O_w,\mathrm{r}\to\mathrm{h}} \in \mathbb{R}^3$$

where $F_{\mathrm{r}\to\mathrm{h}}$ are the forces applied on the human wrist by the robot, and $\tau_{O_w,\ \mathrm{r}\to\mathrm{h}}$ are the torques applied at the wrist joint center O_w (see Figure 5.15). Because force measurement is available at the sensor center O_s, it is possible to derive the expression of $\mathcal{W}_{O_w,\mathrm{r}\to\mathrm{w}}$ from $\mathcal{W}_{O_s,\mathrm{r}\to\mathrm{h}}$. Therefore, by treating the mechanism and the wrist as a single rigid body:

$$\tau_{O_w,\mathrm{r}\to\mathrm{h}} = \tau_{O_s,\mathrm{r}\to\mathrm{h}} + O_wO_s \wedge F_{\mathrm{r}\to\mathrm{h}}$$

and thus:

$$\{\mathcal{W}_{O_w,\mathrm{r}\to\mathrm{h}}\} = \left\{ \begin{matrix} F_x & \tau_x^{O_s} - d_zF_y \\ F_y & \tau_y^{O_s} + d_xF_z^s + d_zF_x \\ F_z & \tau_z^{O_s} - d_xF_y \end{matrix} \right\} \tag{5.5}$$

where $(F_x, F_y, F_z, \tau_x^{O_s}, \tau_y^{O_s}, \tau_z^{O_s})$ are the force and torque components measured at the force/torque sensor center O_s and $O_wO_s = [d_x\ d_y\ d_z]^T$. Using the wrench formulation, it is easily possible to find alternative design solutions to "unlock" some DoFs at the wrist joint center through the addition of passive DoF mechanisms at other positions in the human-robot mechanical loop.

Based on the previous formulation of $\mathcal{W}_{O_w,\mathrm{r}\to\mathrm{h}}$ and the recommendations

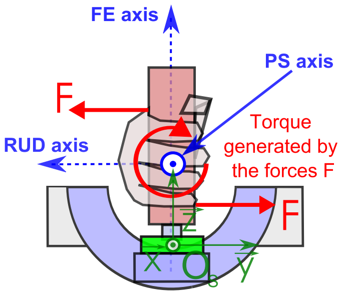

Figure 5.17: Generating torque around the PS axis through application of forces.

from [39] about how to select which Degrees of Freedom to release, three aspects are considered:

i) Velocities compatibility: I first examined the velocities of the relevant human limbs that are incompatible with the robot's kinematics. According to this analysis, all of the translational velocities along the PS, FE and RUD axis should be released, along with the two rotational velocities around the FE and RUD axes (see Figure 5.17 below for axes definition).

ii) Force transmission: the wrist-robot is dedicated to the interaction with human prono-supination, thus only rotation around the PS axis should fixed in order to control the torque around this axis. Considering the coordination system in Figure 5.15, the controlled torque would be $\tau_c = \parallel \tau_x \parallel$. The other generated forces and torques are uncontrolled and can be expressed as $F_{uc} = \sqrt{F_x^2 + F_y^2 + F_z^2}$ and $\tau_{uc} = \sqrt{\tau_y^2 + \tau_z^2}$.

iii) Consideration of human physiology: The moment around a main limb segment axis should not be transmitted directly (as this would deform the muscles), but rather be generated by the distant application of opposed forces. In this case, the solution was inherently included due to the handle as illustrated in Figure 5.17.

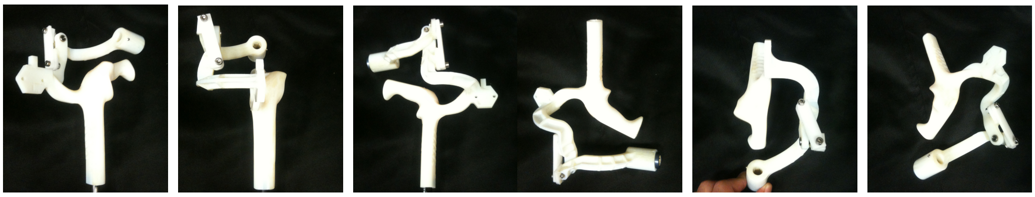

Figure 5.18: Different views of the Ergonomic exoskeleton (ErgoExo).

Finally, the following DoFs were released in the design (see the orange arrows on Figure 5.19): translation along the handle to prevent from force F_z application by the robot along the FE axis; translation along the forearm to prevent application of any force F_x along the PS axis; rotation around the FE axis to prevent the appearance of torque $\tau_z^{O_w}$ and the rotation around the RUD axis (to prevent from the projection of any torque $\tau_y^{O_w}$ generated by the robot or the human PS joint on the wrist flexion joint, and vice versa).

To simplify the design, this preliminary version of the robot does not incorporate translation release along the RUD axis at the handle, and thus does not avoid the appearance of F_y. Redesigned fixation mechanisms lead to following wrench (considering also that $O_wO_s = [0\ 0\ d_z]^T$):

$$\{\mathcal{W}_{O_w,\mathrm{r}\rightarrow\mathrm{h}}\} = \begin{Bmatrix} 0 & \tau_x^{O_s} - d_z F_y \\ 0 & 0 \\ 0 & 0 \end{Bmatrix} \tag{5.6}$$

The improved version of the robotic PS interface, adding the new handle, called *Ergoexo*, can be seen in Figure 5.18. I mounted the *ErgoExo* on my wrist robot to conduct experiments, as it is shown in Figure 5.19.

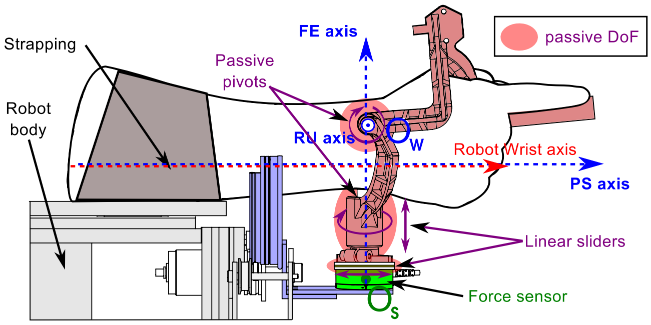
Strapping
Robot body
Passive pivots
FE axis
passive DoF
RU axis
W
Robot Wrist axis
PS axis
Linear sliders
Force sensor
S

Figure 5.19: Human forearm attached to the Wrist Robot. Visualization of the force/torque sensor frame, the three rotation axes of human wrist, and the robot. Passive DoFs are represented by orange arrows.

5.3.3 Experiments to evaluate hyperstaticity

Setup

Based on the presented solution the setup shown in Figure 5.14 was modified to the Wrist Robot presented in Figure 5.20 to validate the design. In order to study the effect of releasing passive DoF, mechanisms were added to block these passive DoF when needed. To ensure pure movement of wrist and minimal movement of elbow, shoulder, and torso during the experiment, the subject was

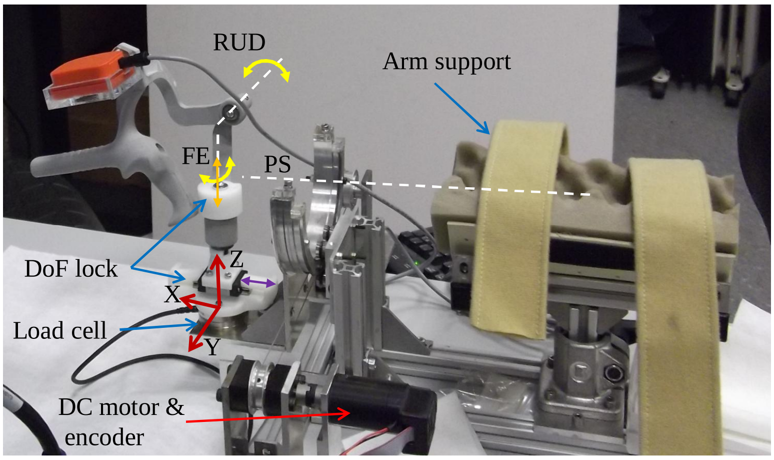
RUD
Arm support
FE
PS
DoF lock
Z
X
Load cell
Y
DC motor & encoder

Figure 5.20: Improved Wrist Robot to study the reaction forces during prono-supination rotation.

asked to remain seated on a chair with his forearm strapped to the arm-support as illustrated in Figure 5.14. The interaction force/torque was recorded with a (Mini40-E Transducer from ATI Industrial Automation, Inc.) load cell whose orientation and axes can be seen on Figure 5.19.

Protocol

Eight subjects (three female, age 22-27), who declared themselves to be right-handed, were asked to perform the following 'PS-rotation' movements. Using a mechanical linkage, the same starting pose for all subjects are initiated. The subjects were instructed to grasp the handle firmly throughout the experiment, pronate their wrist to the limit of his/her range of motion, followed by supination to the opposite limit, and finally pronate back to the starting point. I asked the subjects to rotate their wrists as far as they are comfortable without feeling pain. For each subject the force/torque was biased just before the first movement to cancel out the weight of the wrist. Experiment was conducted in three blocks with ten repetitions per block, under the following conditions:

1. the passive DoFs were locked and gravity was not compensated,

2. the passive DoFs were locked but gravity was compensated,

3. the passive DoFs were released and gravity was compensated.

Special attention is paid to align the prono-supination axis for each subject with the robot's center of rotation. To do so, each subject is instructed to be seated and place his/her forearm comfortably on the armrest. Then the forearm was strapped to armrest to minimize the elbow and torso possible movements. Each subject was instructed to perform ten rotations about prono-supination axis incorporat-

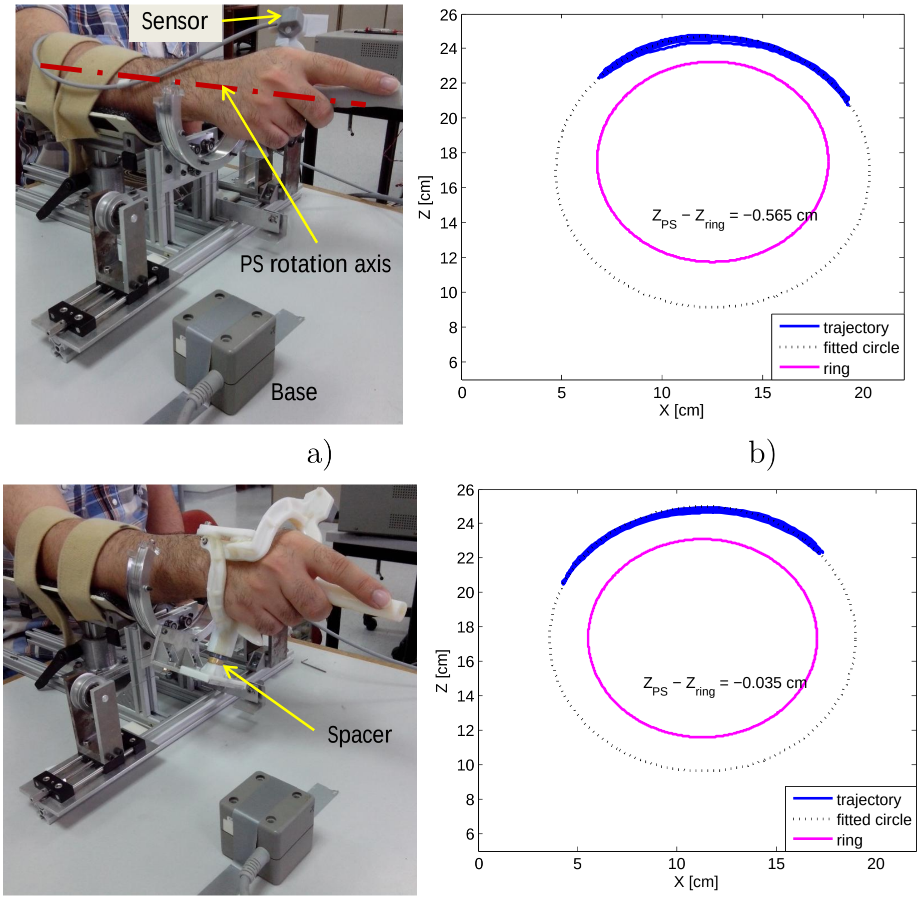

a) b)

c) d)

Figure 5.21: Aligning the prono-supination axis of the subject and the robot.

ing no flexion-extension neither abduction-adduction. I recorded the kinematics of the movements through the Polhemus sensor, as presented in Figure 5.21.a. From the recordings, I plotted the trajectory of the wrist rotations (blue lines in Figure 5.21.b), then I estimated the PS center of rotation of the subject (black dots in Figure 5.21.b) and ultimately found the amount of offset between subject and robot's PS rotation axis. Using a mechanical spacer, as in Figure 5.21.c, the offset was removed. Repeating the mentioned procedure, the results show almost concentric rotation centers for the wrist and the robot as could be observed from

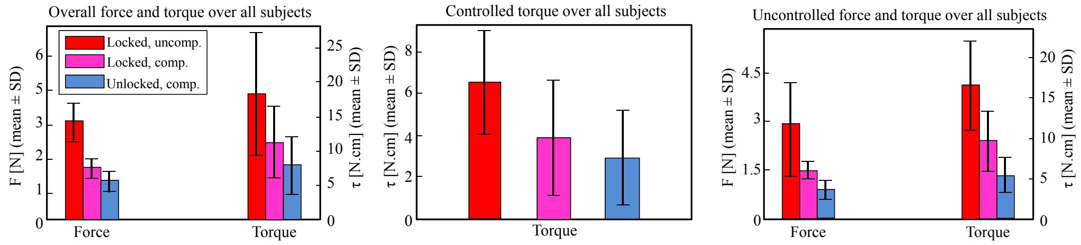

a) b) c)

Figure 5.22: The amount of (a) total, (b) controlled, and (c) uncontrolled force and torque over all subjects, all trials using the ErgoExo.

Figure 5.21.d, i.e. aligning the PS axis of the robot and the user.

5.3.4 Results

Influence of Hyperstaticity on reaction forces

The following forces and torques are expressed at the wrist center O_w (see Figure 5.19) as the main interest is in reducing the uncontrolled effort at (human) joint level. As previously described, the only controlled component is $\tau_c = \parallel \tau_x \parallel$ and the rest are undesired and uncontrolled force/torque, i.e. $F_{uc} = \sqrt{F_x^2 + F_y^2 + F_z^2}$ and $\tau_{uc} = \sqrt{\tau_y^2 + \tau_z^2}$, which was aimed to reduce as much as possible.

To gain a general idea about the magnitude of force/torque in the presence and absence of extra passive DoFs, I calculated the mean of the total, controlled and uncontrolled force/torque over all subjects and all trials for each situation. Figure 5.22 shows a significant reduction in the magnitude of the force/torque when gravity is compensated but also when passive DoFs are freed.

Releasing the passive DoFs and gravity compensation reduce the total force from 3.1 N to 1.2 N (approximately 61.3% reduction) and total torque from 18.3 $N.cm$ to 7.9 $N.cm$ (approximately 56.7% reduction).

Figure 5.23 illustrates the levels of the controlled torque and the uncontrolled force/torque versus the position averaged over all subjects. Figure 5.22.c demonstrates that the method presented can reduce the amount of undesired force/torque by 70% and 67.9%, respectively. This figure further shows that the gravity compensation is working correctly, as it is able to remove the part of the torque applied around the PS axis that is a function of the position, making the interaction torque uniform throughout the workspace. It can also be observed that releasing the passive DoF does not alter the force transmission of the Wrist robot (*i.e.* the controlled torque) as it does not affect τ_x. However, releasing the passive DoFs leads to an important beneficial reduction on the level of uncontrolled forces and torques.

Another interesting result shown in Figure 5.23 is that gravity compensation eliminates dependency of the “controlled” force/torque on wrist position but also, surprisingly, it has the same effect on the “uncontrolled” directions. This could indicate a modification of the motor strategy change in the subjects due to gravity compensation activation. Alternatively, the torque generation around PS axis by the forearm muscles may produce additional small forces (or displacement leading to torque) in other directions. Hence, as soon as the amount of PS torque required to move the robot (τ_x) reduces, the forces on other directions are also reduced which is consistent with my observations in Figure 5.23, that the amount of force/torque reduction due to gravity compensation is non-negligible even on the axes that should not be affected by compensation.

Figure 5.24 allows for a more detailed investigation of the effect of the releasing passive DoFs by showing the effect of the two tested conditions on every single component of force and torque. According to these results, releasing the passive

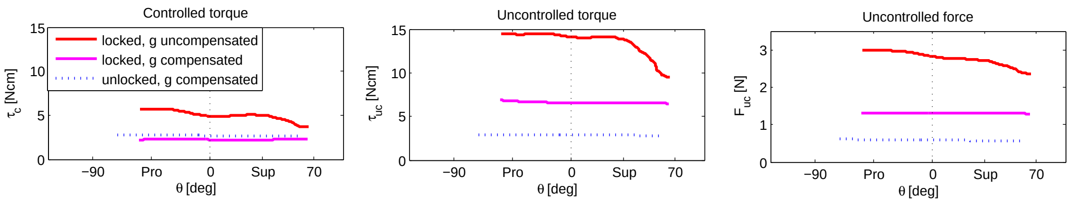

Figure 5.23: Controlled ($\tau_c = \| \tau_x \|$) and uncontrolled ($F_{uc} = \sqrt{F_x^2 + F_y^2 + F_z^2}$, $\tau_{uc} = \sqrt{\tau_y^2 + \tau_z^2}$) force/torque for all subjects throughout the PS workspace, using the ErgoExo.

DoFs does not significantly affect uncontrolled components, i.e. τ_z, F_x and even F_y, for which the force magnitude even increased slightly. However, comparing the levels of F_z for the locked-unlocked condition in Figure 5.24 left side-bottom, reveals a massive reduction on this undesired force acting along side the handle. Similarly, an important decrease of the torque components τ_y and τ_z is observed, indicating a reduction of these uncontrolled torque components interacting with the RUD and FE degree-of-freedom of the subjects. Using the combined gravity compensation and passive DoF mechanism reduced τ_y from 13.3 $N.cm$ (maximum value) to 0.6 $N.cm$ and τ_z from -6.0 $N.cm$ (maximum value) to 2.8 $N.cm$.

As designing and manufacturing an ergonomic handle as the ErgoExo could be time consuming and costly, and some finger strength might be needed to keep the handle in the proper position, using an optimum handle such as ErgoExo might not be practical or convenient for all applications. Hence, along with the experiments with this handle, I evaluated the performance of a simplified passive DoF handle. Taking the results of the ErgoExo into consideration, e.g. investigating Figure 5.24, reveals that the translational and rotational DoFs about FE axis have a critical effect on uncontrolled force/torque. I thus simplified the handle to partly address the problem of hyperstaticity, by releasing only these

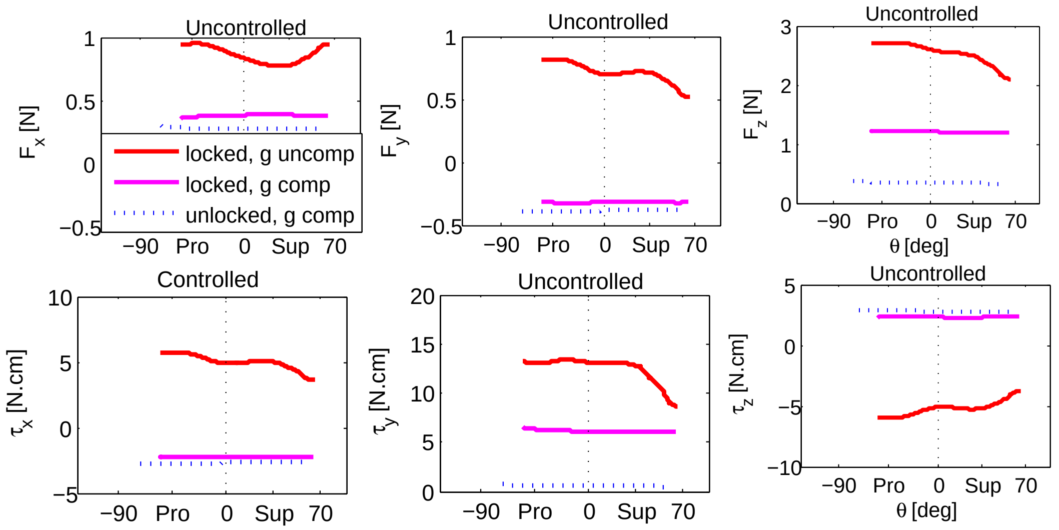

Figure 5.24: The components of force/torque for all subjects throughout the PS workspace. τ_x is controlled and the rest are uncontrolled force/torque components.

Table 5.1: Mean and standard deviation of controlled and uncontrolled force and torque for ErgoExo and simplified handle. $\boldsymbol{F}_{uc}$, $\boldsymbol{\tau}_{uc}$ are uncontrolled force and torque, and $\boldsymbol{\tau}_c$ is controlled torque.

Movement condition		mean±SD of force/torque		
		F_{uc} (N)	τ_{uc} [N.cm]	τ_c [N.cm]
ErgoExo	locked, g uncomp	2.8±0.9	16.5±5.3	6.6±3.3
	locked, g comp	1.3±0.5	9.6±3.5	3.9±2.8
	unlocked, g comp	0.7±0.6	5.3±2.3	2.9±2.3
Handle	locked, g uncomp	3.1±0.1	16.7±0.5	5.5±1.4
	locked, g comp	1.8±0.3	6.3±3.0	3.8±0.4
	unlocked, g comp	0.9±0.1	6.2±1.7	2.2±1.8

two important DoFs. As it is shown in Table 5.1, this simplified solution (i.e. introducing a sliding pivot joint in the handle) already allows to obtain 70% of the uncontrolled force/torque reduction capability of the ErgoExo handle.

Influence of Hyperstaticity on motor strategies

Experimental setup

To study the influence of releasing extra DoFs on motor strategies, I conducted an experiment similar to [23; 92]. Three healthy subjects with no known history of neuromuscular impairment, who declared themselves to be right-handed, were instructed to perform the *center-out* experiment. Each experiment contained 20 trials of which five were training trials designed to familiarize subjects with the task. These training trials were excluded from the analysis while the 15 remaining trials were used for further analyses. The experiment conditions were: i) Free movements, ii) wearing exoskeleton illustrated in Figure 5.20 while extra DoFs are released and iii) similar to item (ii) while the extra DoFs are locked.

To ensure pure movement of the wrist and minimum movement of the elbow, shoulder and torso during the experiment, each subject was asked to be seated on a chair with his/her forearm strapped to the arm-support as shown in Figure 5.25. The orientation of the wrist, R, was captured by means of a motion tracking sensor (MTx-28A-33-G25 device from XSens Inc.). At 120Hz, the se-

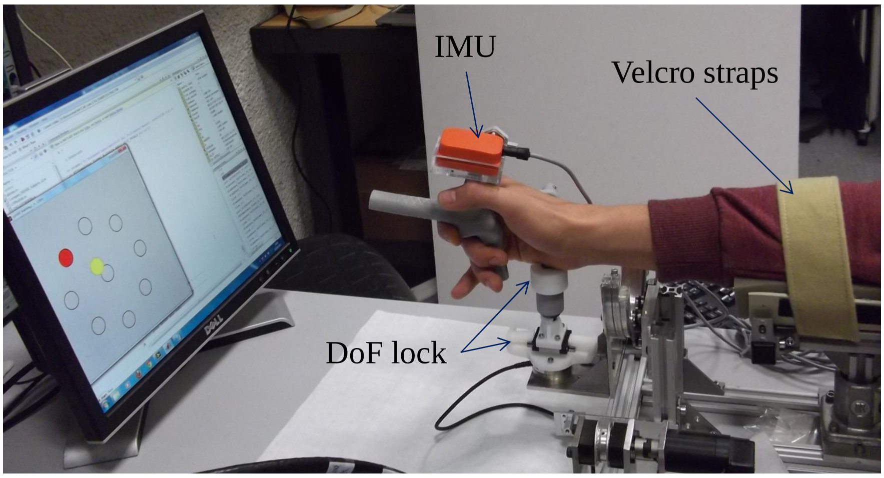

Figure 5.25: Experimental setup to conduct the Centre-out experiment.

quence of orientation matrices, R_i (representing the i-th sample) was downloaded onto a PC for offline data analysis. During the movements, real-time visual feedback was provided for the subject. A zeroing procedure was performed before the start of each trial to define the wrist's anatomical neutral position. For details see Section 3.2.

Analysis

Following Section 3.3, wrist orientations, R_i, for each trial were represented as 'rotation vectors,' a three-dimensional axis-angle representation which allows to visualize rotations as points in a 3D space. In line with my previous work [14], I found that, although three-dimensional in nature, experimental data could be fitted to the so-called Donders' surfaces, a solution to the kinematic redundancy. Figure 5.26 represents the superimposed Donders' surfaces for the three experiments for the subjects.

To analyze the 'shape' of the Donders' surfaces using the method discussed in Section 3.3, I computed Koenderink's Shape Index (through eq. (3.13)). Independent of curvature's amount, this index reflects the intuitive notion of shape and allows me to better compare the shape of the Donders' surfaces between each condition.

A non-parametric analysis of variance (Kruskal-Wallis test) was applied to each trial to understand the differences in shape between each condition. Shape index was used as the dependent variable. Pairwise comparison based on Kruskal-Wallis statistics (using the Matlab R2011a `multcompare` function) revealed between-group differences with a 95% confidence level for the experiment conditions for one of the subjects and no significant difference for the rest. My solution made

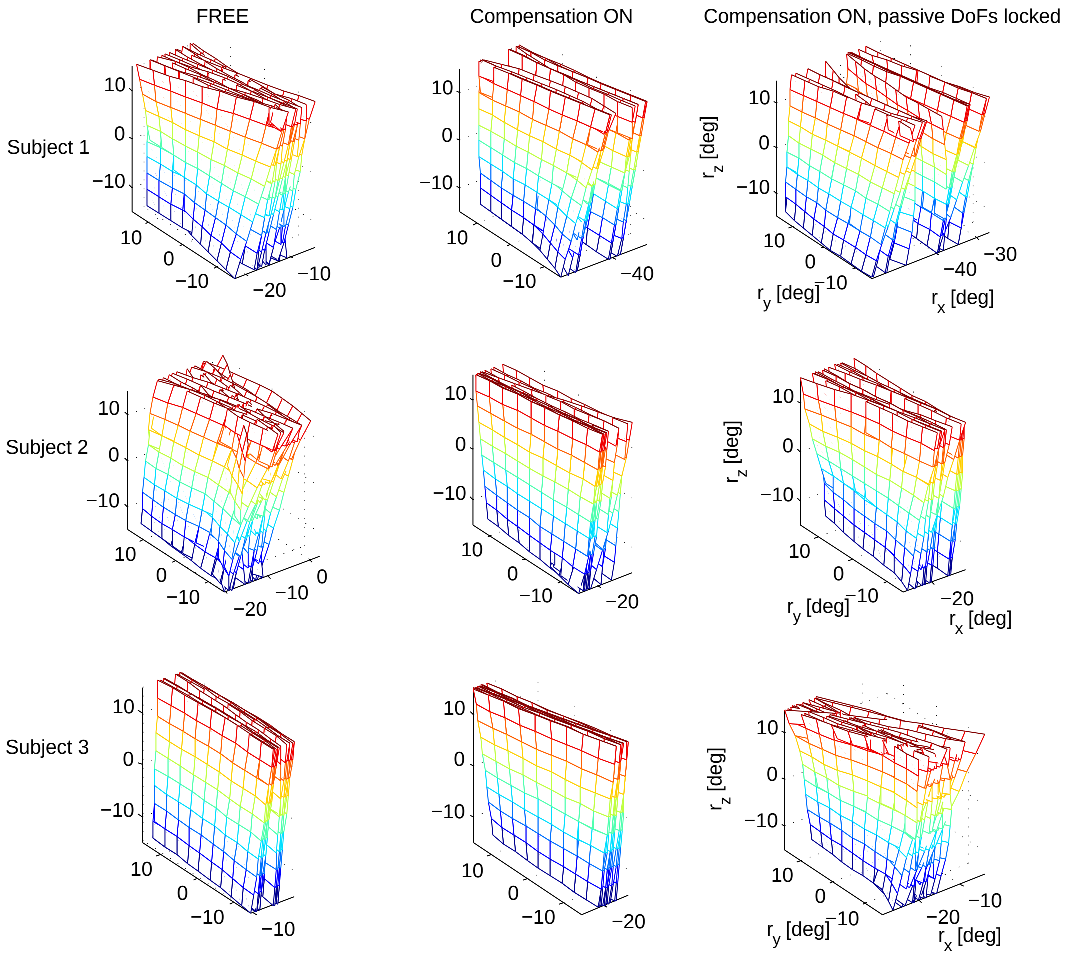

Figure 5.26: Donders' surfaces of all trials for all subjects. Each row represents the results for one of the subjects. The columns from left to right, respectively, illustrate: free movements, movements using wrist robot while all DoFs are released, and movements with locked extra DoFs.

a reduction in the magnitude of undesired force and torques, my results on the motor strategies analysis (kinematics aspects of the tasks) reveals adding extra degrees-of-freedom is not changing motor strategies for two of the subjects.

5.4 Discussion

5.4.1 Numerical study

I evaluated the response of the exoskeleton in terms of kinematic incompatibility and reaction forces in wrist joint by simulating imposed movements at the human joints (within a physiological range of motion). Although the exoskeleton in Figure 5.4 comprises various extra (prismatic) joints, to allow different users to wear the exoskeleton, during operation all these extra prismatic joints are meant to be locked. Therefore, the exoskeleton is a 2–DoF system. Any misalignment would make it kinematically incompatible (kinematic discrepancy) with the human 2–DoF wrist unless some compliance is allowed. The distal part of the exoskeleton is attached to the hand through a handle while the proximal part is meant to be attached to the forearm. I focused on the hand-handle attachment since, is more prone to relative motion and is less addressed in literature, to the authors' knowledge. To do so, I considered a non-rigid attachment between hand and handle by implementing a set of four non-collinear springs.

My simulations quantified the amount of kinematic mismatch between the human joint angles and the exoskeleton counterparts caused by joint misalignment.

Such a kinematic mismatch should be taken into account especially when the exoskeleton is being driven, imposing movement to the human joints. Typically, it is assumed perfect match between human and exoskeleton joint angles while my simulations show that large errors (e.g. 20% relative error in Figure 5.6) might arise. This suggests that the human joint angles should be measured separately from the exoskeleton joint angles, where on current robots, the joint angles are measured at the robot and not at human side.

Although the exoskeleton joints are not actuated in my study, reaction forces still arise due to kinematic mismatch, as highlighted by my simulations. As mentioned in [40], kinematic discrepancy is one of the causes for reaction forces. Since my exoskeleton is located on the volar side of the wrist, it causes asymmetric kinematic mismatch between exoskeleton and wrist for flexion rotations in presence of misalignments. These reaction forces do not perform work on the human joint but cause discomfort, or worse, pain.

Despite the oversimplifications, this work highlighted that misalignments would result in kinematic discrepancies and generation of interaction forces in pHRI. Kinematic mismatch would then make an exoskeleton 'non-transparent', causing movement perturbation. Since, the discomfort is asymmetric, choosing an offset for the exoskeleton based on the average offset for the human joints, might not be optimal from a 'one-size-fits-all' perspective. Based on the *aggregate loss* minimization concept, I numerically found that a 4mm offset for the exoskeleton joints, instead of a 6.8 mm average (as from the experimental distribution of human offsets), would actually determine the optimal one-size-fits-all.

5.4.2 Experimental study

Through *center-out* experiment the design of the wrist exoskeleton which meant to comply with the natural coordination mechanisms in the redundant wrist is investigated. Comparison of the results in Figure 5.12 between the ComfGrip handle with those of the PS locked, i.e. *only handle* and *locked PS*, respectively, reveals that locking one DoF has a strong influence on the subject. As anticipated, the locked PS case resulted in particularly consistent surfaces across all trials (refer to Section 5.2.2). Moreover, as Figure 5.13.b shows, the values of shape index of the experiments with locked PS, black stars, are closely distributed about this line, demonstrating wrist as a 2D gimbal in the absence of PS DoF which is consistent with my expectations in Section 5.2.2. A non-parametric analysis of variance (Kruskal-Wallis test) was applied to each trial to understand the differences in shape between each condition. Shape index was used as the dependent variable, the experiments were the grouping factor and statistical differences for the median of each group were identified ($p < 10^{-7}$). Pairwise comparison based on Kruskal-Wallis statistics (using the Matlab R2012a `multcompare` function) revealed group differences with a 95% confidence level. Specifically, the shape index distributions for *misaligned exoskeleton* and *locked PS* are significantly different from *only handle* and *aligned exoskeleton*, respectively, with a 95% confidence level.

5.4.3 Hyperstaticity

Releasing passive DoFs, i.e. preventing hyperstaticity and its consecutive uncontrolled forces/torques, resulted in a reduction of uncontrolled torques by approximately 45%. As my results illustrate, accounting for passive DoFs could be as effective as considering gravity compensation in the reduction of undesired forces/torques for rehabilitation robots.

My results show a correlation between different force/torque components, i.e. improving force in a direction results in improvement or change of force in other directions. For instance, Figure 5.24 demonstrates that reduction of the undesired τ_z also lead to a reduction of τ_x. Therefore it is useful to consider all forces in the design phase of the robot since a reduction of resistive force on one axis may modify the whole motor strategy due to adaptation neuromotor mechanisms.

The results from my force analyses demonstrate how undesired forces might arise due to kinematic discrepancy between human and robot. More importantly, the centre-out experiment confirmed that adding the extra passive DoFs could not avoid changes in motor strategy during a redundant task for one of the subjects, however, for the rest of the subjects no statistically significant difference was found for the movements. Thus, the presented solution could be taken into account in the early phase of design of robots. It could also be applied to modify the fixation points of commercial robots in order to reduce the magnitude of reaction forces.

Chapter 6

Towards Haptic Devices Compatible with Neural Constraints

As it is discussed earlier, in Section 1.2, providing haptic feedback requires a transparent mechanism, here the effects of the inertia at the prono-supination (PS) joint on the transparency of the robot is emphasized. For this reason, I start with actuating the PS joint and leaving the remaining joints passive. Furthermore, the possibility of using the PS joint as a haptic channel finds interesting applications, for example in minimally invasive surgery (MIS). Recent work by Masia et al. [57], shows how haptic feedback through PS during visuo-motor rotation tasks enhances learning and adaptation of the users.

Here, I present two wrist robots, both actuated at the PS joint. The first robot is equipped with a load-cell, for force measurements, but this excessive inertia perturbs pointing tasks for most of the subjects. The second robot, similar to the first but without the load-cell, does not perturb motor strategies during pointing tasks for most of the subjects.

6.1 Transparency in Human-Robot Interaction

Two important aspects of HRI are physical and cognitive interactions which are correlated. Hence, a cognitive interaction can be used to alter the physical interaction between human and machine and also a physical interaction with the machine can bring about a cognitive process [50; 67], more details in Section 2.2. At the cognitive level, recent studies [57; 59; 76; 91; 103] reveal a high demand on investigating the benefits of various forms of haptic feedback when synchronized with the visuo-motor misalignment especially for the precise applications, such as minimally invasive surgery (MIS). In particular, a great interest exists on quantifying the impact of haptic feedback on visuo-motor learning and adaptation mental processes of the users in typical manipulation tasks, e.g. MIS. Moreover, a recent behavioral study (Masia et al. [57]) showed that a kinesthetic feedback, added to the visual feedback and synchronized with the visuo-motor rotation, can effectively improve the kinematic performance in basic pointing tasks, i.e. reducing the cognitive burden on the surgeon's side.

Transparency in literature is addressed in two 'some-how' different categories: *telerobotics* and *wearable robotics*. In telerobotics, transparency is defined as the match between the impedance perceived by the operator and the environment impedance [33; 49; 88]. Transparency in the second application, that concerns my research, is interpreted also as *comfort* of the user during the operation. In wearable robotics, a robot that is not altering the natural movement of the user and also interacts smoothly with the user is considered transparent [24; 39; 67; 80; 92]. The most common approach implemented in literature to evaluate the degree of transparency of wearable robots is the analysis of the reaction forces during operation [24; 39; 80]. The other approach is neural constraints assessment during the task that is implemented in the recent works [23; 92]. In my thesis I applied the both approaches. The first one, i.e. analyzing the reaction forces, is reported in Chapter 5 and the second approach is used in this chapter.

Recent research has shown how even state-of-the-art robots designed for neurorehabilitation of the human wrist might not be transparent and perturb natural motor strategies in healthy humans during redundant tasks [11]. Campolo et al. performed a 2D pointing task under two scenarios: free movements and using a commercial robot. They extracted the $C1...C6$ coefficients relative to the rotations for each of their subjects and reported the average of five trials in Table II of their paper [11]. Using the C coefficients, I calculated the *mean curvature* (H), *Gauss curvature* (K) and *Koenderink's index* (S), respectively, through the equations (3.11), (3.12) and (3.13), as presented in Table 6.1. As it is explained earlier in Section 3.3, *mean curvature* is the mean of largest and smallest section curvatures, *Gauss curvature* corresponds to their product and *Koenderink's index* captures the intuitive notion of shape independently of the curvature's amount.

Figure 6.1 is generated based on the values reported in Table 6.1. The solid horizontal and vertical red lines intersecting at $H_{locked} = 0\,rad^{-1}$ and $K_{locked} = -\frac{1}{4}\,rad^{-2}$ for the case of 2D gimbal, discussed in Section 5.2.2. As highlighted in [11] the movements of all the subjects are heavily perturbed by the InMotion3 robot and statistically not different from a 2D gimbal case.

Since in 2D gimbal the PS is locked, a clear message here, in line with lit-

Table 6.1: The *mean curvature* (H), *Gauss curvature* (K) and *Koenderink's index* (S) for the C coefficients reported in [11] for InMotion3.

Subjects	mean (H)	Gauss (K)	Koenderink's index (S)
1	0.0044	-0.2188	-0.0060
2	0.0041	-0.2531	-0.0052
3	-0.0145	-0.2824	0.0174
4	0.0045	-0.2575	-0.0056
5	0.0095	-0.2546	-0.0120
6	-0.0002	-0.2500	0.0003
7	-0.0479	-0.2531	0.0602
8	0.0107	-0.2549	-0.0135
9	0.1132	-0.2712	-0.1332
10	0.0174	-0.2581	-0.0218

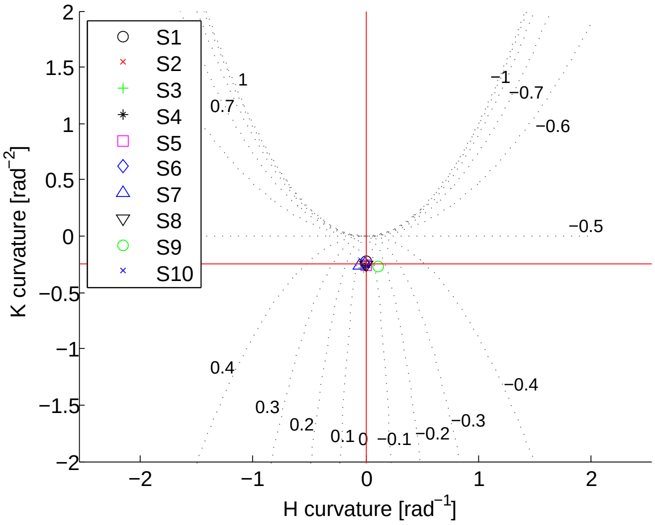

Figure 6.1: Mean curvature (H) vs. Gaussian curvature (K) for all trials and all subjects for the experiments reported in [11] done by InMotion3.

erature, is that even though the InMotion3 robot is backdrivable, due to the redundancy in the wrist, the high perceived impedance on PS causes subjects not to involve their PS DoF incorporating only the FE and RUD DoFs in the movements. Thus, inertia of robot PS joint (i.e. the most proximal joints) plays a crucial role in the wrist platforms in the sense of transparency.

To improve the transparency of InMotion3, in a recent study, Tagliamonte et al. [92] actively compensated for the gravity, friction and inertia of the PS degree-of-freedom. They also applied a force control by adding a loadcell between the handle and the body of the InMotion3 to evaluate the possibility of further reduction of perceived inertia on PS to increase the degree of transparency of the robot. As they have reported in [92; 94; 95] their approach could successfully reduce the perceived inertia and also reaction force by over 70%. The problem though is that through the force control approach, there is a limit (about 3 times) for the reduction of the perceived impedance, meaning any further reduction would make the robot unstable. This also shows to increase the degree of transparency in a robot, the mechanical structure of the robot plays an important role too. Besides, it should be noted that the physical damping of the robot directly effects on the maximum passive impedance that a robot can contribute [101]. Therefore, in my study, I paid special attention to the design of the robot, as it is presented in the previous chapters, and also to the control of my robot that is discussed in this chapter.

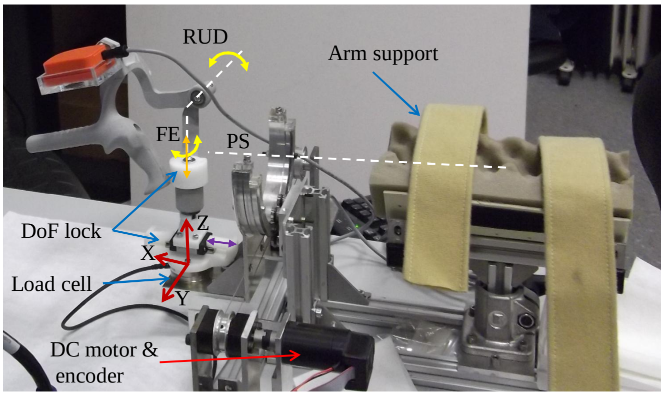

Figure 6.2: The wrist robot used as the platform to study motor synergies.

6.2 PS-actuated wrist robot

The wrist robot shown in Figure 6.2 is a one active DoF measurement device, actuated at PS joint. Its kinematics is composed of one pivot whose axis is intended to be coincident with that of prono-supination movements.

Table 6.2, shows the equipments used for devising the wrist robot and performing the experiments. Control (for gravity and friction compensation) and data logging are implemented in `MATLAB R2011b/dSPACE` real-time environment with sampling rate at 1 kHz. Data from the force sensor and encoder are sam-

Table 6.2: Components used to fabricate the wrist robot and implement the control.

Component	Specification	Manufacturer/released by
MATLAB	2011b	MathWorks, Inc.
dSPACE	DS1103 PPC Controller Board	dSPACE GmbH
Force sensor	Mini40-E Transducer, 6-DoF	ATI Industrial Automation, Inc.
Encoder	HEDL 5540 optical, 3 channels, 500 pulses per revolution	Avago Technologies
DC motor	3242G012CR	Faulhaber GmbH & Co.
Current servo	Ocarina OCA 5-60	Elmo Motion Control Ltd.

pled and used to control the DC motor. The DC motor is coupled to the ring via cables (reduction ratio: 3.9) to transmit the required driving torque. The current servo is used to drive the DC motor.

6.2.1 Actuator characterization

The motor used in the wrist robot was rated with a stall torque of 181 mNm and torque constant, k_m, at 20.6 mNm/A. To identify k_m, I performed a static torque test by applying different current levels to the motor and measuring the torque through the Mini40-E force transducer while the PS joint was rigidly fixed to the robot as shown in Figure 6.3.a.

As I am interested in the PS torque at the human wrist (τ^{PS}), ideally where all the wrist axes intersect, the torques and forces measured at the load-cell, are converted through $\tau^{PS} = \tau_x - d_z F_y$. τ_x is the torque about x axis at the load-cell, F_y is force on y-direction and d_z is the vertical distance between the load-cell and human wrist center of rotation. Then, knowing the pulley ratio, i.e. ring radius (R_r) over pulley radius (R_p), I calculated τ_{motor} from τ_{PS} as $\tau_{motor} = (R_p/R_r)\, \tau_{PS}$.

The resulting data are presented together with the linear best-fit equation in the Figure 6.3.b. I found the slope of the linear fit in Figure 6.3 to be $k_m = 12.25 mNm/A$.

6.2.2 Gravity term characterization

To evaluate the gravity term for the Prono-Supination DoF, I performed a correlation between different static configurations and the torques required to hold the robot in those positions.

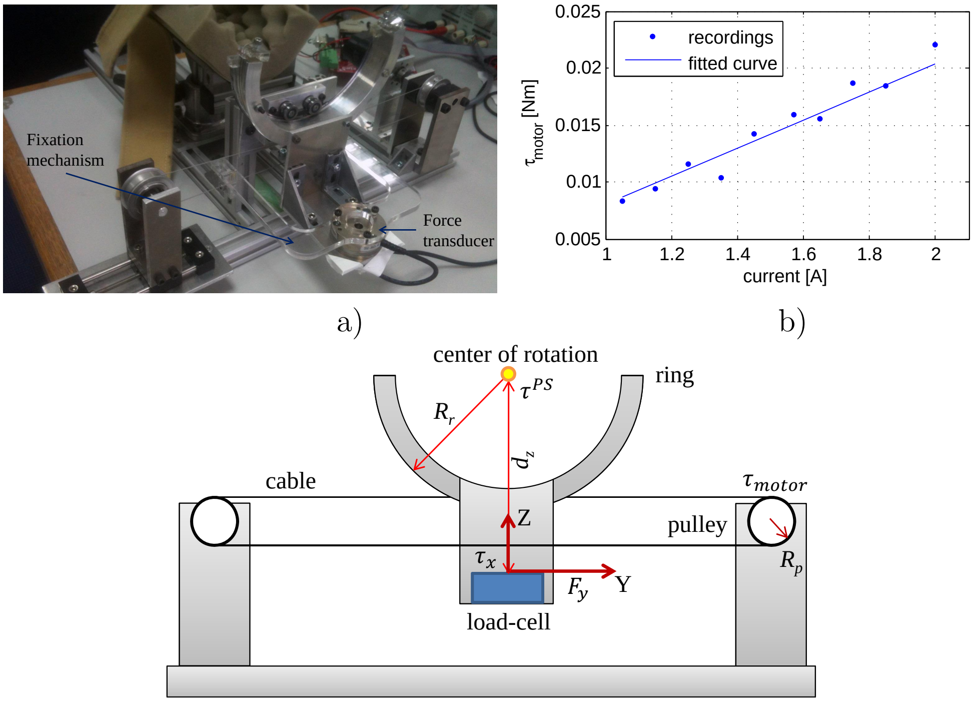
Fixation mechanism
Force transducer
0.025
0.02
0.015
0.01
0.005
τmotor [Nm]
recordings
fitted curve
1
1.2
1.4
1.6
1.8
2
current [A]
center of rotation
ring
τPS
Rr
dz
cable
τmotor
Z
pulley
τx
Rp
Fy
Y
load-cell

a) b)

c)

Figure 6.3: Motor torque constant (k_m) characterization setup (a). Plotting the τ_{motor} vs. applied current (b) resulted in a k_m value of 12.25 mNm/A. The d_z, R_r and R_p in (c) are the distance from load cell to the center of rotation, radius of the ring and radius of the pulley used to calculate τ_{motor} from force transducer reading.

The handle shown in Figure 6.2 (no movements on RUD and and FE DoFs) was used to conduct the test. Following [47] the contribution of RUD and FE degrees-of-freedom on the PS gravity term is neglected since the load produced by the handle on the PS joint can reasonably be considered independent of the RUD and FE orientations of the robot in the range of operation.

The robot was commanded to reach 21 positions (from -0.7 to +0.7 rad with respect to its rest position); PS actuator torques exerted to maintain these rotations in static conditions were evaluated.

The gravity term was assumed to vary sinusoidally with PS angle so a linear

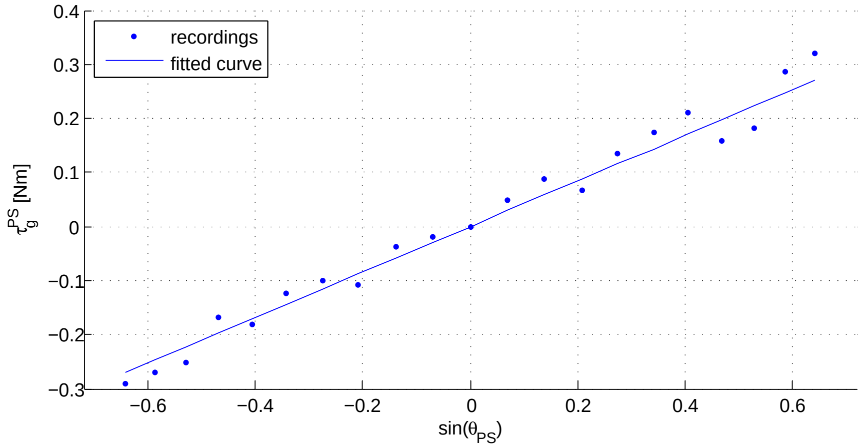

Figure 6.4: Linear regression between τ_g^{PS} and $\sin(\theta_{PS})$ static values for the estimation of the Prono-Supination gravity term. The fitting curve slope gives the gravitational term as $\tau_g^{PS} = g_{PS}\sin(\theta_{PS}) = 0.42\sin(\theta_{PS})$.

regression between PS torque, τ_{PS}, and the sine of the PS rotation, $\sin\theta_{PS}$, was calculated. In Figure 6.4, the resulting data (static PS angles and torques) are shown together with the best-fit curve. The slope of the linear fit in Figure 6.4 was found to be $g_{PS} = 0.42Nm$.

6.2.3 Inertia and friction characterization

To estimate inertia and friction terms, the robot was manually back-driven, with the gravity compensation on, through several rapid oscillation movements. I estimated the inertia and friction terms for the PS joint by regression between the τ^{PS}, the torque on PS joint, with angular velocities and accelerations of the Prono-Supination DoF, as demonstrated in

$$\tau^{PS} = \tau_0^{PS} + b\dot{\theta}_{PS} + B\ddot{\theta}_{PS} \tag{6.1}$$

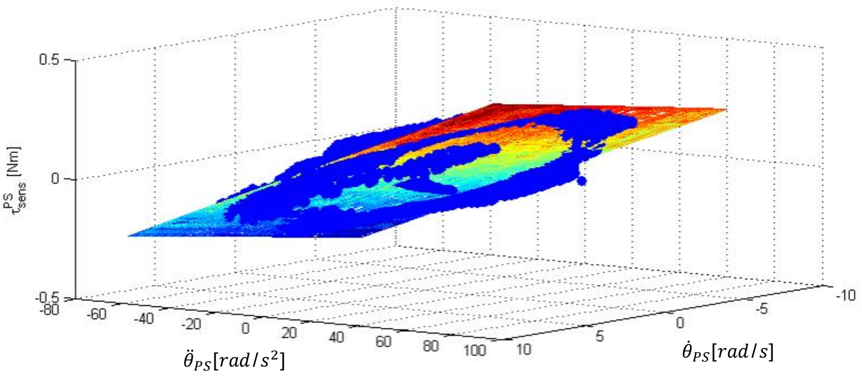

Figure 6.5: Multivariable linear regression for PS inertia and friction characterization as reported in (6.1). Considering the values averaged on 10 trials, a viscous friction $b = 0.0121\,Nm.s/rad$ and an inertia $B = 0.0045\,kg.m^2$ were found.

The multivariable linear regression reported in eq. (6.1) was performed on 10 trials; the plane of best-fit shown in Figure 6.5. I found a viscous friction $b = 0.0121\,Nm.s/rad$ and an inertia $B = 0.0045\,kg.m^2$.

To identify the static friction, τ_0^{PS}, I commanded the robot to move back to zero from 20 different positions, 10 positions within pronation and 10 positions within supination domain, and recorded the required additional current, i, on top of the current needed to compensate for gravity, to initiate each movement. From this the required torque was estimated as $\tau_{st}^{PS} = k_m.i$.

Through a linear regression between PS torque, τ_{st}^{PS}, and the the PS rotation, θ_{PS}, the static friction term was calculated. In Figure 6.6, the resulting data (static PS angles and movement initiating torques) are shown together with the best-fit curve. The value of the linear fit in Figure 6.6 was found to be $\tau_0^{PS} = 5.109\,mNm$.

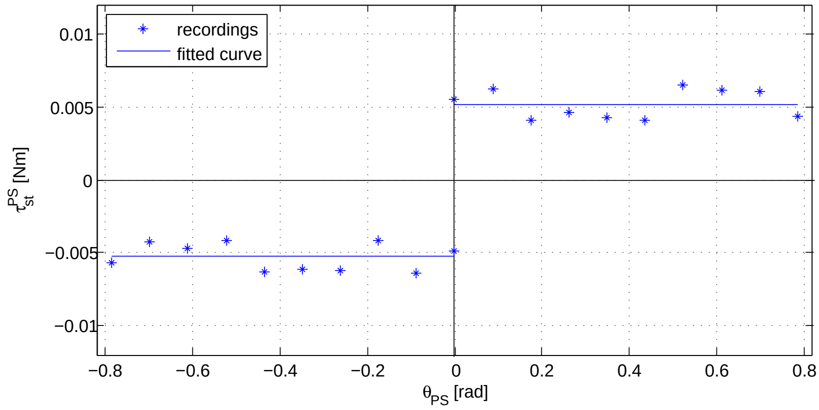

Figure 6.6: Linear regression between τ_{st}^{PS} and θ_{PS} static values for the estimation of static friction term. The fitting curve gives the torque required to overcome static friction, τ_0^{PS}, as $5.109\, mNm$.

6.2.4 Gravity and friction compensation

The control scheme presented here, adapted from [94; 100], is used to compensated for the gravity and friction. The implemented control model is

$$\tau^{PS} = \tau_g^{PS} + \tau_{st}^{PS} + \tau_{visc}^{PS} \tag{6.2}$$

where, τ_g^{PS}, is the gravity term, τ_{st}^{PS}, is the static friction term and τ_{visc}^{PS}, is the viscous friction term. Since slow movements are involved in our experiments, the coriolis, centrifugal and inertial effects have been neglected in our control model. Figure 6.7, illustrates the block diagram of the implemented control algorithm. The static friction is modeled as

$$\tau_{st}^{PS} = \begin{cases} -\tau_0^{PS}, & \text{if } |\tau_{sens}| > 0 \;\&\; \dot{\theta}_{PS} < 0.4 \;\&\; \tau_{sens} > 0 \\ +\tau_0^{PS}, & \text{if } |\tau_{sens}| > 0 \;\&\; \dot{\theta}_{PS} < 0.4 \;\&\; \tau_{sens} < 0 \end{cases} \tag{6.3}$$

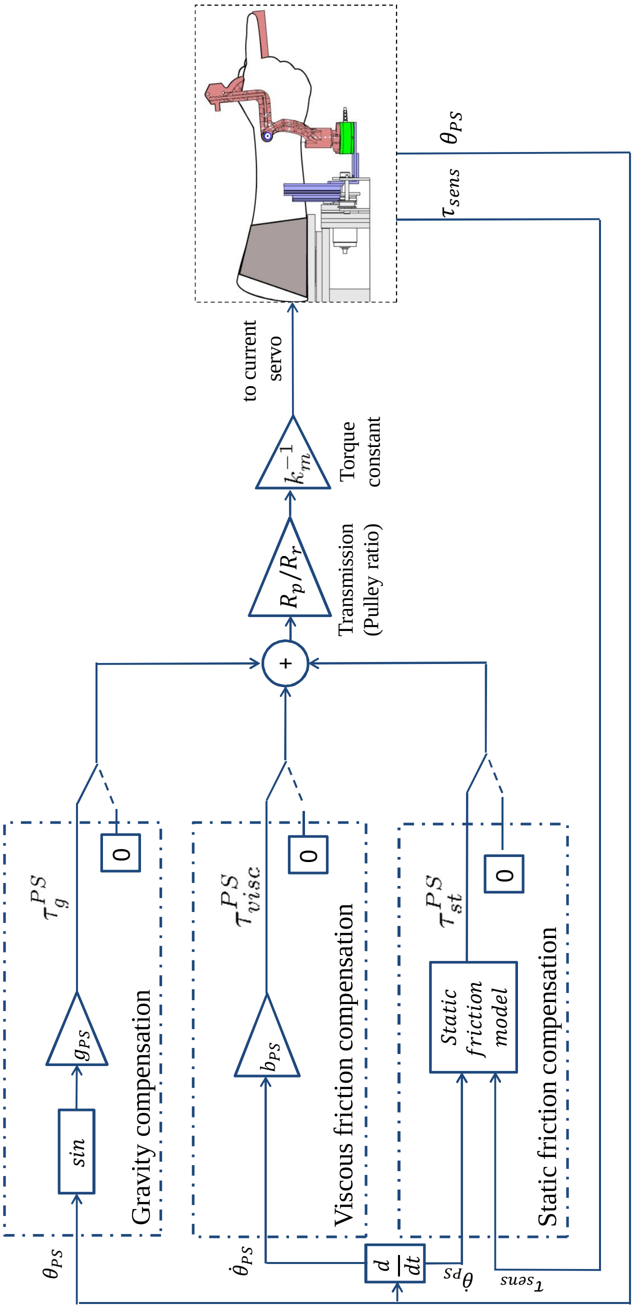
θ_{PS}
τ_{sens}
to current servo
k_m^{-1}
Torque constant
R_p/R_r
Transmission (Pulley ratio)
+
τ_g^{PS}
0
g_{PS}
sin
Gravity compensation
τ_{visc}^{PS}
0
b_{PS}
Viscous friction compensation
τ_{st}^{PS}
0
Static friction model
Static friction compensation
θ_{PS}
$\dot{\theta}_{PS}$
$\frac{d}{dt}$
$\dot{\theta}_{PS}$
τ_{sens}

Figure 6.7: Control scheme.

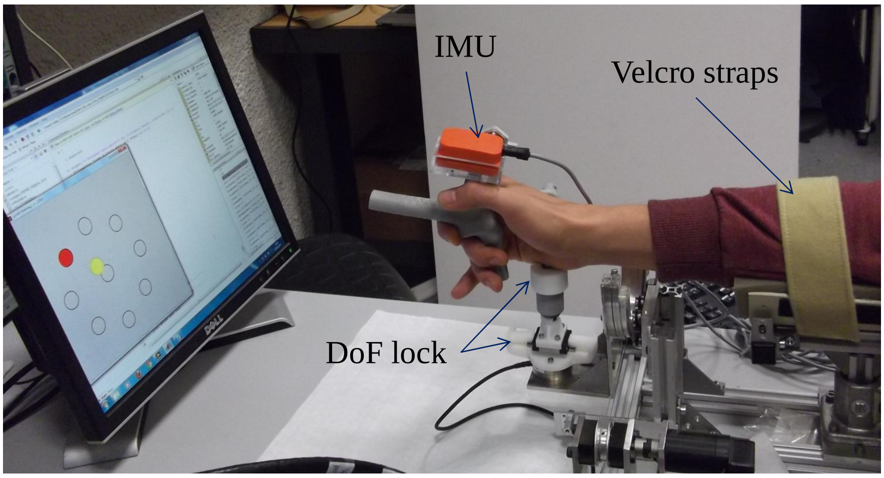

Figure 6.8: Experimental setup to conduct the Centre-out experiment.

6.3 Influence of the wrist robot on soft constraints

6.3.1 Experimental setup

To assess the transparency of our robot, I conducted the center-out experiment similar to Section 3.2. To ensure pure movement of the wrist and minimum movement of the elbow, shoulder and torso during the experiment, each subject was asked to be seated on a chair with his/her forearm strapped to the arm-support as shown in Figure 6.8.

6.3.2 Protocol

Six healthy subjects, with no known history of neuromuscular impairment, who declared themselves to be right-handed, were instructed to perform the *center-out* experiment. Similar to the task presented in Section 3.2, each subject was asked to point from the central target toward one of eight peripheral targets. A zeroing procedure was performed before the start of each trial to define the wrist's anatomical neutral position, for details see [14]. Each experiment contained 20 trials of which five were training trials designed to familiarize subjects with the task. These training trials were excluded from the analysis while the 15 remaining trials were used for further analyses. The experiment conditions are:

- ***i. Free movements:*** The subject grasps the ergonomic handle[1] to point at each of the 9 targets. The sequence always starts from the center target, move to the one in the periphery (random), and then come back again to the center until all the peripheral targets are hit.
- ***ii. Uncompensated:*** The experiments are similar to condition *i*, but the subject grasps the ergonomic handle which is mounted on the robot. The motor of the robot remains off during the experiment.
- ***iii. Gravity compensated:*** The experiments are similar to condition *ii*, but gravity is compensated during the experiment.
- ***iv. Gravity and friction compensated:*** The experiments are similar to condition *ii*, but gravity and friction are compensated during the experiment.

Similar to Section 5.3.3, I aligned the prono-supination axis for each subject with robot's center of rotation.

---

[1] a comfortable handle developed based on the fencing grip configuration, more details could be found in [23].

6.3.3 Data analysis

Similar to Section 3.3, according to the sequence R_i relative to each trial, the sequence of rotation vectors, r_i, were calculated through eq. (3.8). Then, the generic quadratic surface, $\boldsymbol{r^*}_i = [r^*_{xi} \; r_{yi} \; r_{zi}]^T$, was fitted to the sequence of the first components r_{xi} using the eq. (3.9) to generate the relative *Donders' surface*. Following Section 3.3, determined coefficients $C_1 ... C_6$. Besides, the goodness of fit index is evaluated by calculating the *variance accounted for* via eq. (3.10).

To analyze the 'shape' of Donders' surfaces, calculating the *mean* and *Gauss* curvatures through eq. (3.11) and eq. (3.12), respectively, I computed Koenderink's Shape Index as in eq. (3.13).

6.3.4 Results

Donders' surfaces

Figure 6.9 shows the Donders' surfaces relative to all trials, for each subject (rows) for the case of *free*, *uncompensated*, *gravity compensated* and *gravity-friction compensated* movements. From a visual inspection, two major features appear. The first is that between-subject differences can be appreciated in terms of curvature of Donders' surfaces for all conditions, it is though less evident for *uncompensated* movements. The second feature is the different amount of inter-subject differences observed for subjects under different conditions that would be discussed more in the following sections.

Curvature and shape analysis

For *free*, *uncompensated*, *gravity compensated* and *gravity-friction compensated*

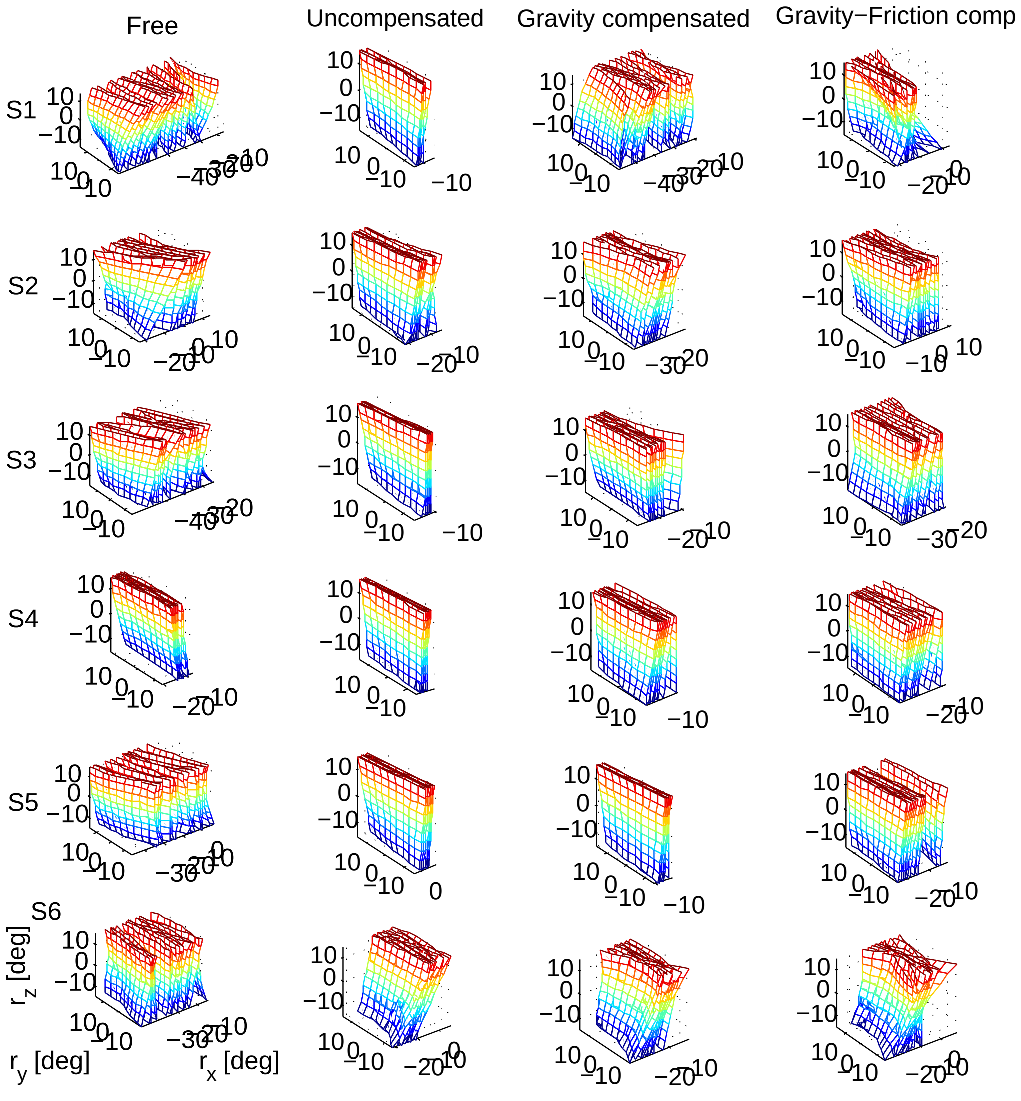

Figure 6.9: Donders' surfaces of all trials for each subject (rows) for *free*, *uncompensated*, *gravity compensated* and *gravity-friction compensated* movements (columns).

movements, gauss curvature K as a function of mean curvature H is presented in Figure 6.10 for all trials of all subjects. Even though the robot is backdriveable, in the absence of gravity and friction compensation, Figure 6.10.b, for most of the subjects the K and H values have fallen in the K_{locked}, H_{locked} neighbourhood. This is an evident that the robot perturbs the motor coordinations, hence most of the subjects' performance are consistent with the 2D gimbal discussed in Section 5.2.2. Gravity and friction compensation has reduced the amount of perturbation obviously (compare Figure 6.10.b with Figure 6.10.c and Figure 6.10.d). yet the movements are different than the *Free* movements.

Subject-specific distributions of shape index is presented in Figure 6.10.e-h. Two major features could be perceived from the shape index. The first is between-group differences for each condition. The second feature, not addressed in previous studies, is that the shape index distribution is changed differently for different subjects, meaning subjects show different level of *sensitivity* to the perturbation. For instance, a comparison between *subject 2* (S2, red crosses) and *subject 6* (S6, blue diamonds) in Figure 6.10.e-h reveals that motor strategies of *subject 2* has been perturbed/changed appreciably due to the mechanical constraints imposed (*i.e.* the mass, friction and inertia felt by the subject on account of the robot). Though *subject 6* shows a change in motor coordination for different conditions, the distribution of the shape index seems wide and similar for Figure 6.10.e, *g* and *h*. It is obvious for the case of *uncompensated* movements, Figure 6.10.f, all subjects present the most change in motor strategies.

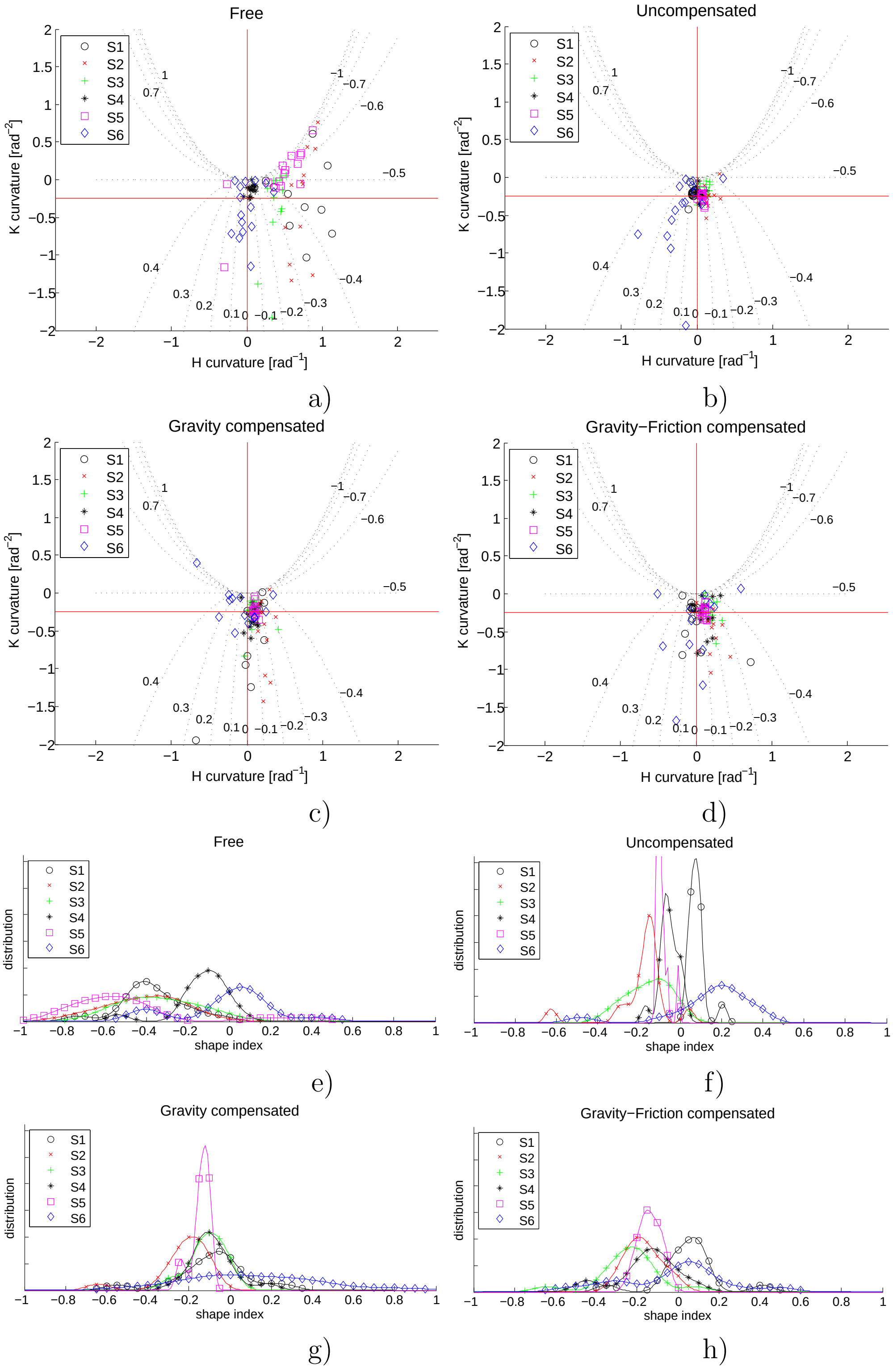

a)

b)

c)

d)

e)

f)

g)

h)

Figure 6.10: a-d) Mean curvature (H) vs. Gaussian curvature (K) for all trials and all subjects for *free*, *uncompensated*, *gravity compensated* and *gravity-friction compensated* movements. Dotted lines indicate *loci* of (H, K) pairs with same Shape Index. e-h) Distribution of shape index eq. (3.13) for all subjects.

6.4 Improving the design to reduce the perceived impedance

Low endpoint impedance is one of the essential features of backdrivable robots [47; 104]. As I discussed throughout this thesis, from the early steps of our design, the main effort was towards reducing the endpoint impedance of the robot as much as possible. Thus, the perceived inertia of our robot, about the prono-supination axis, became $3.4 \times 10^{-3}\, kg.m^2$ which is roughly one fourth of the inertia of one of the most famous state-of-the-art robots commercially available (MIT-MANUS wrist module, InMotion3: $12.0 \times 10^{-3}\, kg.m^2$ [94]) and is close to the human forearm/hand inertia, i.e. $1 - 2 \times 10^{-3}\, kg.m^2$ [99]. In the step after, through a control scheme, presented in Section 6.2.4, I compensated for the gravity and friction to further reduce the endpoint impedance. The presented results in the previous section however, revealed that the robot is perturbing the natural motor strategies in our redundant task. To further reduce the inertia, I removed the load cell, which caused the main portion of the inertia/weight, and also shortened the connecting part, see Figure 6.11. For the updated control scheme, since I removed the load cell, the part related to the friction compensation providing τ_{st}^{PS}, i.e. the last row of the control scheme in Figure 6.7, is also cancelled out.

6.4.1 Method

Twelve healthy subjects (4 female, age range 23-47) were recruited to perform the *center-out* experiment under *free*, *uncompensated* and *gravity compensated* movements conditions as described in Section 6.3.2. The experimental setup is the

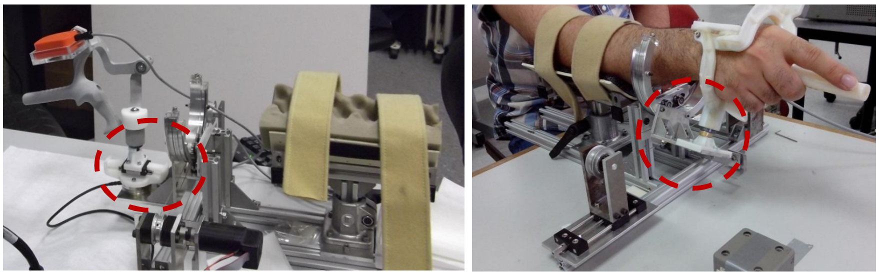

Figure 6.11: The modifications applied to our robot (a) resulted in the robot (b), the inertia could be reduced to less than one third of the original amount (from $3.4 \times 10^{-3}\,kg.m^2$ to $1.0 \times 10^{-3}\,kg.m^2$) and the mass by half (from $0.39\,kg$ to $0.20\,kg$).

robot presented in Figure 6.11.b. The control scheme for gravity compensation is same as the upper part of the block diagram illustrated in Figure 6.7, the g_{PS} though for the modified setup is $0.175\,N.m$.

6.4.2 Results

Thickness distribution and Donders' surfaces

The variance accounted for (VAF) index relative to the fitting[1] of each trial for all subjects is shown in Figure 6.12. This figure confirms the reliability of the fitted Donders' surfaces for the next analysis, e.g. curvature and shape analysis.

The Donders' surfaces relative to all trials, for each subject (rows) and all movement conditions is presented in Figure 6.13. Both between and within-subject differences in terms of curvature of Donders' surfaces is more evident, in comparison with section 6.3.4, for all conditions, even for uncompensated movements.

---

[1] Data from each single trial were fitted with the generic quadratic surface of eq. (3.9).

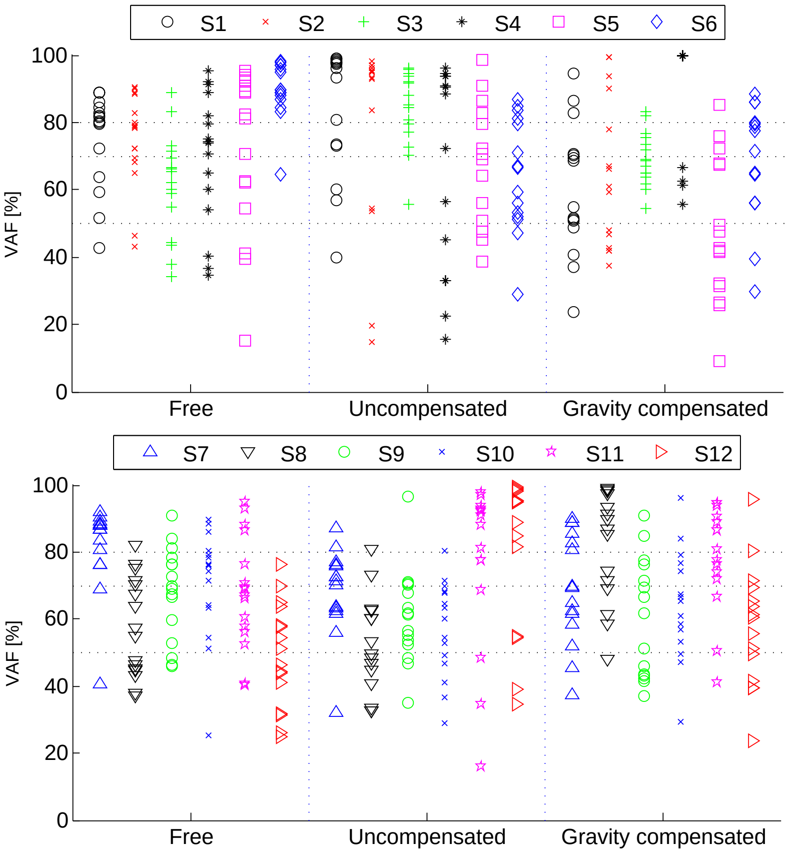

Figure 6.12: Variance accounted for (VAF) for each trial for all movements and subjects.

Curvature and shape analysis

For the experiments conducted by the modified robot, gauss curvature K as a function of mean curvature H is also presented in Figure 6.14.a-c for all trials of all subjects. Between-subject difference could be appreciated for *free* and *gravity compensated* movements. The dotted lines in Figure 6.14.a-c show the *loci* of the equivalent shape index, suggesting subject-specific clustering in terms of shape.

Subject-specific distributions of shape index is presented in Figure 6.14.d-f. Non-parametric analysis of variance (Kruskal-Wallis test) has been performed for all trials, using the shape index as dependent variable and movement conditions

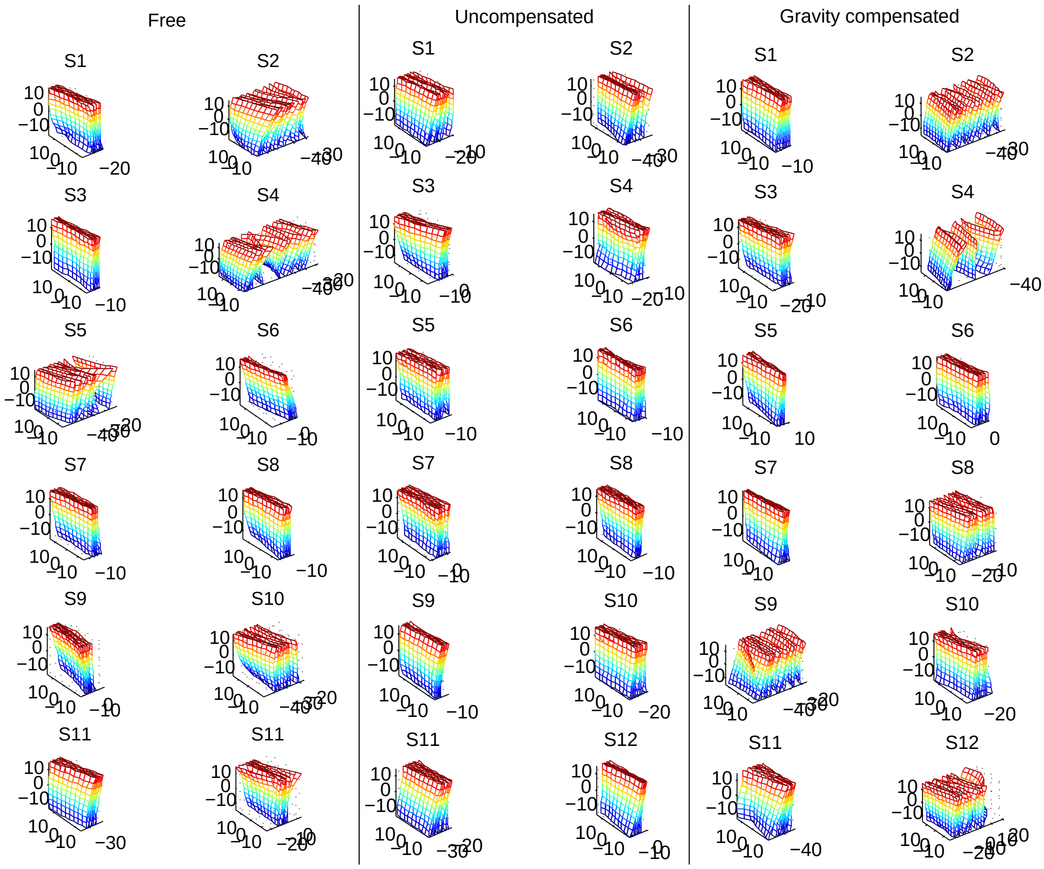

Figure 6.13: Donders' surfaces of all trials for each subject in different movement conditions.

as grouping factor. I performed pairwise comparisons based on Kruskal-Wallis statistics (using the Matlab R2011b `multcompare` function[1]) which showed no significant difference between *free* and *gravity compensated* movements for 9 subjects (S1, S3, S4, S6, S7, S8, S9, S11 and S12) at 95% confidence level. No significant difference between any movement condition was found for three of the subjects (S4, S6 and S12). The shape index distributions for each subject is presented in Figure 6.15 for better inspection.

---

[1] receiving the data in form of MATLAB structure, this function performs a multiple comparison test (through a pairwise t-test at normally a confidence level of 5%) on the data and displays which pairs of means of the received data are significantly different.

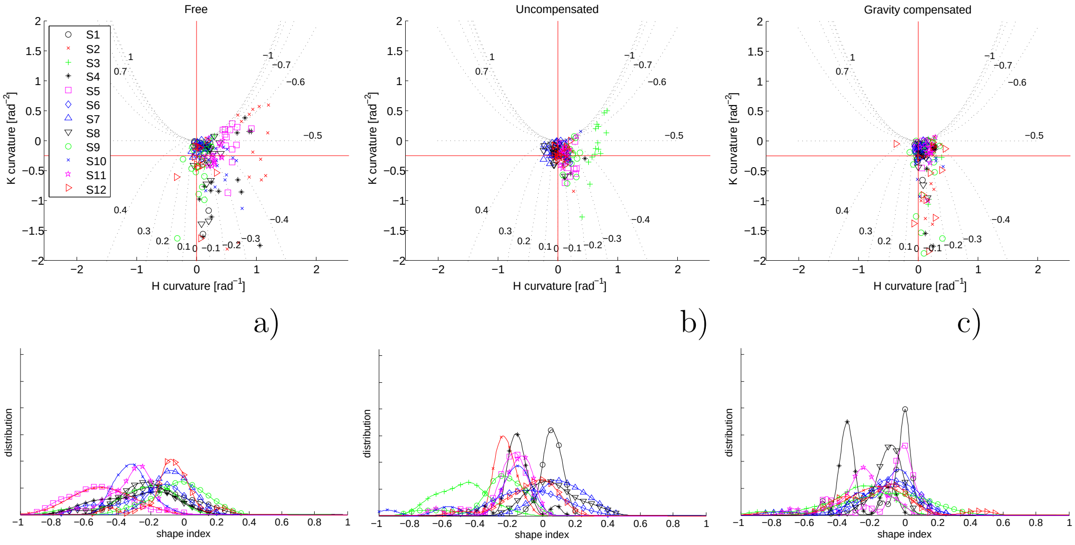

a) b) c)

d) e) f)

Figure 6.14: a-c) Mean curvature (H) vs. Gaussian curvature (K) for all trials and all subjects. Dotted lines indicate *loci* of (H, K) pairs with same Shape Index. d-f) Distribution of shape index eq. (3.13) for all subjects.

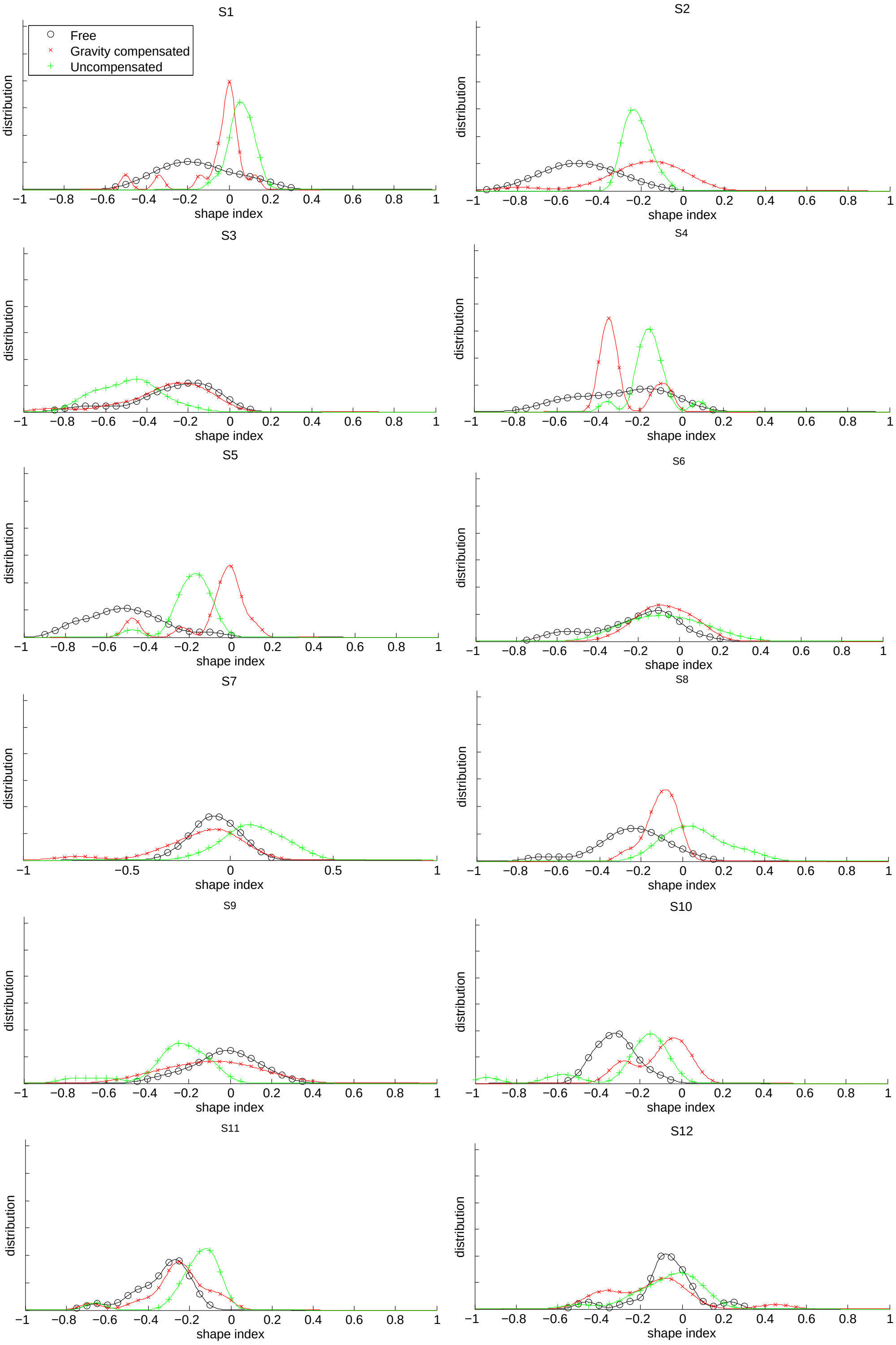

Figure 6.15: Distribution of shape index for each subject in different conditions.

6.5 Discussion

Introducing a wrist robot, in this chapter I studied the effect of mechanical constraints imposed by the robot to the subjects, i.e., gravity, friction and inertia, on motor coordination mechanisms in a redundant task.

Through different conditions I made a comparison between the free movements and movements while attached to the robot. I should mention that the conditions constituted a within subjects factor. Although the presentation order of the conditions was not randomized or counterbalanced, inspection of the data revealed no presence of learning effects. In particular, there were no differences between the first (free pointing) and third condition (gravity compensated), but significant differences between the first and second, and the second and third conditions for nine of the participants. If learning effects were present, the first and third conditions should not have been similar to one another.

In line with previous studies, e.g. [92], our results show that even though the robot is backdriveable, when the motors are off, the robot perturbs the natural coordination mechanisms. Implementing gravity and friction compensation, see Section 6.2.4, I tried to reduce the mechanical impendence and therefore the perturbation. After compensating for gravity and friction the PS joint of the robot would seem lighter to the subjects hence, the results showed a change in the movements for *gravity compensated* and *gravity-friction compensated* relative to the *uncompensated* movements, yet the movements are different than the *free* movements, see section 6.3.4.

To increase the degree of transparency of the robot, I modified the design, removed the load-cell since it was the main source of the inertia, in such a way that the perceived inertia of prono-supination DoF could be decreased to one third of its initial value. I repeated our experiments and found no significant difference between *free* and *gravity compensated* movements for most of the subjects, through a non-parametric analysis of variance (Kruskal-Wallis) test at 95% confidence level. This, demonstrates a high degree of transparency for our robot.

A comparison between the effect of our robot and the InMotion3 robot on the voluntary motions, compare Figure6.1 and Figure 6.14.b-c, in the proposed redundant task reveals that unlike the InMotion3, our robot is not perturbing the movements. Hence, our robot could be considered transparent also relative to the available commercial robots.

Finally, our results present a wrist robot which is transparent enough for studying human motor coordination mechanisms. Thus, this robot provides a reliable test-bed to study several important issues such as:

Impedance threshold. As I addressed in this report and could be seen in literature, excessive mechanical impedance could change the natural human strategies. Due to the lack of a transparent platform, it is not yet clear human sensory motor is more sensitive to what type of impedance. More importantly, no threshold for *perturbing* mechanical impedance is reported in literature, to the best of author's knowledge. This report and the resulted wrist robot could be used to perform such study.

Visuo-motor coordination. Our robot could be used as a 'transparent' platform to provide kinesthetic feedback required to be added to visual feedback to investigate visuo-motor coordination in presence of mis-orientation similar to the work reported by Masia et al. [57].

In summery, Table 6.3, illustrates a comparison between InMotion3 wrist robot from literature and the other two robots devised and studied in my study.

Table 6.3: Comparison between wrist robots studied in this research.

Robot	End-point inertia	Gravity comp.	Friction comp.	DoF Active	DoF Passive	Transparent
InMotion3	$12.0 \times 10^{-3}\, kg.m^2$	×	×	3	0	×
NTU-wrist1	$3.4 \times 10^{-3}\, kg.m^2$	✓	✓	1	4	×
NTU-wrist2	$1.0 \times 10^{-3}\, kg.m^2$	✓	×	1	3	✓

Chapter 7

Conclusion and Future Work

7.1 Conclusion

In this work, I analyze the effects of ergonomic factors and mechanical impedance on human motor strategies during redundant tasks, with focus on pointing tasks performed with the wrist. My work considered recent literature on the kinematic analysis of motor synergies in the redundant wrist ([11; 12; 13; 92; 93]) as a starting point. My contribution to [14] gave me the opportunity to familiarize myself with algorithms for quantitative assessment of motor synergies. Afterwards, I reapplied these assessment tools to analyse and quantify the influence of mechanical impedance on the soft constraints aiming to devising a transparent wrist platform, which is the main contribution of my PhD work.

Motor strategies (Donders' law) quantified in my thesis, in terms of quadratic surfaces, are shown to be subject-specific and sensitive to 'discomfort'. Discomfort arises due to misalignment, reaction forces between human limb and robot and so forth. As the first step, due to inter-subject anatomical differences, I determined subject-specific kinematic models by estimating anatomical parameters from wearable motion tracking sensors through a non-invasive protocol, adapted from literature. Known to be repeatable, I further investigated accuracy of the adapted method in parameter estimations as this would affect the alignment of the robot joints with the human's. Then I used the method to fit measurements performed on a human subject. The resulting parameters were applied in the design of a subject-specific, ergonomic exoskeleton, *ErgoExo*.

I evaluated how kinematic misalignment between robot and human joints would cause interaction forces, and therefore discomfort first through a numerical study. Afterwards, using the ErgoExo, I assessed the effect of misalignment on the natural coordination mechanisms in the redundant wrist. The study showed statistical significant differences for movements performed by a misaligned handle, i.e. uncomfortable, and either of the movements performed freely or by means of the ErgoExo.

Afterwards, I investigated the effects of kinematic compatibility. This study revealed that considering extra 'passive' degrees-of-freedom helps to prevent hyperstaticity, i.e. over-constrained configuration. In fact, the interaction forces could be decreased by 45%, suggesting that the releasing of extra passive degrees-of-freedom should be taken into account in the early phase of design. It could also be applied to modify the fixation points of commercial robots in order to reduce the magnitude of reaction forces.

I also studied the dynamic aspects of human-robot interaction and its effect on motor strategies. In line with previous studies, e.g. [92], these results confirmed that even backdrivable robots can perturb natural coordination mechanisms. Highlighting the role of inertia, especially on the PS joint, I devised my PS joint activated wrist robot. The inertia of my robot about the PS joint is $3.4 \times 10^{-3}\, kg.m^2$ which is one fourth of MIT-MANUS wrist module, InMotion3, and almost twice the inertia of the human forearm/hand. The results of the experiments, presented in Section 6.4.2, confirmed the transparency of the robot for most of the subjects.

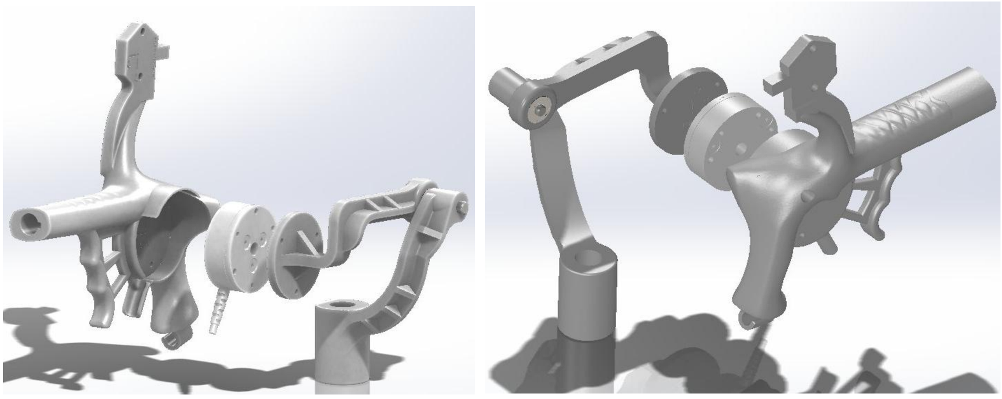

Figure 7.1: Locating the load cell (`Mini40-E` Transducer from ATI Industrial Automation, Inc.) into the handle.

7.2 Future work

Force recording through ErgoExo

The initial results for the first robot (Section 6.3.4) showed the load-cell inertia perturbed the motor strategies in most of the subjects, not just for its weight but mainly for its position (away from the PS axis). Figure 7.1, depicts a possible solution meant to include the load-cell into the handle, bringing the extra weight closer to the PS axis.

Conceptual design of a 2 active DoF exoskeleton

As a further step, beside the prono-supination DoF, the flexion-extension joint would be actuated. Through some modifications the *ErgoExo*, see Section 4.3, also could be mounted on this platform, hence, kinematically the robot would have 3 DoFs (PS and FE as two active DoFs and Radial-Ulnar deviation as a passive DoF). For this mechanism, the motors are grounded, as depicted in the

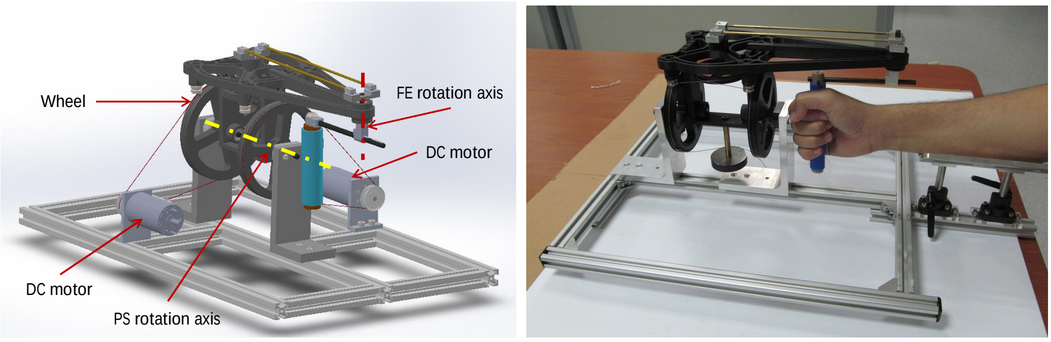

Figure 7.2: Differential mechanism to drive flexion-extension and prono-supination.

Figure 7.2.a, and through the cable driven differential mechanism the both of the PS and FE DoFs would be actuated. This mechanism follows the same principals explained through this report aiming a transparent robot. The preliminary prototype of the robot is illustrated in Figure 7.2.b.

In this differential mechanism, a simultaneous, either, clockwise or counterclockwise rotation of the wheels generates a rotation about prono-supination axis. Moreover, the clockwise rotation of one wheel during the counterclockwise rotation of the other wheel ends up with a rotation about flexion-extension axis. Main advantages of this deferential mechanism are:

- Motors are designed to be grounded, eventually would not be mobile during the operation, lowering the perceived inertia considerably and increasing compactness. This would overcome one of the drawbacks of the available commercialized robots. For example, in the robots depicted in Figure 2.1 (a) and (b), the motors' inertia would perceived in prono–supination activation.
- The use of the cables would results in zero backlash, fewer machined parts, easier assembly, and a more robust mechanism because the wheels slip under

excess torque rather than breaking gear teeth as would happen in a gear differential.

References

[1] S. K. Agrawal, S. K. Banala, A. Fattah, V. Sangwan, V. Krishnamoorthy, J. P. Scholz, and Hsu Wei-Li. Assessment of motion of a swing leg and gait rehabilitation with a gravity balancing exoskeleton. *IEEE Transactions on Neural Systems and Rehabilitation Engineering*, **15**[3]:410–420, 2007.

[2] J. G. Andrews and Y. Youm. A biomechanical investigation of wrist kinematics. *Journal of Biomechanics*, **12**[1]:83–93, 1979.

[3] E. Apergis. Wrist anatomy. In *Fracture-Dislocations of the Wrist*, pages 7–41. Springer Milan, January 2013.

[4] M. Bergamasco, B. Allotta, L. Bosio, L. Ferretti, G. Parrini, GM Prisco, F. Salsedo, and G. Sartini. An arm exoskeleton system for teleoperation and virtual environments applications. In *Robotics and Automation, Proceedings, IEEE International Conference on*, pages 1449–1454. IEEE, 1994.

[5] E. V. Biryukova, A. Roby-Brami, A. A. Frolov, and M. Mokhtari. Kinematics of human arm reconstructed from spatial tracking system recordings. *Journal of Biomechanics*, **33**[8]:985–995, 2000.

[6] R. Bogue. Exoskeletons and robotic prosthetics: a review of recent developments. *Industrial Robot: An International Journal*, **36**[5]:421–427, August 2009.

[7] G. A. Boy. *The Handbook of Human-machine Interaction: A Human-centered Design Approach.* Ashgate Publishing, Ltd., 2011.

[8] M. Brown, N. Tsagarakis, and D. G. Caldwell. Exoskeletons for human force augmentation. *Industrial Robot: An International Journal*, **30**:592–602, 2003.

[9] J. H. Burridge, R. Turk, S. V. Notley, R. M. Pickering, and D. M. Simpson. The relationship between upper limb activity and impairment in post-stroke hemiplegia. *Disability and rehabilitation*, **31**[2]:109–17, January 2009.

[10] D. G. Caldwell, O. Kocak, and U. Andersen. Multi-armed dexterous manipulator operation using glove/exoskeleton control and sensory feedback. In *Intelligent Robots and Systems. 'Human Robot Interaction and Cooperative Robots', Proceedings. IEEE/RSJ International Conference on*, pages 567 –572, vol.2, Pittsburgh, USA, Aug 1995.

[11] D. Campolo, D. Accoto, D. Formica, and E. Guglielmelli. Intrinsic constraints of neural origin: Assessment and application to rehabilitation robotics. *Robotics, IEEE Transactions on*, **25**[3]:492 –501, june 2009.

[12] D. Campolo, D. Accoto, F. Taffoni, and E. Guglielmelli. On the kinematics of human wrist during pointing tasks with application to

motor rehabilitation. *2008 IEEE International Conference on Robotics and Automation*, pages 1318–1323, Pasadena, USA, May 2008.

[13] D. Campolo, D. Formica, E. Guglielmelli, and F. Keller. Kinematic analysis of the human wrist during pointing tasks. *Experimental Brain Research*, **201**:561–573, 2010. 10.1007/s00221-009-2073-1.

[14] D. Campolo, F. Widjaja, M. Esmaeili, and E. Burdet. Pointing with the wrist: a postural model for donders law. *Experimental Brain Research*, **212**[3]:417–427, June 2011.

[15] M. Ceylan, D. Y. P. Henriques, D. B. Tweed, and J. D. Crawford. Task-dependent constraints in motor control: pinhole goggles make the head move like an eye. *The Journal of neuroscience : the official journal of the Society for Neuroscience*, **20**[7]:2719–30, April 2000.

[16] P.I. Corke. A robotics toolbox for MATLAB. *Robotics & Automation Magazine, IEEE*, **3**[1]:24–32, 1996.

[17] J. J. Crisco, S. W. Wolfe, C. P. Neu, and S. Pike. Advances in the in vivo measurement of carpal kinematics. *Orthopedic Clinics of North America*, **32**[2]:219–231, Apr 2001.

[18] A.G. Cutti, A. Giovanardi, L. Rocchi, A. Davalli, and R. Sacchetti. Ambulatory measurement of shoulder and elbow kinematics through inertial and magnetic sensors. *Medical and Biological Engineering and Computing*, **46**[2]:169–178, 2008.

[19] J. Denavit and R.S. Hartenberg. A kinematic notation for lower-pair mechanisms based on matrices. *Trans ASME J. Appl. Mech*, **23**:215–221, 1955.

[20] M. P. Do Carmo. *Differential Geometry of Curves and Surfaces*. Prentice Hall, New Jersey, 1976.

[21] G. Domien, L. Ilse, K. Lore, A. Geert, K. Els, and F. Peter. The armeo spring as training tool to improve upper limb functionality in multiple sclerosis: a pilot study. *Journal of NeuroEngineering and Rehabilitation*, **8**, 2007.

[22] F. C. Donders. Beitrag zur lehre von den bewegungen des menschlichen auges. *Holland Beitr Anat Physiol Wiss*, **1**[104]:384, 1848.

[23] M. Esmaeili, W. Dailey, E. Burdet, and D. Campolo. Ergonomic Design of a Wrist Exoskeleton and its Effects on Natural Motor Strategies During Redundant Tasks. *Robotics and Automation, ICRA. IEEE International Conference on*, Karlsruhe, Germany, May 2013.

[24] M. Esmaeili, K. Gamage, E. Tan, and D. Campolo. Ergonomic considerations for anthropomorphic wrist exoskeletons: A simulation study on the effects of joint misalignment. In *Intelligent Robots and Systems (IROS), IEEE/RSJ International Conference on*, pages 4905 –4910, San Francisco, USA, Sept. 2011.

[25] M. Esmaeili, N. Jarrassé, W. Dailey, E. Burdet, and D. Campolo. Hyperstaticity for Ergonomic Design of a Wrist Exoskeleton. *Re-*

habilitation Robotics, ICORR. IEEE International Conference on, Seattle, USA, June 2013.

[26] M. Esmaeili, S. Moussouni, F.n Widjaja, K. Gamage, and D. Campolo. Accuracy and repeatability of parameter estimation methods from ambulatory data for the wrist joint. In *33rd Annual International Conference of the IEEE Engineering in Medicine and Biology Society (EMBC), International Conference on*, Boston, USA, Aug 30th – Sept 3rd 2011.

[27] M. Fetter. *Three-dimensional kinematics of eye, head and limb movements.* CRC, 1997.

[28] M. Fontana, A. Dettori, F. Salsedo, and M. Bergamasco. Mechanical design of a novel hand exoskeleton for accurate force displaying. In *Robotics and Automation, 2009. ICRA '09. IEEE International Conference on*, pages 1704 –1709, Kobe, Japan, May 2009.

[29] L. Giugovaz and J.M. Hollerbach. Closed-loop kinematic calibration of the sarcos dextrous arm. In *Proceedings of the IEEE/RSJ/GI International Conference on Intelligent Robots and Systems '94. 'Advanced Robotic Systems and the Real World', IROS '94*, pages 329–334 vol.1, Munich, Germany, 1994.

[30] R.A.R.C. Gopura and K. Kiguchi. Development of a 6DOF exoskeleton robot for human Upper-Limb motion assist. In *Information and Automation for Sustainability, 2008. ICIAFS 2008. 4th International Conference on*, pages 13–18, Colombo, Sri Lanka, 2008.

[31] A. Goto, H. Moritomo, T. Murase, K. Oka, K. Sugamoto, T. Arimura, J. Masumoto, S. Tamura, H. Yoshikawa, and T. Ochi. In vivo three-dimensional wrist motion analysis using magnetic resonance imaging and volume-based registration. *Journal of Orthopaedic Research: official publication of the Orthopaedic Research Society*, **23**[4]:750–6, July 2005.

[32] A. Gupta, M. K. O'Malley, V. Patoglu, and C. Burgar. Design, control and performance of RiceWrist: a force feedback wrist exoskeleton for rehabilitation and training. *The International Journal of Robotics Research*, **27**[2]:233 –251, February 2008.

[33] K. Hashtrudi-Zaad and S. E. Salcudean. Transparency in time-delayed systems and the effect of local force feedback for transparent teleoperation. *Robotics and Automation, IEEE Transactions on*, **18**[1]:108–114, 2002.

[34] M. Hillman. 2 Rehabilitation Robotics from Past to Present A Historical Perspective. In Z.Zenn Bien and Dimitar Stefanov, editors, *Advances in Rehabilitation Robotics*, chapter 2, pages 25–44. Springer Berlin Heidelberg, 2004.

[35] N. Hogan and H.I. Krebs. Interactive robots for neuro-rehabilitation. *Restorative neurology and neuroscience*, **22**[3-5]:349–358, 2004.

[36] C.H. Hsu. Developing accurate industrial standards to facilitate production in apparel manufacturing based on anthropometric data. *Human Factors and Ergonomics in Manufacturing*, **19**[3]:199–211, 2009.

[37] J.F. Jansen. *Exoskeleton for soldier enhancement systems feasibility study. Report ORNL/TM-2000/256).* Oak Ridge National Laboratory Oak Ridge, TN, 2000.

[38] N. Jarrasse and G. Morel. On the kinematic design of exoskeletons and their fixations with a human member. In *Proceedings of Robotics: Science and Systems*, Zaragoza, Spain, June 2010.

[39] N. Jarrasse and G. Morel. Connecting a Human Limb to an Exoskeleton. *IEEE Transactions on Robotics*, **28**[3]:697 –709, June 2012.

[40] N. Jarrassé, M. Tagliabue, J.V.G. Robertson, A. Maiza, V. Crocher, A. Roby-Brami, and G. Morel. A methodology to quantify alterations in human upper limb movement during co-manipulation with an exoskeleton. *Neural Systems and Rehabilitation Engineering, IEEE Transactions on*, **18**[4]:389–397, 2010.

[41] H. Kazerooni. Human-robot interaction via the transfer of power and information signals. *Systems, Man and Cybernetics, IEEE Transactions on*, **20**[2]:450 –463, mar/apr 1990.

[42] H. Kazerooni. The human power amplifier technology at the university of california, berkeley. *Robotics and Autonomous Systems*, **19**[2]:179 – 187, 1996.

[43] H. Kazerooni. Exoskeletons for human power augmentation. In *Intelligent Robots and Systems, 2005. (IROS 2005). 2005 IEEE/RSJ International Conference on*, pages 3459 – 3464, Edmonton, Canada, Aug. 2005.

[44] Y. Kijima and S. F. Viegas. Wrist anatomy and biomechanics. *The Journal of Hand Surgery*, **34**[8]:1555–1563, October 2009.

[45] J. J. Koenderink and A. J. van Doorn. Surface shape and curvature scales. *Image and Vision Computing*, **10**[8]:557–564, October 1992.

[46] H.I. Krebs, J.J. Palazzolo, L. Dipietro, M. Ferraro, J. Krol, K. Rannekleiv, B.T. Volpe, and N. Hogan. Rehabilitation robotics: Performance-based progressive robot-assisted therapy. *Autonomous Robots*, **15**:7–20, 2003. 10.1023/A:1024494031121.

[47] H.I. Krebs, B.T. Volpe, D. Williams, J. Celestino, S.K. Charles, D. Lynch, and N. Hogan. Robot-aided neurorehabilitation: A robot for wrist rehabilitation. *Neural Systems and Rehabilitation Engineering, IEEE Transactions on*, **15**[3]:327 –335, Sept. 2007.

[48] D. A. Lawrence. Impedance control stability properties in common implementations. In *Robotics and Automation, Proceedings., IEEE International Conference on*, pages 1185 –1190 vol.2, Philadelphia, USA, Apr 1988.

[49] D. A. Lawrence. Stability and transparency in bilateral teleoperation. *Robotics and Automation, IEEE Transactions on*, **9**[5]:624–637, 1993.

[50] H. Lee, B. Lee, W. Kim, M. Gil, J. Han, and C. Han. Human-robot cooperative control based on pHRI (Physical Human-Robot Interaction) of exoskeleton robot for a human upper extremity. *International Journal of Precision Engineering and Manufacturing*, **13**[6]:985–992, June 2012.

[51] J. D. Lee, A. Kirlik, and M. J. Dainoff. *The Oxford Handbook of Cognitive Engineering*. Oxford University Press, March 2013.

[52] J. Lenarcic and M. L. Husty. *Latest Advances in Robot Kinematics*. Springer, May 2012.

[53] L. Leonard, D. Sirkett, G. Mullineux, G. Giddins, and A. W. Miles. Development of an in-vivo method of wrist joint motion analysis. *Clinical Biomechanics*, **20**[2]:166–171, 2005.

[54] D. G. Liebermann, A. Biess, J. Friedman, C. C. A. M. Gielen, and T. Flash. Intrinsic joint kinematic planning. i: Reassessing the listings law constraint in the control of three-dimensional arm movements. *Experimental Brain Research*, **171**[2]:139–154, 2006.

[55] H. S. Lo and S. Q. Xie. Exoskeleton robots for upper-limb rehabilitation: State of the art and future prospects. *Medical Engineering & Physics*, **34**[3]:261–268, April 2012.

[56] L.I. Lugo-Villeda, A. Frisoli, O. Sandoval-Gonzalez, M.A. Padilla, V. Parra-Vega, C.A. Avizzano, E. Ruffaldi, and M. Bergamasco. Haptic guidance of Light-Exoskeleton for arm-rehabilitation tasks. In *Robot and Human Interactive Communication, RO-MAN 2009. The 18th IEEE International Symposium on*, pages 903 –908, Toyama, Japan, Oct 2009.

[57] L. Masia, M. Casadio, G. Sandini, and P. Morasso. Eye-hand coordination during dynamic visuomotor rotations. *PLoS ONE*, **4**[9]:e7004, 2009.

[58] L. Masia, N.N. Rodriguez, M. Casadio, P. Morasso, G. Sandini, and P. Giannoni. Adaptive training strategy of distal movements by means of a wrist-robot. In *Advances in Computer-Human Interactions, 2009. ACHI '09. Second International Conferences on*, pages 227 –233, feb. 2009.

[59] L. Masia, V. Squeri, E. Burdet, G. Sandini, and P. Morasso. Wrist Coordination in a Kinematically Redundant Stabilization Task. *Haptics, IEEE Transactions on*, **5**[3]:231 –239, 2012.

[60] D. Mayhew, B. Bachrach, W. Z Rymer, and R. F Beer. Development of the MACARM - a novel cable robot for upper limb neurorehabilitation. In *Rehabilitation Robotics, 9th International Conference on*, pages 299– 302, July 2005.

[61] S. Mehta, P. E. K. Berg-Yuen, E. L. Pasiliao, and R. A. Murphey. A control architecture for human-machine interaction in the presence of unreliable automation and operator cognitive limitations. In *AIAA Guidance, Navigation, and Control Conference*. American Institute of Aeronautics and Astronautics.

[62] N. Mizen. Powered exoskeletal apparatus for amplifying human strength in response to normal body movements, June 17 1969. US Patent 3,449,769.

[63] R. S. Mosher. Handyman to hardiman: Soc. *Automotive Eng*, 1967.

[64] R.M. Murray, Z. Li, , and S.S. Sastry. *A mathematical introduction to robotic manipulation*. CRC, 1994.

[65] J. Oblak, I. Cikajlo, and Z. Matjacic. Universal Haptic Drive: A Robot for Arm and Wrist Rehabilitation. *Neural Systems and Rehabilitation Engineering, IEEE Transactions on*, **18**[3]:293 –302, June 2010.

[66] J.F. OBrien, R.E. Bodenheimer Jr, G.J. Brostow, and J.K. Hodgins. Automatic joint parameter estimation from magnetic motion capture data. *Proceedings of Graphics Interface*, pages 53–60, 2000.

[67] J.L. Pons. *Wearable robots: biomechatronic exoskeletons*. Wiley Online Library, 2008.

[68] R. A. Prokopenko, A. A. Frolov, E. V. Biryukova, and A. Roby-Brami. Assessment of the accuracy of a human arm model with seven degrees of freedom. *Journal of Biomechanics*, **34**[2]:177–185, 2001.

[69] D.J. Reinkensmeyer, N. Hogan, H.I. Krebs, S.L. Lehman, and P.S. Lum. Rehabilitators, robots, and guides: New tools for neurological rehabilitation. *Biomechanics and neural control of posture and movement*, pages 516–533, 2000.

[70] Y. Ren, S. Kang, H. Park, Y. Wu, and L. Zhang. Developing a Multi-Joint Upper Limb Exoskeleton Robot for Diagnosis, Therapy and Outcome Evaluation in Neurorehabilitation. *IEEE Transactions on Neural Systems and Rehabilitation Engineering*, **PP**[99]:1, 2012.

[71] D.W. Repperger, B.O. Hill, C. Hasser, M. Roark, and C.A. Phillips. Human tracking studies involving an actively powered, augmented exoskeleton. In *Biomedical Engineering Conference, 1996., Pro-*

ceedings of the 1996 Fifteenth Southern, pages 28–31, Dayton, USA, Mar 1996.

[72] N. Rezzoug, J. Jacquier-Bret, and P. Gorce. A method for estimating three-dimensional human arm movement with two electromagnetic sensors. *Computer Methods in Biomechanics and Biomedical Engineering*, **13**[6]:663–668, 2010.

[73] E. Rocon, A.F. Ruiz, J.L. Pons, J.M. Belda-Lois, and J.J. Sanchez-Lacuesta. Rehabilitation robotics: a wearable Exo-Skeleton for tremor assessment and suppression. In *IEEE/ICRA*, pages 2271–2276, Barcelona, Spain, 2005.

[74] G. Rosati, P. Gallina, and S. Masiero. Design, Implementation and Clinical Tests of a Wire-Based Robot for Neurorehabilitation. *IEEE Transactions on Neural Systems and Rehabilitation Engineering*, **15**[4]:560–569, December 2007.

[75] A.F. Ruiz, A. Forner-Cordero, E. Rocon, and J.L. Pons. Exoskeletons for rehabilitation and motor control. In *Biomedical Robotics and Biomechatronics, BioRob. The First IEEE/RAS-EMBS International Conference on*, pages 601–606, Pisa, Italy, 2006.

[76] R. L. Sainburg, J. E. Lateiner, M. L. Latash, and L. B. Bagesteiro. Effects of altering initial position on movement direction and extent. *Journal of neurophysiology*, **89**[1]:401–15, January 2003.

[77] G. Salvendy. *Handbook of Human Factors and Ergonomics.* John Wiley & Sons, March 2012.

[78] R. A. Scheidt, D. J. Reinkensmeyer, M. A. Conditt, W. Z. Rymer, and F. A. Mussa-Ivaldi. Persistence of motor adaptation during constrained, multi-joint, arm movements. *Journal of Neurophysiology*, **84**[2]:853–862, August 2000.

[79] A. Schiele. *Fundamentals of ergonomic exoskeleton robots.* PhD thesis, 2008.

[80] A. Schiele. Ergonomics of exoskeletons: Objective performance metrics. In *EuroHaptics conference, 2009 and Symposium on Haptic Interfaces for Virtual Environment and Teleoperator Systems. World Haptics 2009. Third Joint*, pages 103–108. IEEE, 2009.

[81] A. Schiele. An explicit model to predict and interpret constraint force creation in pHRI with exoskeletons. IEEE/ICRA, pp. 1324–1330, Pasadena, USA, 2008.

[82] A. Schiele, M. De Bartolomei, and F. van der Helm. Towards intuitive control of space robots: A ground development facility with exoskeleton. In *Intelligent Robots and Systems, 2006 IEEE/RSJ International Conference on*, pages 1396 –1401, Beijing, China, Oct. 2006.

[83] A. Schiele and F.C.T. van der Helm. Kinematic design to improve ergonomics in human machine interaction. *IEEE Transactions on Neural Sys and Rehab Eng*, **14**[4]:456–469, 2006.

[84] R.J. Schilling. *Fundamentals of robotics: analysis and control.* Simon & Schuster Trade, 1996.

[85] F. Sergi, D. Accoto, D. Campolo, and E. Guglielmelli. Forearm orientation guidance with a vibrotactile feedback bracelet: On the directionality of tactile motor communication. In *Biomedical Robotics and Biomechatronics, 2nd IEEE RAS & EMBS International Conference on*, pages 433–438, Scottsdale, USA, 2008.

[86] F. Sergi, D. Accoto, N.L. Tagliamonte, G. Carpino, and E. Guglielmelli. A systematic graph-based method for the kinematic synthesis of non-anthropomorphic wearable robots for the lower limbs. *Frontiers of Mechanical Engineering in China*, 2010.

[87] K. Shoemake. Animating rotation with quaternion curves. In *Proceedings of the 12th annual conference on Computer graphics and interactive techniques*, SIGGRAPH '85, pages 245–254, New York, NY, USA, 1985. ACM.

[88] B. Siciliano and O. Khatib. *Springer Handbook of Robotics*. Springer, June 2008.

[89] Z. Song and S. Guo. Implementation of self-rehabilitation for upper limb based on a haptic device and an exoskeleton device. In *Mechatronics and Automation (ICMA), International Conference on*, pages 1911 –1916, Beijing, China, Aug 2011.

[90] S.J. Spencer, J. Klein, K. Minakata, V. Le, J.E. Bobrow, and D.J. Reinkensmeyer. A low cost parallel robot and trajectory optimization method for wrist and forearm rehabilitation using the wii. In *Biomed-*

ical Robotics and Biomechatronics, BioRob 2008. 2nd IEEE RAS EMBS International Conference on, pages 869 –874, Scottsdale, USA, Oct. 2008.

[91] V. Squeri, L. Masia, P. Giannoni, G. Sandini, and P. Morasso. Wrist Rehabilitation in Chronic Stroke Patients by Means of Adaptive, Progressive Robot Aided Therapy. *IEEE transactions on neural systems and rehabilitation engineering : a publication of the IEEE Engineering in Medicine and Biology Society*, [c], March 2013.

[92] N. L. Tagliamonte, M. Scorcia, D. Campolo, and E. Guglielmelli. Effects of Impedance Reduction of a Robot for Wrist Rehabilitation on Human Motor Strategies in Healthy Subjects during Pointing Tasks. *Advanced Robotics*, **25**[May 2013]:537–562, 2011.

[93] N.L. Tagliamonte, D. Formica, D. Campolo, and E. Guglielmelli. Coping with intrinsic constraints of neural origin in the design of rehabilitation robots: A preliminary study. In *Neural Engineering, 2009. NER'09. 4th International IEEE/EMBS Conference on*, pages 124–127. IEEE, 2009.

[94] N.L. Tagliamonte, D. Formica, M. Scorcia, D. Campolo, and E. Guglielmelli. Force control of a robot for wrist rehabilitation: Towards coping with human intrinsic constraints. In *Intelligent Robots and Systems (IROS), 2010 IEEE/RSJ International Conference on*, pages 4384–4389, Taipei, Taiwan, 2010.

[95] N.L. Tagliamonte, M. Scorcia, D. Formica, F. Taffoni, D. Campolo, and E. Guglielmelli. Force control of a robot for wrist rehabil-

itation: Coping with human motor strategies during pointing tasks. *RSJ Advanced Robotics Journal*, **25**:537–562, 2011.

[96] N. Tsagarakis, D.G. Caldwell, and G. A. Medrano-Cerda. A 7 DOF pneumatic muscle actuator (pMA) powered exoskeleton. In *8th IEEE International Workshop on Robot and Human Interaction, RO-MAN '99*, pages 327–333, Pisa, Italy, 1999.

[97] D. Tweed and T. Vilis. Geometric relations of eye position and velocity vectors during saccades. *Vision Research*, **30**[1]:111–127, 1990.

[98] A. E. Q. van Delden, C. E. Peper, G. Kwakkel, and P. J. Beek. A Systematic Review of Bilateral Upper Limb Training Devices for Poststroke Rehabilitation. *Stroke Research and Treatment*, **2012**:1–17, 2012.

[99] H. E. J. Veeger, B. Yu, K. An, and R. H. Rozendal. Parameters for modeling the upper extremity. *Journal of Biomechanics*, **30**[6]:647–652, June 1997.

[100] R. Volpe and P. Khosla. A theoretical and experimental investigation of explicit force control strategies for manipulators. *IEEE Transactions on Automatic Control*, **38**[11]:1634–1650, 1993.

[101] D.W. Weir, J.E. Colgate, and M.A Peshkin. Measuring and increasing z-width with active electrical damping. In *symposium on Haptic interfaces for virtual environment and teleoperator systems*, pages 169–175, March 2008.

[102] G. Welch and E. Foxlin. Motion tracking: no silver bullet, but a respectable arsenal. *Computer Graphics and Applications, IEEE*, **22**[6]:24–38, 2002.

[103] V. Wigmore, C. Tong, and J. Randall. Visuomotor rotations of varying size and direction compete for a single internal model in a motor working memory. *Journal of Experimental Psychology: Human Perception and Performance*, **28**[2]:447–457, 2002.

[104] D.J. Williams, H.I. Krebs, and N. Hogan. A robot for wrist rehabilitation. In *IEEE/EMBS*, pages 1336–1339 vol.2, Istanbul, Turkey, 2001.

[105] I.I. Williams, M. Murphy, J. Berlin, and M. Krier. Kinesthetic force/moment feedback via active exoskeleton. In *Proceedings of the Image Society Conference, Scottsdale, AZ*, 1998.

[106] S. W. Wolfe, J. J. Crisco, and L. D. Katz. A non-invasive method for studying in vivo carpal kinematics. *Journal of hand surgery (Edinburgh, Scotland)*, **22**[2]:147–52, April 1997.

[107] G. Wu, F. van der Helm, H.E.J. Veeger, M. Makhsous, P. Van Roy, C. Anglin, J. Nagels, A.R. Karduna, K. McQuade, X. Wang, F.W. Werner, and B. Buchholz. ISB recommendation on definitions of joint coordinate systems of various joints for the reporting of human joint motion–Part II: shoulder, elbow, wrist and hand. *Journal of Biomechanics*, **38**[5]:981–992, May 2005.

[108] N. Yagn. Apparatus for facilitating walking, running and jumping, November 18 1890. US Patent 440,684.

[109] C. J. Yang, J. F. Zhang, Y. Chen, Y. M. Dong, and Y. Zhang. A review of exoskeleton-type systems and their key technologies. *Proceedings of the Institution of Mechanical Engineers, Part C: Journal of Mechanical Engineering Science*, **222**[8]:1599–1612, August 2008.

[110] L. Zollo, S. Roccella, E. Guglielmelli, M.C. Carrozza, and P. Dario. Biomechatronic design and control of an anthropomorphic artificial hand for prosthetic and robotic applications. *Mechatronics, IEEE/ASME Transactions on*, **12**[4]:418 –429, Aug. 2007.